THÈSE

En vue de l'obtention du

DOCTORAT DE L'UNIVERSITÉ DE TOULOUSE

Délivré par : *l'Université Toulouse 3 Paul Sabatier (UT3 Paul Sabatier)*

Présentée et soutenue le *05 février 2014* **par :**

ISIDRE MATEU SUAU

Systèmes de détection digitaux par traitement numérique des impulsions X-dur pour des applications spatiales

---

JURY

DOMINIQUE TOUBLANC	Professeur, UPS/IRAP	Président du Jury
LORENZO NATALUCCI	Chercheur, INAF	Examinateur
ALAIN BARDOUX	Ingénieur, CNES	Examinateur
PHILIPPE LAURENT	Ingénieur, CEA	Rapporteur
OLIVIER LIMOUSIN	Ingénieur, CEA	Rapporteur
JEAN-PIERRE ROQUES	Directeur de recherche, IRAP	Directeur de thèse

---

École doctorale et spécialité :
SDU2E : Astrophysique, Sciences de l'Espace, Planétologie
Unité de Recherche :
Institut de Recherche en Astrophyisique et Planétologie (UMR 5277)
Directeur de Thèse :
Jean-Pierre ROQUES
Rapporteurs :
Philippe LAURENT et *Olivier LIMOUSIN*

Acknowledgements

Firstly, I would like to thank Jean-Pierre for giving me the opportunity to do this thesis. Working with someone who lives so passionately science and instrumentation has been a great experience for me and a continuous source of learning. I want to thank him specially for the confidence shown to me at all times, giving me full freedom and autonomy in my research, while always staying close for any advice or guide that I could need. Both from a personal and professional point of view, working with him has been a real pleasure over the last three years.

I also want to thank the whole Phenix team. Odile, Elsa, David, Jacques, Nicole, thank you for the hard work and for the superb atmosphere within the team. Without you this manuscript would not have been possible.

My thanks also to other people who helped me during these three years. Thanks to Elisabeth Jourdain for her advice and for helping me in the writing of both the articles and this document. Thanks also to Patrice Medina for the *MGS* simulator. Finally, thanks to Gonzalo Campos for those fantastic Pspice simulations.

Many thanks to the jury of the thesis for taking the time to read and evaluate my work. I specially thank Dr P.Laurent and Dr O.Limousin for their valuable comments that allowed me to improve this manuscript.

In addition to enriching from a professional perspective, my stay at IRAP has been the opportunity to meet a handful of extraordinary people. I want to mention Romain, Anthony and Alexis, friends in this journey from the beginning. Many thanks to you for all the good times spent together!

Outside the lab, I would not want to miss the opportunity to thank the great friends I have made in Toulouse. To put it simply, these were the best years of my life, and that was thanks to you. I do not put names for fear of forgetting someone, but anyone who takes the trouble to read this can feel included.

Finally, many, many thanks to my family. Margalida, Joan, Maria, Miquel and Joanet. Thank you for your unconditional love and support that I feel at all times, no matter the kilometres between us.

Agraïments

En primer lloc, voldria agraïr en Jean-Pierre per haver-me donat l'oportunitat de fer aquesta tesi. Treballar amb algú que viu amb tanta passió la ciència i la instrumentació ha sigut per mi una gran experiència i una continua font d'aprenentatge. Vull agraïr en particular la confiança que en tot moment m'ha demostrat, donat-me plena llibertat i autonomia en la meva recerca, al mateix temps que es mantenia sempre pròxim per qualsevol consell o guia que pogués necessitar. Tant del punt de vist personal com professional, treballar amb ell ha sigut un veritable plaer durant aquests més de tres anys.

Vull també agraïr tot l'equip de Phenix. Odile, Elsa, David, Jacques, Nicole, moltes gràcies per la dura feina feta i per l'inmillorable acull al si de l'equip. Sense vosaltres aquest manuscrit no hauria estat possible.

Els meus agraïments també per altra gent que m'ha ajudat durant aquests tres anys. Gracies a Elisabeth Jourdain pels seus consells i per ajudar-me en l'escriptura tant dels articles com d'aquest document. Gracies també a Patrice Medina per facilitar-me la tasca amb el seu simulador MGS. Finalment, gràcies a Gonzalo per les fantàstiques simulacions Pspice.

Moltes gràcies al jurat de la tesi per haver pres el temps de llegir i evaluar la meva feina. En especial, gràcies al Dr. O. Limousin i al Dr. P. Laurent pels valiosos comentaris que m'han permès de millorar aquest manuscrit.

A més d'enriquidora en el pla professional, en aquesta etapa a l'IRAP he tingut la sort de conèixer un bon grapat de gent extraordinària. Penso especialment a en Romain, Anthony i Alexis, companys de viatge des del principi. Moltes gràcies per tots els bons moments que m'heu fet passar!

Fora del laboratori, no voldria deixar passar l'oportunitat de donar les gràcies a les grans amistats que he fet a Toulouse. Per dir-ho simplement, si aquests han sigut els millors anys de la meva vida és gràcies a vosaltres. No poso noms per por d'oblidar algú, però qualsevol que es prengui la molèstia de llegir això s'hi pot sentir inclòs.

Per acabar, moltes, moltíssimes gràcies a la meva família. Margalida, Joan, Maria, Miquel i Joanet. Gràcies pel vostre amor i suport incondicional que sento en tot moment, malgrat els quilòmetres de distància.

Contents

List of Figures

List of Tables

Introduction

Thanks to the extension of the focusing capabilities to the hard X-ray domain and the use of extensible mast technology, focusing telescopes with focal lengths of several tens of meters providing wide X-ray coverage might be not too far away. At the time of writing, the NuSTAR[1] telescope is operative and already capable of focusing X-rays up to 80keV using a 10 meter mast. Similar coverage will be provided by Astro-H[2], to be launched in 2015. New depth graded multilayer coatings, allowing the focusing of rays up to several hundreds of keV have been proposed recently [3] for designs using mast lengths between 20 and 50 meters. As an alternative for deployable masts, formation flying was studied for Symbol-X[4] to achieve a long focal, although the project was finally cancelled. The use of focusing optics will represent a gain in sensitivity up to two or three orders of magnitude with respect to the currently operational observatories, and thus, a huge increase of the number of potential sources to be observed in the sky. High angular resolution will therefore be needed in order to correctly discriminate the new emitters. In parallel, a detector offering a spatial resolution on a par with the angular resolution, while, at the same time, maintaining high energy resolution, must be developed.

In this context, PheniX, a detection system based on a high-purity Germanium (HPGe) double sided strip detector (DSSD), aiming at a broad X-ray coverage including the entire hard X-ray band, is presented in this work. The project was initially proposed by IRAP to CNES, constituting later a proposal [5] of a whole instrument concept in answer to ESA's Announcement of Opportunity for its Medium-Class Science Mission, M3, in 2010. Although not selected, research work continued in the form of a Research and Technology action at IRAP, funded by CNES, for the development and study of a detector prototype. The use of Germanium ensures high energy resolution, while a DSSD allows to obtain a highly pixelated image with a reduced number of channels. The segmentation of each electrode in N strips with orthogonal orientation between the anode and the cathode yields N^2 pixels with only $2N$ electronic readout channels. In addition, the depth of the interaction can be determined based on timing measurements. This completes a three dimensional location of the photons interaction points, which can be used for background reduction purposes or polarimetry measurements.

This thesis focuses on the acquisition and processing of the impulsions from the detector, in order

to retrieve the useful information for spectroscopy and imaging purposes. We propose a system based on an early digitization of the signal waveform after the charge-sensitive amplifier, for which we have developed algorithms in the digital domain with the objectives of, first, measuring the energy on each channel, and second, estimating the position of the interaction inside the detector volume. In addition to the implementation of the algorithms, we completed the study with performance analysis using a software tool for the simulation of the charge collection process inside the detector, and laboratory tests of the Phenix prototype. All this has allowed us to validate the working principles of the detector and thus, demonstrate the feasibility of a detection system featuring good spectroscopic properties and an accurate determination of the interaction point in the three dimensions.

The first chapter presents the context of X-ray astronomy, with an inventory of the observatories currently in space and a focus on the different types of detectors used in X-ray astronomy. The telescope concept which would accommodate the Phenix detection system is described at the end of the chapter.

Chapter 2 begins by describing the working principles of a DSSD, emphasizing the phenomena of charge splitting among segments and the apparition of transient signals on the strips without net charge collection. The possibility to exploit these effects to improve the spatial resolution of the device, using algorithms capable of analysing multiple strips at a time, is discussed. Following, the processes of signal readout and acquisition in the Phenix experimental setup are presented. The analogue electronics in use are described, as well as the trigger mechanism and digitization.

The next chapter covers the software tools that have been used for the simulation of the system. MGS, a Matlab-based code developed at IPHC laboratory, was adapted to the DSSD case and used for the simulation of the charge collection process and the signal response of the detector. A validation of the simulator was also made, including the comparison of the electric potential calculated by the program to what is obtained using a theoretical approach, as well as the comparison of the calculated pulses to the measurements obtained with the prototype. A brief description of the analogue electronics model, implemented using Pspice, is also provided.

The 4^{th} chapter addresses the signal processing chain that was implemented for the calculation of the energy measured by each strip, based on a trapezoidal shaping of the pulses. Charge sharing and its effect on the measurement of the full energy deposited in the interaction is discussed next, and illustrated with observations on real data measured on the prototype. A method for the calibration of a DSSD in presence of charge splitting is also presented. At the end of the chapter the energy resolutions measured at the energies of the calibration sources.

The last chapter treats the determination of the interaction point in three dimensions. An algorithm for the estimation of the number of interactions in an event and their respective positions is presented. The method is based on a joint analysis of the signal measured on multiple electronic channels, by

comparison with a pre-stored set of responses to a grid of basis points. The algorithm is used first in a simulation to investigate the possibility to use the transient signals induced to the strips neighbouring those collecting the main part of the charge. Finally, the results of its application to prototype measurements are reported. First, the measured distributions for the penetration depth, using the algorithm, are compared to the theoretical absorption of the sources used to irradiate the detector; and second, the images obtained when shadowing parts of the detector with different masks are presented. In this way, the principles of 3D localization of the interaction point are validated.

Introduction

Grâce à la capacité de focaliser les photons jusque dans le domaine des rayons X-dur et à l'utilisation de mâts extensibles, le lancement de télescopes ayant des distances focales de quelques dizaines de mètres pourrait être bientôt possible. Au moment où nous écrivons, le télescope NuSTAR[1], capable de focaliser des rayons X jusqu'à 80 keV en utilisant un mât de 10 mètres est déjà opérationnel. Une couverture similaire sera offerte par Astro-H[2], qui sera lancé en 2015. De nouveaux revêtements multicouches à épaisseur variable ont été proposés récemment pour être utilisés avec des mâts de 20-50 mètres. Comme alternative aux mâts extensibles, l'utilisation de la technique de vol en formation a été étudiée pour Symbol-X[4], pour obtenir une grande distance focale, mais le projet a été finalement arrêté. L'utilisation d'optiques focalisantes en X-durs représentera un gain en sensibilité jusqu'à deux ou trois ordres de grandeur par rapport aux observatoires actuellement en opération, et par conséquent, une augmentation considérable du nombre potentiel de sources observables dans le ciel. Une haute résolution angulaire sera donc nécessaire pour discriminer ces nouveaux émetteurs. En parallèle, le développement d'un détecteur offrant une résolution spatiale au niveau de cette résolution angulaire, tout en proposant une excellente résolution en énergie, sera indispensable.

Dans ce contexte, nous présentons PheniX, un système de détection basé sur un détecteur en Germanium d'haute pureté (HPGe: *High purity Germanium*) de type DSSD *(*double sided strip detector). C'est à dire, une géométrie planaire et des électrodes segmentées en pistes. Le projet a été initialement présenté par l'IRAP au CNES puis a fait l'objet d'une proposition[5] d'instrument complet en réponse à l'*Announcement of Oportunity* pour une mission de taille moyenne M3 de l'ESA, en 2010. Bien que non retenu, ce projet de recherche a continué à l'IRAP sous la forme d'une action de Recherche et Développement, financée par le CNES, pour le développement et l'étude d'un prototype de détecteur. L'utilisation du Germanium assure une haute résolution en énergie, alors que la technologie DSSD permet d'obtenir des images avec un grand nombre de pixels et un nombre réduit de chaines de traitement. La segmentation de chaque électrode en N pistes avec une orientation orthogonale entre l'anode et la cathode produit N^2 pixels avec seulement 2N canaux. De plus, la profondeur d'interaction des photons peut etre déterminée par la mesure des temps d'arrivée des pulses. Ceci apporte une localisation en 3D

du point d'interaction, qui peut être utilisée pour réduire le bruit de fond vu par le détecteur ou pour realiser des mesures de polarisation.

Cette thèse se centre sur l'acquisition et le traitement des impulsions en sortie du détecteur, pour extraire l'information utile aux fonctions de spectroscopie et d'imagerie. Nous proposons un système basé sur une numérisation rapide du signal après l'amplificateur de charge. Pour cela, nous avons développé des algorithmes numériques avec pour but de mesurer l'énergie sur chaque canal et d'estimer la position de l'interaction dans le volume du détecteur. En plus de l'implémentation des algorithmes, nous avons complété notre étude avec des analyses de performance, en nous servant d'un code de simulation pour le processus de collection de charge dans le détecteur, et avec des tests en laboratoire sur le prototype PheniX. Tout cela nous a permis de valider les principes de fonctionnement du détecteur et, ainsi, de démontrer la faisabilité d'un système de détection dans une large bande d'énergie couvrant le domaine des X-dur, avec à la fois de bonnes propriétés spectroscopiques et une détermination précise du point d'interaction.

Le premier chapitre présente le contexte de l'astronomie X, avec un inventaire des observatoires actuellement dans l'espace, et des différents types de détecteur utilisés en l'astronomie X. Le concept d'un télescope qui pourrait intégrer le système de détection Phenix est décrit à la fin du chapitre.

Le chapitre 2 décrit tout d'abord les principes de fonctionnement d'un DSSD, avec la présentation des phénomènes de répartition de charge entre segments et l'apparition de signaux transitoires sur les pistes sans collection nette de charge. La possibilité d'exploiter ces effets pour améliorer la résolution spatiales du dispositif, tout en utilisant des algorithmes capables d'analyser plusieurs canaux simultanément, est évaluée. Les processus de lecture et d'acquisition des signaux de Phenix en laboratoire sont ensuite presentés. L'électronique analogique utilisée est décrite, ainsi comme le mécanisme de déclenchement et la numérisation.

Le chapitre suivant concerne les outils algorithmiques qui ont été utilisés pour la simulation du système. MGS, un code Matlab développé au laboratoire IPHC, a été adapté au cas d'un DSSD et utilisé pour la simulation du processus de collection de charge et le calcul de la réponse du détecteur. Une validation du simulateur a également été réalisée, avec la comparaison des potentiels calculés par le programme et ceux obtenus par une approche analytique, ainsi que la comparaison des impulsions calculées et de vraies mesures réalisées avec le prototype. Une brève description du modèle de simulation de l'électronique, implémenté sur Pspice, est aussi donnée.

Le $4^{ème}$ chapitre est consacré à la chaine de traitement de signal qui a été implémentée pour le calcul de l'énergie mesurée sur chaque piste. Elle est basée sur un filtrage des impulsions visant à leur donner une forme trapézoïdale. La répartition de charge et ses effets sur la mesure d'énergie sont ensuite discutés, et illustrés avec des observations sur des données réelles obtenues à partir du prototype. Une

méthode pour la calibration d'un DSSD prenant en compte la répartition de charge est aussi présentée. À la fin du chapitre, les résolutions en énergie mesurées aux énergies des sources de calibration sont presentées.

Le dernier chapitre est consacré à la détermination du point d'interaction en trois dimensions. Nous décrivons un algorithme qui calcule le nombre d'interactions d'un événement et leurs positions respectives. La méthode est basée sur une analyse simultanée du signal mesuré sur plusieurs voies, par comparaison avec un groupe de réponses pre-stockées pour une grille de points de référence. L'algorithme est utilisé tout d'abord dans une simulation pour quantifier la possibilité d'utiliser les signaux transitoires induits sur les pistes voisines de celles collectant la majorité de la charge, puis, les résultats de la méthode sont présentés. Les distributions des profondeurs de pénétration mesurées utilisant l'algorithme sont comparées avec l'absorption théorique pour les énergies des sources utilisées pour irradier le détecteur. Enfin, les images obtenues en occultant une partie du détecteur avec des différents masques sont présentées. Tout cela nous permet de valider le principe de positionnement 3D du prototype.

Chapter 1

X-ray astronomy

Although radiation in the X band was first observed in 1895[6], detection of X-rays from astronomical objects was not possible until many years later, as X-radiation does not pass through the Earth's atmosphere (figure 1.1). The first observations of X-rays above the atmosphere date back to the late 1940's and are a result of research efforts on the properties of the ionosphere by the U.S. Navy Research Laboratory (NRL), led by Herbert Friedman. The understanding of the Earth reflecting layer properties had become important since the raise of short-wave radio communications in the 1920's, when theorist E.O. Hulburt predicted that the layer ionization might be due to radiation coming from the Sun[7]. After World War II, NRL began using captured German rockets for Space Research. In 1949, a detector on board of a Viking Rocket confirmed Hulburt's theories by observing for the first time the solar X-ray spectrum [8].

The first detection of an astronomical source in the X band, other than the Sun, came in 1962 with the observation of a bright source in the Scorpio constellation, which was named Sco X-1[9]. The observation was also obtained by a detector on a sounding rocket. Two years later, on 1964, a scintillation counter flown on a balloon was able to discover the emission of the Crab Nebula supernova remnant in the hard X-ray band[10].

Although sounding rockets and balloons continue to be used nowadays, the main advances and development of X-ray astronomy came by the hand of satellite utilization. Satellites allowed to reach higher altitudes, getting rid of atmospheric absorption and enlarging the field of view. And for much longer operation times. The first satellite to detect cosmic X-rays was the American OSO-3, launched in 1967. Since then, many generations of X-rays observatories have succeeded, each contributing to the technological progress and improving our knowledge of the X-ray sky.

This introductory chapter aims at giving an overview of the state of the art in X-ray astronomy. It be-

gins by defining what we understand by X-radiation, and describing the physical processes responsible for their emission. An outline of the cosmic sources emitting in the X domain is also provided, showing the fundamental role of X-rays for astrophysics. Following, the lecture focuses on the instrumentation used for X-ray astronomy. After a brief summary of the currently operational telescopes, the principles of detection are given. Particularly, the stress is made on the working principles of semiconductor diode detectors, which are of interest for this work. Finally, the chapter ends by introducing the instrument concept that would integrate the detection system proposed in this thesis.

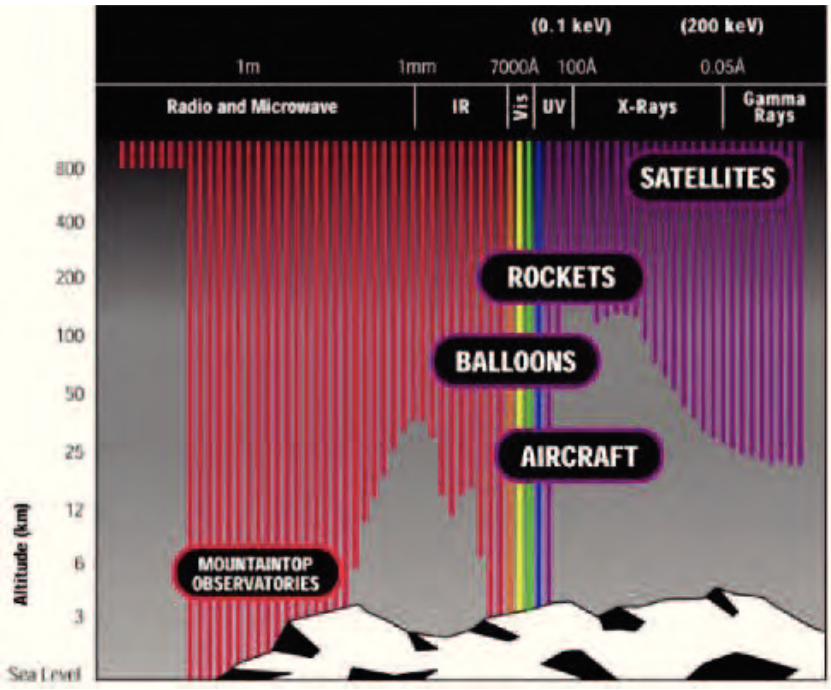

Figure 1.1: *The depth of penetration of different frequencies of light into the Earth's atmosphere, compared to typical altitudes for different types of aircraft. (*credits: NASA*)*

1.1 X-radiation

X-radiation occupies the portion of the electromagnetic spectrum corresponding to frequencies higher than those of ultra-violet (UV) radiation, but lower than gamma-rays. X-rays are more commonly described in terms of its energy rather than frequency or wavelength, and they range from a few eV to a few hundred of keV. There are no unanimous energy boundary values to separate between X-rays and gamma or UV rays. Distinction is more often based on the radiation origin. Thus, X-rays are those

originated in the rearrangement of electron shells of atoms, whereas gamma rays are a consequence of transition within the atom nucleus and UV radiation are a product of the excitation of molecular and atomic valence electrons. In addition, an arbitrary distinction is usually made between X-radiation below 10 keV, called *soft X-rays*, and above 10 keV, called *hard X-rays*.

1.1.1 Emission processes

Several physical processes lead to X-radiation. The most significant ones in astrophysics are:

- Blackbody radiation[11, p. 208]: all object at temperature greater than zero emits electromagnetic waves, due to the interactions of the thermally excited particles composing the matter. A black body is a body in thermodynamical equilibrium that absorbs all incident radiation and emits radiation whose spectrum is determined only by its temperature. At sufficiently high temperatures, this emission can happen in the X band.
- Bremmstrahlung[12, p. 14]: refers to the radiation which is emitted by electrons that are decelerated by the influence of an atom nuclei electromagnetic field. The energy loss of the electron is compensated by the emission of electromagnetic radiation, and when the energy of the electrons (i.e. electrons travelling at ultrarelativistic speeds) is high enough, that radiation is in the X-rays region of the electromagnetic spectrum.
- Synchrotron radiation[13, p. 385]: similarly to Bremmstrahlung, synchrotron radiation is produced due to the acceleration of electrons, not by other particles, but by their interaction with a magnetic field.
- Inverse Compton Scattering[14, ch. 7]: upon the collision of a photon with an electron at relativistic speed, part of the energy of the electron is transferred to the photon, promoting it to the X band. This is opposed to normal Compton scattering which leads to a loss in energy to the photon involved.
- Characteristic X-rays[12, p. 15]: are originated by the return to their normal configuration of excited electrons. In the rearrangement process of the electrons within the energy shells of the atom, an X-ray is generated whose energy corresponds to the energy difference between the initial and final electron states.
- Pair production [12, p. 53]: gamma rays exceeding twice the rest-mass energy of an electron (i.e. 1.02 MeV) may interact with matter producing simultaneously an electron and a positron. The whole photon energy is transferred to the particles as kinetic energy. The subsequent annihilation of the positron generates two photons as a secondary product of the interaction.

1.1.2 Cosmic X-ray sources

Cosmic X-rays owe their existence to a large variety of phenomena occurring in the Universe. The most relevant identified up to date are listed below (as classified in [15]).

Solar and stellar X-ray emission The X-ray emission observed from the Sun is due to the existence of hot gases (at temperatures of the order of some million degrees) in the Sun corona. Knowing that the temperature on the star surface is hardly of 6000 K, how these atmospheric gases were heated remained a mystery for more than 50 years, and it is not fully understood yet. However, a broad consensus exists that the heating of the corona is linked to the interaction of the magnetic field lines radiating out of small patches covering the entire surface of the Sun[16]. Because the laws of electromagnetism prohibit the intersection of two magnetic field lines, every time magnetic field lines come close to crossing they are "rearranged," and this magnetic reconnection continuously heats the solar corona. Many other normal stars aside from the Sun could produce X-rays by similar mechanisms.

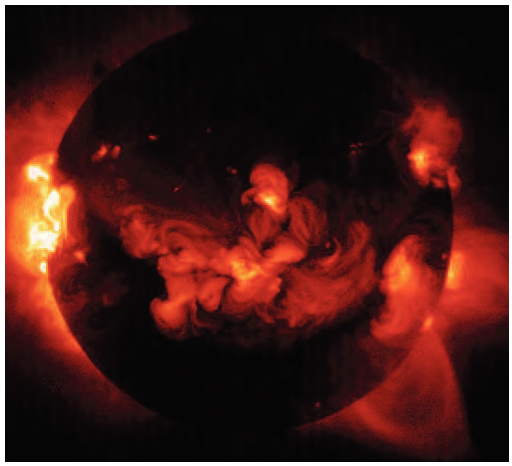

Figure 1.2: *Soft X-ray image of the Sun obtained by the Yohkoh satellite.*

Neutron stars Neutron stars are the remnants of massive stars which have burned their elements into iron. The core of the star no longer produces enough energy to withstand gravitational attraction. The core collapses and all matter is turned into a neutron gas which can maintain a stable configuration. The rotational kinetic energy of the star prior to collapse is transferred to the neutron star, which rotates very rapidly at its birth. The magnetic field of the star prior to collapse is also transferred to the neutron star and is greatly intensified.

Figure 1.3: *Artist's impression of a Neutron Star.* (Credits: ESO/L. Calçada)

The energy for the observed X-rays is thought to originate from the rotation of the neutron star (synchrotron process), or from an internal heat reservoir following formation. Rotation power can manifest itself as pulsed emission, or as nebular radiation produced by a relativistic wind of particles emitted by the neutron star. Residual heat of formation is observed as

soft X-ray emission from young neutron stars. Such thermal radiation, however, can also be produced as a result of reheating from internal or external sources. Rotation-powered pulsed and nebular X-ray emission, as well as thermal emission, can often be observed in a single object simultaneously.[17]

Supernova remnants Stars which are 8 times or more massive than our Sun end their lives in a supernova explosion. This occurs when there is no longer enough fuel for the fusion process in the core of the star to create an outward pressure which combats the inward gravitational pull of the star's great mass. At this moment, the core compresses but then recoils. The energy of the recoil is transferred to the envelope of the star, which explodes and produces a shock wave. As the shock encounters material in the star's outer layers, the material is heated, fusing to form new elements and radioactive isotopes. The shock then propels that matter out into space. The material that is exploded away from the star is known as a supernova remnant.

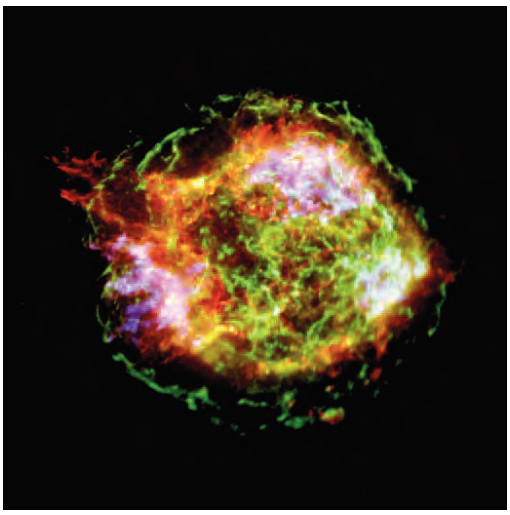

Figure 1.4: *One-million second Chandra image of the supernova remnant Cassiopeia A. (*Credit: NASA/CXC/GSFC/U.Hwang et al.*)*

The hot material given off by the supernova, the radioactive isotopes, and the free electrons moving in the strong magnetic field of the neutron stars produce X-rays and gamma rays. The emission of characteristic X-rays of the elements forming the gas allows to study their composition.[18]

Figure 1.5: *Artist conception of the binary system Cyg X-1. (*Credits: L.Cohen*)*

Binary X-ray sources X-ray binaries are systems composed of a normal star and a collapsed companion, either a neutron star or a black hole. The gas from the normal companion falls in the deep potential well of the compact object and it acquires energies of the order of 100 MeV per nucleon. This energy heats the gas as it spirals in the accretion disk and reaches the surface of the neutron star. Due to the high tempera-

ture, the gas is a fully ionized plasma which, due to its high temperature, produces X-rays. As the star rotates this produces the characteristic periodic pulsations.

Active galactic nuclei Every large galaxy, including the Milky Way, harbours a nuclear super-massive black hole. About 10 per cent of these appear to be extremely bright active galactic nuclei (AGN), with X-ray luminosities between 10^9 and 10^{13} times that of the Sun. The observed emission is explained by accretion of hot gas onto the black hole and liberation of the gravitational energy associated with this infalling matter through dissipative processes.

AGN are prodigious sources of emission across the whole electromagnetic spectrum. X-rays, however, are the most direct probe of the accretion processes responsible for this massive energy generation because they can penetrate through large columns of obscuring gas and dust associated with the accreting matter that surrounds many AGN. Moreover, X-rays are generated in the very hearts of these sources, down to distances within a few gravitational radii of the central black hole, while emission at other wavelengths is generated at distances 10^5 times or more farther out.

Figure 1.6: *Centaurus A, one of the closest galaxies with an active galactic nucleus. (*Credits: ESO*)*

AGN are the dominant sources of cosmic X-rays. In any medium-deep image of the X-ray sky at high galactic latitudes, 80 per cent of detections correspond to AGN. Until the early 1990s, the existing telescopes did not allow for most of these sources to be resolved and the X-ray sky was believed to be dominated by a diffuse cosmic X-ray radiation. [19]

X-ray background During the first discovery flight of ScoX-1 in 1962 an isotropic X-ray background was observed. This had immediate consequences for cosmology. Hoyle's Hot Universe continuous creation theory could not account for this emission, and this created a major difficulty for the theory as a whole. With the launch of UHURU in 1970 the existence of the background was confirmed and data collected with the EINSTEIN Observatory permitted to demonstrate, in 1979, that at least 25% of the background in the 0.5 to 3 keV range was due to single sources, probably quasars.

The study of active galaxies with ROSAT showed strong evidence that the in the 0.5 to 3.0 keV range some 80% of the background could be due to quasars, provided only that the background and

quasars spectral discrepancy could be explained. Recently, the CHANDRA observatory has provided enough evidence to conclude that the X-ray background radiation is largely the result of accretion onto super-massive black holes, integrated over cosmic time. The optical/near-IR identification and redshift measurement of large samples of AGN in deep pencil-beam surveys, as well as shallower wide area surveys, has provided a solid determination of the cosmic evolution of their space density at different luminosities.).

Figure 1.7: *Bullet Cluster. (*Credits: NASA/ESO*)*

X-ray emission from clusters of galaxies The discovery of high temperature plasma pervading the space between galaxies in galaxy clusters has been one of the most important discoveries of X-ray astronomy. Starting from the UHURU observations of large angular extent, there followed the determination of the thermal bremsstrahlung nature of the emitted spectrum with the first detection of plasma iron lines, the discovery of structures in the clusters emission and of binary clusters with EINSTEIN and more and more distant clusters with the ROSAT, CHANDRA and XMM-Newton Observatories.

One of the earliest findings was that the X-ray emission from the clusters was due not only to the sum of the X-ray emission from each galaxy but also (and prevalently) by the emission of the diffused gas contained by the gravitational potential of the cluster as a whole. Since this potential is much greater than that of single galaxies, the gas could be at much higher temperature (more than 10 keV rather than 1 keV). As the cluster collapses in time due to gravitational attraction, each particle in the cluster experiences a gain in energy which results in the heating to these very high temperatures. The total mass of the intergalactic gas was found to exceed by factors of 2 to 10 that of all the galaxies contained in the cluster, thus it played an important role in providing the virial mass for the cluster, although dark mass was still required for closure. Because of the large mass and high temperature, the X-ray emission from the intergalactic gas can exceed by large factors (10-100) the emission from all stars and galaxies in the cluster.

1.2 Current missions in X-ray astronomy

Several satellites carrying instruments for the observation of the X-ray band were in orbit at the time of writing. The main ones are listed below.

XMM-Newton The X-ray Mult-Mirror Mission - Newton[20], was launched by the European Space Agency (ESA) in 1999. The spacecraft carries three telescopes offering the possibility to perform extremely sensitive imaging observations over the telescope's field of view (FOV) of 30 arcmin and in the energy range from 0.15 to 15 keV with moderate spectral and angular resolution.

INTEGRAL The International Gamma-Ray Astrophysics Laboratory[21] is an ESA orbital observatory. Launched in 2002, it is dedicated to the fine spectroscopy and fine imaging of celestial gamma-ray sources in the energy range 15 keV to 10 MeV, with concurrent source monitoring in the X-ray (3-35 keV) and optical (V-band, 550 nm) energy ranges.

Figure 1.8: *Integral satellite. (*Credits: ESA*)*

Chandra The Chandra X-ray Observatory[22] is a U.S. satellite launched in 1999. It carries a high resolution mirror, two imaging detectors, and two sets of transmission gratings, covering energies from 0.1 keV to 10 keV. The telescope was designed to provide unprecedented angular resolution and imaging sensitivity, together with high spectroscopy capability.

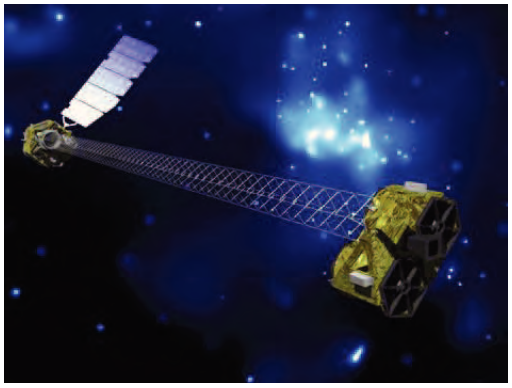

Figure 1.9: *NuStar satellite. (*Credits: NASA*)*

Suzaku Suzaku[23] is the fifth in the series of Japanese astronomy satellites devoted to observations of celestial X-ray sources. It was launched on 2005 and despite the initial success, an X-ray Spectrometer (XRS) became inoperable shortly after the launch. However, the spacecraft maintains an X-ray Imaging Spectrometer (XIS) and a Hard X-ray Detector (HXD). Suzaku instruments provide an excellent X-ray sensitivity, with high throughput over a broad-band energy range of 0.2 to 600keV.

NuStar The Nuclear Spectroscopy Telescope Array Mission[1], launched in 2012, is the first mission using focusing telescopes to image the sky in the high-energy

(5 - 80 keV) region of the electromagnetic spectrum. Due to technological limitations (see 1.4), previous orbiting telescopes did not employ focusing optics above 10 keV, so NuStar is expected to provide unprecedented sensitivity in this energy range.

Swift The Swift[24] observatory was launched in 2004, its main mission being the survey of gamma-ray bursts (GRBs) on multiple wavelengths. To do so, it is equipped with three different instruments: a wide field gamma-ray monitor and two directive telescopes, one in the UV domain and the other in the X-ray band. The X-ray telescope (XRT) is a Wolter-I type telescope composed of 12 nested mirror shells, and it covers the energy band between 0.2 keV and 10 keV.

MAXI JAXA's MAXI[25] experiment is operational since 2009 on board of the ISS. It is an all-sky X-ray monitor in the 0.5-30 keV band. The instrument performs a complete scan of the sky at every orbital period of the ISS, i.e. 96 minutes, using a combination of slit cameras and one-dimensional sensitive detectors.

1.3 Detectors in X-ray astronomy

As for any telescope, X-ray observatories are composed of two main systems: the first one, the imaging system or optics, provides a means to select the region of the sky to be observed, while obscuring the rest of directions. Depending on the type of instrument, the radiation can be directed, focused or simply allowed into the second system, the detector, which is in charge of converting the incoming photons into measurable signals. Because this thesis is focused on the operation of a particular type of detector, the purpose of this section is to be a panorama of the different detector technologies utilized in X-ray astronomy. Nevertheless, a brief mention of the different types of optics used in the field is provided first on an informative note.

1.3.1 Optics

Classical telescopes in the visible spectrum use different types of mirror and lens combinations as imaging systems. Through them, light is changed in its trajectory and focused on the spot where the detector (in this case, our eye) is expected to be. Such systems are not applicable to X-radiation because of its high energy, which would cause the rays to penetrate the lenses or mirrors without being deviated. Therefore, for many years typical imaging systems for X-ray telescopes have contented themselves with just letting in the radiation coming from the direction in space to be observed through different types of

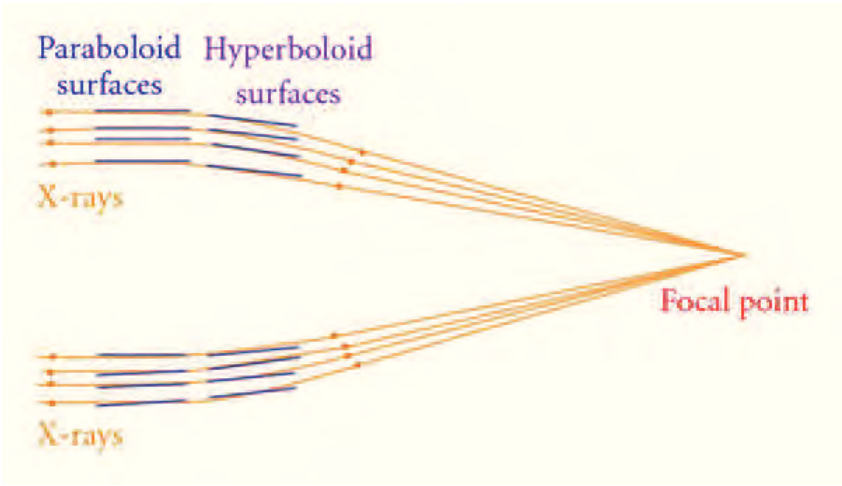

Figure 1.10: *Reflection principle in a grazing incidence Wolter I type telescope. The incoming rays are deviated by means of two (paraboloid and hyperboloid) consecutive mirrors. Multiple mirror shells may be nested in order to increase the collecting are of the telescope.*

apertures. It is the case, for instance, of collimators, where X-rays access the detector through a long and narrow tube. The longer and narrower is the collimator, the smaller is the solid angle covered by the telescope beam. Coded masks are another type of imaging systems in which radiation goes through a grid of some opaque material, with a series of apertures on it. The holes are distributed following a certain pattern to obtain a different shadow on the detector for every direction of the incoming rays. Coded Masks have been successfully used as X-ray imaging systems for the SIGMA telescope[26], the BAT instrument on board SWIFT[27], or the IBIS instrument on board INTEGRAL[28].

Collimators and coded masks are useful as systems that allow to discriminate the origin of the detected rays. However, they do not focus the incident beam. Focusing is important as a means of increasing the signal-to-noise ratio by concentrating the incident photon flux from a large collecting surface to a small spot. As mentioned, focusing through classical mirror and lens structures is not possible at X-ray energies. X-ray wavelengths are small compared to inter-atom distances, so they penetrate easily into materials. The focusing of X-radiation in astronomy is achieved using special optics called Wolter-I[29](after its inventor, Hans Wolter). In this type of telescope, the incoming rays are deviated by two successive mirrors with paraboloid and hyperboloid shapes (figure 1.10). Reflection is achieved for those photons impacting the mirror surface with very weak angles. This causes the apparent distances between atoms to be strongly reduced from the point of view of the incoming photon, thus allowing reflection.

1.3.2 X-ray detection

Unlike heavy charged particles or fast electrons, X-radiation is uncharged, so it does not interact with matter through the coulomb force. In consequence, it is possible for an X photon to go through a material without being altered and without altering the material, making impossible its detection[12, ch.2, p. 30]. For the radiation to be detected, it must first undergo some interaction process for which it transfers the totality or part of its energy to a secondary charged particle. Detection devices are designed to maximize the probability of such interactions. In the case of X-radiation, the result of the interaction is a fast electron that travels a certain distance until its energy is completely transferred to the detecting material.

Fast electrons may be a result of three main interaction processes[12, p.50]:

- Photoelectric absorption: the incoming photon is completely absorbed by an atom in the material and as a result, an electron is ejected from one of the atom bound shells.

- Compton scattering: the incident ray interacts with an electron in the material and undergoes a deflection in its trajectory. In the process, part of the energy of the photon is transferred to the electron. The transferred energy depends on the angle of deflection of the photon, varying from near-zero values for small deflection angles to a large fraction of the photon energy for backscattering photons.

- Pair production: if the radiation energy exceeds twice the rest-mass energy of the electron (1.02 MeV), the photon may interact by being replaced by an electron-positron pair. X-rays do not undergo pair production due to the high energy needed for this type of interaction, which is in the range of gamma radiation.

1.3.3 Semiconductor Diode Detectors

The detector studied in this work is a High Purity Germanium (HPGe) diode. Due to its electrical conductivity properties, Germanium enters the category of semiconductor materials. As its name suggests, a semiconductor is a material that conducts electricity worse than metals, but better than insulators. This kind of materials have been used as a medium for radiation detection since the 1960s due to their excellent spectroscopy properties.

Semiconductor properties

In semiconductors, atoms are structured in a crystal lattice where electrons are shared between adjacent atoms forming covalent bondings. Due to thermal excitation, some of those electrons may leave their position lattice and be free to migrate through the crystal, thus contributing to the material conductivity. Free electrons have higher energy than those contributing to the bondings. The energy level of the former determines the *conduction band*, while for the latter it determines the *valence band*. The two bands are separated by the *bandgap*. The bandgap is directly related to the material conductivity as it determines the amount of energy needed for an electron to pass from the valence band to the conduction band. Crystal structures are not exclusive of semiconductors and can be also found in insulators, but with much greater bandgaps.

When a electron migrates from the valence band to the conduction band, a positive charge appears in the lattice, due to the vacancy left by the electron. The pair formed by the negative charge of the electron and the positive charge of the vacancy is called an *electron-hole pair*. In absence of electric field, electron-hole pairs are constantly being created and recombining so that the electron-hole pair concentration remains stable. As electron-hole pairs are created due to thermal excitation, the concentration of electron-hole pairs increases with temperature. When an electric field is applied to the material, charge carriers undergo a net migration, with electrons and holes drifting in opposite directions. Frequently, semiconductor detectors need to be operated at low temperatures to avoid the drift of charge carriers produced by thermal excitation.

In a pure semiconductor, each electron in the conduction band leaves a hole in the valence band. As a consequence, the number of free electrons and holes is always the same. In reality, semiconductors are never found in its pure state, and an small amount of impurities is always present in the material. In addition, some interesting properties arise when intentionally doping the semiconductor with impurities of certain materials. Depending on the doping material, a N type semiconductor may be obtained, where the concentration of electrons is much larger than that of the holes; or P type, where the holes are the dominating carriers.

The ionization energy

Charged particles passing through a semiconductor transfer their energy to electrons in the lattice, resulting in the production of many electron-hole pairs along the track of the particle. The amount of energy needed to produce an electron hole pair is called the *ionization energy*, and is experimentally observed to be largely independent of the type and energy of the incident radiation. This implies that the energy of the incident radiation can be directly deduced from the measurement of the number of

produced electron-hole pairs. Semiconductor detectors have low ionization energies compared to other types of detectors, which allows for better energy resolutions. Indeed, as the number of charge carrier increases, the statistical fluctuation in the number of carriers per pulse becomes a smaller fraction of the total.

Detection principles

The basics of operation of semiconductor detectors consists in forcing the charge carriers produced by the radiation to drift towards metallic contacts (electrodes) placed at opposite boundaries of the semiconductor wafer. To do so, a difference of potential must be applied between the electrodes to create an electric field inside the semiconductor volume. However, applying an electric field to a simple N type or P type semiconductor would make the majority charge carriers (electrons or holes, respectively) drift, creating a steady-state leakage current some orders of magnitude above the typical current pulses generated by the radiation.

To reduce this leakage current, a P-N semiconductor junction must be used to obtain the typical behaviour of a diode. Through variation of the amount and type of impurities, a semiconductor can be obtained where one part presents the properties of a P type material while the other part behaves as N type. As illustrated in figure 1.11, the high gradient in the concentration of charge carriers near the junction makes some electrons to migrate from the N side to the P side. Equally, some holes migrate from the P side to the N side. This migration produce a net positive charge to appear in the N side, and a net negative charge in the p side. An associated electric field between the two sides appears as a result of this charge accumulation. As more carriers migrate, the electric field increases, opposing a resistance to the migration. At the end, an equilibrium is reached where no further migration occurs. Under these conditions the current across the junction is very low and is only due to the minority carriers, as majority carriers are blocked by the electric field.

If no additional voltage is applied, the electrical field in the P-N junction remains weak and extends only through a small region around the junction, called the depletion region. Applying an external voltage in the same direction as the natural potential difference of the junction has the effect of enhancing the electric field while at the same time enlarging the depletion region. Electron-hole pairs that are generated within the depletion region are separated by the effect of the bias voltage and drift in opposite directions towards the electrical contacts, where the induced current pulses are read out by appropriate electronics. As the depleted region is the useful region for detection, it is common for semiconductor detectors to be operated with a voltage high enough for the depleted region to extend all over the wafer thickness. In that case, the detector is said to be fully depleted.

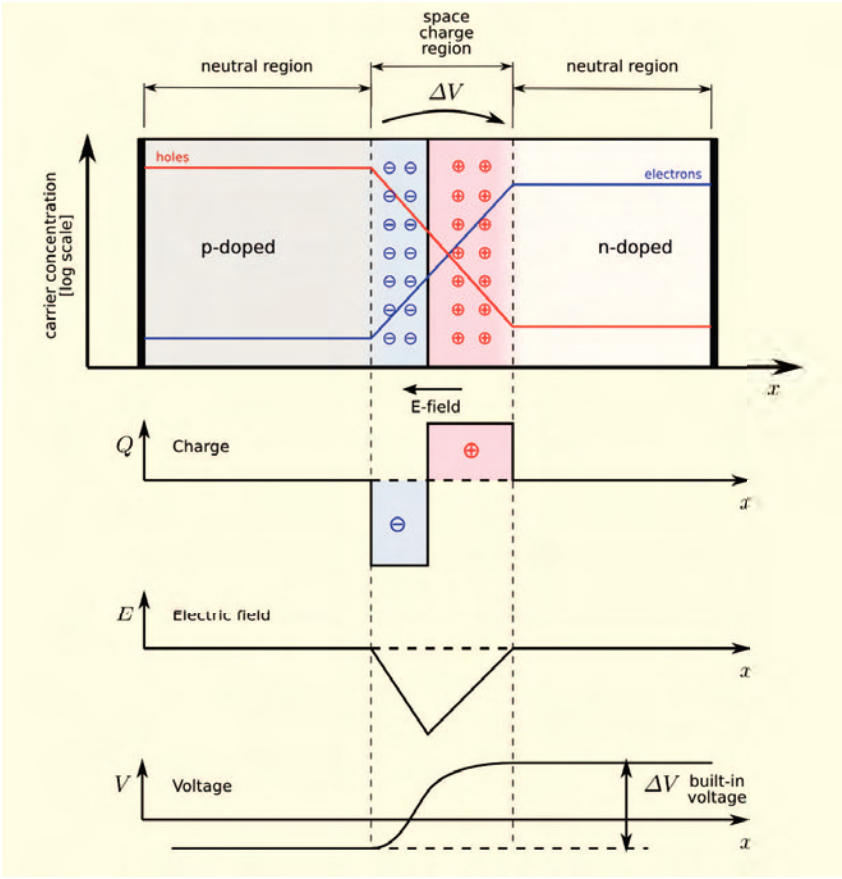

Figure 1.11: *P-N junction representation. On the top, the space charge created around the junction due to the migration of carriers. Below, plots of the resulting charge concentration, voltage and electric field profiles across the junction. No external bias voltage is applied.*

High purity Germanium detectors

P-N junctions using doped semiconductors find its application in thin detectors for the detection of radiations that penetrate short depths into the semiconductor, such as alpha particles. More penetrating radiation, such as X-rays, require thicker wafers to achieve good detection efficiency. This implies an increase of the applied bias voltage in order to maintain the device fully depleted. In fact, the voltage required to deplete a detector of thickness t is given by [12, P.387]:

$$V = \frac{eNt^2}{2\epsilon V} \tag{1.1}$$

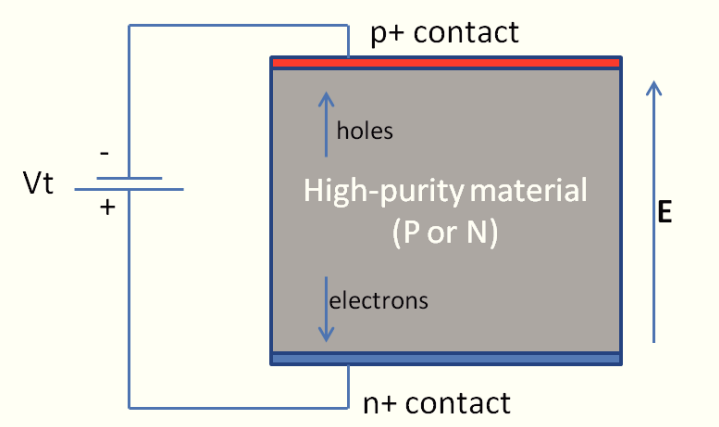

Figure 1.12: *High purity detector in planar configuration. The high-purity bulk may be of N or P type. The junction is created at the separation with the contact of opposite behaviour.*

where N is the impurity concentration of the semiconductor bulk. As V is proportional to t^2, too high voltages are needed to deplete detectors thicker than 2 or 3 mm, if semiconductors with high N (low purity) are used. A way to lower the voltage is to use a thick wafer of non doped, high-purity material, which depending on the residual impurities behaves as mildly p or n. In this case, the junction is made up by disposing just a thin layer of heavily doped material (p^+ for a N type wafer, n^+ for a P type wafer) on one face of the wafer, which acts as rectifying contact. Given that in the pure bulk of the wafer the minority charge carriers are not greatly suppressed, an additional blocking contact is provided at the opposite face. For instance, if the high-purity semiconductor is mildly N type, then a thin n^+ layer is provided. By doing so, the impurity concentration along practically all the detector thickness is that of the high purity material, and fully depletion may be attained using reasonable voltage levels. Figure 1.12 schemes a high-purity semiconductor detector in planar configuration.

The detection system studied in this work is made using High-Purity Germanium (HPGe). Techniques for the fabrication of these ultra pure crystals date back to the early 1970s and are based on zone refinement processes of polycrystalline Germanium. The impurities are progressively removed by locally heating the material and slowly passing a melted zone from one end to the sample to the other. Impurities tend to remain in the melted zone, so they can be swept from the sample. Repeating this process many times allows to attain purity levels in Germanium that have not been reached in any other semiconductor. Moreover, large crystals (up to 10 cm long[30]) can be obtained using this technique, thus making possible to build monolithic detectors of high efficiency over a broad energy range.

Application in current missions

Semiconductor diode detectors are present in various of the currently operative missions for X-ray astronomy. For instance, the SPI spectrometer on board INTEGRAL uses 19 hexagonal HPGe detectors to cover an energy range between 18 keV and 8 MeV. Another instrument of the same mission, the imager IBIS, is a CdTe pixel detector. NuStar Observatory uses four 32×32 pixel Cadmium-Zinc-Tellurium (CdZnTe, or CZT) as its imaging detectors. In addition, many of the current detectors for imaging purposes are Charged Couple Devices (CCD), which typically use semiconductors as the detecting substrate. The basic functioning of a CCD is explained in section 1.3.4. CCD cameras can be found in a diversity of missions such as Chandra, Suzaku or XMM-Newton.

1.3.4 Other types of detectors

Proportional counters

Proportional counters [12, ch.6] are gas-filled detectors, which take advantage of the *gas multiplication* phenomenon, to amplify the initial number of ions created by the interaction of a photon with the gas. A sufficiently high electric field needs to be applied to the gas for the electrons liberated in the interaction to be sufficiently accelerated and be able to create additional ion pairs when colliding with other neutral molecules in the gas. Over some region of the electric field, the gas multiplication is linear, meaning that the collected charge is proportional to the initial number of ion pars created by the incident radiation.

Scintillation detectors

Scintillation detectors[12, ch.8] take advantage of the property presented by certain materials to produce light when interacting with ionizing radiation, in a process known as *fluorescence*. The most widely used in the X-ray domain are high-density crystals of high Z-value constituents. In these types of materials, electrons are found in either one of the two following states: electrons that are bound to the crystal lattice and whose energy level determines its valence band; and electrons at higher energy that are free to migrate through the crystal contributing to its electrical conductivity. X-ray photons are detected when they interact with the lattice through photoelectric or Compton effect, generating a free electron that causes the excitation of electrons from the valence band to the conduction band. Eventually, the electrons will return to their non-excited state through emission of visible photons. Finally, an adapted sensor, such as a photomultiplier tube is used for collecting and measuring the light escaping from the scintillating material.

An example of scintillation detector is found in the spectrometer HXD[31] on board of the Suzaku observatory. The instrument cover energies from 10 keV to 600 keV using different types of detectors. Above 40 keV, detection is achieved by scintillation detectors made of Gadolinium Silicate (GSO, Gd_2SiO_5(Ce)) crystals.

The light output of a scintillator is usually collected using a photomultiplier[12, ch.9], a device consisting of a photosensitive layer, called the $photocathode$, coupled to an electron multiplier structure. The photocathode reacts to the light photons coming from the scintillating material by liberating a limited number of low-energy electrons. Amplification is achieved thanks to secondary electron emission processes occurring in the electron multiplier. The structure is a tube containing a series of electrodes in cascade, called *dynodes*. Electrons coming from the photocathode are accelerated into the first dynode. This may cause the excitation of other electrons within the dynode material, resulting in the reemission of more than one electron per incident electron towards the second dynode. Thus, the total number of electrons is amplified at each dynode stage, and the whole tube acts as a near-ideal signal amplifier.

The principles of photomultiplier tubes are used in the High Resolution Camera (HRC)[32] of the Chandra Observatory, to obtain a detector with imaging capability. Instead of a single electron multiplier tube, the instrument uses two consecutive clusters of many thousand of tubes called *micro-channel plates*. The electrons enter a different channel depending on the position of the X-ray interaction, which results on a electron cloud emerging from the rear plate. The centroid of the electron cloud is obtained using adequate readout electronics and is used for a precise calculation of the interaction position.

CCDs

Charge Coupled Devices (CCD) are widely used in modern instruments. This type of detector consists of a N type semiconductor (typically silicon) substrate with a thin layer of p doped material on its surface. Electrical contacts are implanted onto the junction and biased above the inversion threshold, forming MOS capacitors. The contacts are distributed so as to form a 2D pixel array. The detector acts in two phases: in the first phase, it is exposed to radiation and every capacitor stores charge proportional to the energy deposited by the incident radiation on each pixel; in a second phase, contacts act as a shift register, transferring its charge to the immediate adjacent pixel until reaching the last pixel of each row, where charges are read out by a charge amplifier.

The European Photon Imaging Camera (EPIC)[33] on board XMM-Newton, and the Advanced CCD Imaging Spectrometer (ACIS) on Chandra, are two examples of CCD technology applied to current X-ray astronomy instruments.

1.4 Current context in X-ray astronomy

The use of focusing telescopes in the X-ray domain has been, since very recently, constrained to soft X-rays. The Chandra Observatory, XMM-Newton, Swift or Suzaku are different examples of observatories providing focusing capabilities in this energy band. They all do so by means of grazing incidence X-ray telescopes based upon the Wolter I geometry.

The upper energy limit of all the above mentioned missions is situated around 10 keV, due to the high-energy cutoff of the grazing incidence optics. However, thanks to the use of new multilayer coating techniques[1] and longer focal lengths (achieved using a 12 meter extensible mast), the NuStar observatory, launched in 2012, has already extended the focusing capabilities up to 80 keV. This trend will be followed by the Japanese Astro-H, scheduled for 2015. At the same time, research on new mirror coatings allows to expect the extension of the focusing capabilities more and more towards higher energies[3].

In the upcoming years, several missions using focusing telescopes are planned or under study in the soft X-ray band. Such is the case of eRosita[34] which will be the primary instrument on-board the Russian "Spectrum-Roentgen-Gamma" (SRG) satellite which will be launched in 2015, or the X-IFU instrument onboard of Athena[35], a candidate for ESA's L2 mission scheduled for 2028. NASA is conducting studies for a telescope using focusing optics and a 60 meter extensible mast which aims at dramatically improve the performances offered by the current Chandra in terms of angular resolution and collecting area.

In the hard X-ray domain, the perspectives for new missions using focusing telescopes are still scarce, although preliminary studies have been carried out by NASA [36] [37], and INAF [38]. Whereas NuStar and Astro-H provide coverage up to 80 keV, no instrument with focusing capabilities exists above that energy. In order to fill this gap, and prepare future mission opportunities, the PheniX concept being developed at IRAP proposes a grazing incidence telescope with a long focal given by an extensible mast and wide energy coverage, from 1 to a few hundreds of keV.

1.5 The PheniX project

The PheniX project was presented as an answer proposal[5] to ESA's Announcement of Opportunity for its Medium-Class Science Mission, M3. Although not retained by ESA, the instrument concept received

[1] A multilayer coating consists of alternate layers of two materials with very different indices of refraction, that is, a heavy material and a light material. Examples of heavy materials used in multilayer coatings are cobalt, nickel, tungsten, and platinum. Low-density coating materials include carbon, boron carbide, and silicon. This configurations have the property of reflecting at angles of incidence larger than the critical angle of the densest materials

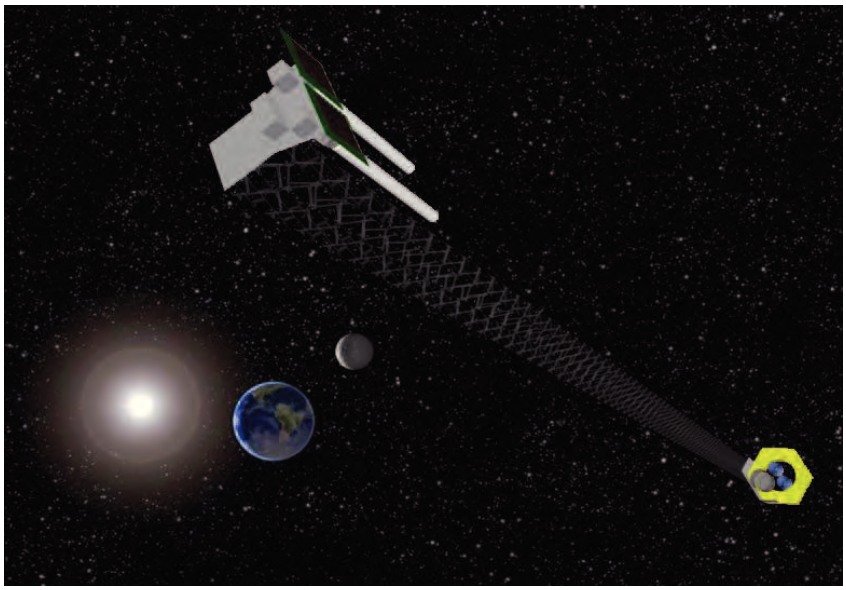

Figure 1.13: *Artist's impression of the PheniX telescope concept. The focusing optics and the detection plane are separated by a 40m deployable mast.*

attention of CNES, who provided funds for the development and study of the detector proposed in PheniX. This section is devoted to the description of the whole PheniX concept and the scientific goals that the instrument would cover.

1.5.1 Instrument design

PheniX observatory is composed of two identical coaligned telescopes in which the focusing optics and the detection plane are separated by a 40m deployable mast that provides a long focal. Figure 1.13 shows an artist impression of this design. Optics are based on depth-graded multi-layer mirrors in a Wolter-I configuration, and HPGe double sided strip detectors are used in the detection plane. The fact of having two telescopes increases the effective area, while providing redundancy. The satellite is situated in L2 orbit for thermal stability, minimization of gravity gradients on the mast and background reduction due to Earth's albedo.

The main advance of PheniX with respect to current X-ray missions is the extension of the Wolter-I focusing telescope above the 80 keV limit of NuStar and Astro-H, reaching a broad energy coverage from 1 keV to energies of the order of a few hundreds of keV and obtaining a gain of sensitivity between two and three orders of magnitude in the hard X-ray domain. To extend the focusing capability, three aspects need to be taken into account:

- As the wavelength associated with the photon decreases with the energy, the maximum grazing angle drastically reduces. This difficulty is overcome by an increase of the telescope focal length to 40m.

- As energetic photons have a higher penetrating power, the mirror coating has to be more "efficient" in order to maintain a good reflection coefficient when the photon energy increases. This is achieved by using dedicated depth-graded multi-layer coating technique.

- The increase of effective area is obtained through a large number of mirror shells. This is now feasible using light weight mirror shells such as slumped glass mirror substrate.

In the detector plane, the energy band of interest is covered with a single detector, thus avoiding the problem of cross-calibration between different instruments. The detector is a HPGe double sided strip detector (DSSD) capable of locating the photon interaction point in three dimensions, allowing for improved background rejection and polarisation measurements. The excellent spectrometry properties of Germanium yield an estimated energy resolution of about 150 eV at 6 keV, and 400 eV at 100 keV. Three dimensional location of the photon interaction point is a main feature of the instrument as it allows the reconstruction of the Compton interactions for the measurement of the radiation polarisation. In addition, being able to calculate the penetration depth of the photon is useful to reduce background by virtually adapting the thickness of the detector to the energy of the observation.

Science drivers to the instrument performance.

The choice of Germanium

HPGe presents a series of advantages with respect to other typical semiconductors used for detection purposes. Looking at table 1.1, Germanium presents low ionization energy with respect to its counterparts, thus resulting in higher energy resolution. In addition, contrary to CdTe or CdZnTe, the hole and electron mobilities are of the same order of magnitude, so the charge collection time does not vary much for events occurring at different parts of the detector. Another advantage is that it is technologically possible to grow large crystals of HPGe (several cm long and with diameters of the order of 10 cm), which is not the case for the other semiconductors. Thus, it is possible to have a single volume which efficiently collects photons of a wide range of energies. Finally, the INTEGRAL experience has shown[39] that it is possible to restore the properties of the crystal from radiation damage in space through annealing of the detector, even after many years of operation.

Material	Si	Ge	CdTe	CdZnTe
Atomic number	14	32	48,52	48,30,52
Band gap (eV)	1.12	0.67	1.44	1.57
Ionization energy (eV)	3.62	2.96	4.4	4.6
Electron mobility ($cm^2/V \cdot s$)	$2.1 \cdot 10^4$ (77K)	$3.6 \cdot 10^4(77K)$	880 (300K)[40]	960 (300K)[41]
Hole mobility ($cm^2/V \cdot s$)	$2.1 \cdot 10^4$ (77K)	$3.6 \cdot 10^4(77K)$	90 (300K)[40]	52 (300K)[41]

Data for Si, Ge, extracted from [12, p.340]

Table 1.1: *Properties of different semiconductors utilized as X-ray detectors.*

The DSSD technology

Double sided strip detectors are planar diode detectors with the particularity of having both electrodes segmented into strips. The charge collected by each strip are measured separately using a dedicated electronic readout chain. The orthogonal orientation between the anode and cathode strips defines pixels and provides the imaging capability of the device. DSSDs find applications in a variety of fields, including astrophysics[42] [43] [44], medical imaging [45] [46], nuclear physics[47] or environmental remediation [48].

The main advantage of a DSSD, compared to pixelled detectors[49], is the reduction in the number of readout channels. Indeed, a DSSD with N strips per side features N^2 pixels using only $2N$ readout channels (one per strip), compared to N^2 readout channels in a pixelled detector (one per pixel). Less electronics implies less power consumption, mass and cost, which are all major constraints in a spatial instrument. Moreover, the detection substrate being a monolithic block, DSSDs present no dead zones which maximizes the efficiency of the device. Finally, as both the current induced on the P contacts and on the N contacts are recovered, it is possible to determine the depth of the interaction from pulse timing measurements, thus obtaining a 3D location of the interaction point. 3D localization has direct applications such as background reduction or polarization measurements. In light of all these characteristics, a DSSD appears as an attractive candidate to be placed in the focal plane of a focusing telescope.

1.5.2 Scientific goals

A summary of the scientific topics that the PheniX telescope would cover (as described in [5]) is provided next.

Physics of compact objects:

The sensitivity gain provided by PheniX would allow a precise determination of the non-thermal processes at work in the vicinity of compact objects. The wide energy coverage should be beneficial for

the study of the physical links among the different emission processes: disk, thermal emission, iron line, Comptonisation, reflection, non-thermal emission, jets... In particular, the spectra of X-ray binaries above 20 keV, their cut-off energy and other properties could be studied. PheniX would enable deep studies of the hard X-ray emission of binaries in their quiescent state, that are for the moment unreachable while it would give crucial information on accretion physics at the lowest attainable rates. In addition, the huge sensitivity improvement possible with this instrument, particularly at high energies, would provide new insights on the spectral variability on short (minute) time scale and would show the evolution of the closest regions around the central engine. The non-poissonian high energy emission would be revealed and would probe the innermost disk structure. Our understanding of the Galactic central black hole emission would also benefit from the unprecedented sensitivity level.

Neutron stars- magnetic field- cyclotron lines:

Time resolved spectroscopy (and polarimetry) at ultra-high sensitivity of Anomalous X-ray Pulsars, milliseconds pulsars and magnetars would give new tools to study the role of the synchrotron processes at work in these objects. Cyclotron lines, direct measurement of magnetic filed, equation of state constraints, short bursts, giant flares... could all be studied with great detail. Transients containing neutron stars as companion would be observed over various states particularly in quiescence allowing for the first time a characterization of their spectral properties in less active phases.

AGN:

The sensitivity improvement would provide detailed spectral properties of the high energy emission of AGN's. This would give a fresh look to the connection between accretion and jet emission and would provide a new understanding of the physical processes at work (thermal Comptonisation; non-thermal synchrotron emission; hot plasma physics). This would have large implications on the robust assessment of the role of AGN energy production for the surrounding ISM in galaxies. Detection of high-redshift active nuclei in this energy range would allow to introduce an evolutionary aspect to high-energy studies of AGN, probing directly the origin of the Cosmic X-ray Background also in the non-thermal range (> 20 keV). Absorption properties would be sampled of a wide range of redshifts allowing tests of the AGN unified theory.

Element formation - Supernovae:

The energy resolution achievable for this mission (<0.5 keV) and a large high energy effective area are ideally suited for the 44Ti line study (68 and 78 keV). This radioactive nuclei emission would give an

Parameters	Requirement	Drivers
Energy range ($\Delta E/E$ FWHM)	150 eV @ 7 keV 0.5 keV @ 100 keV	X-ray binaries, AGNs (Fe line), explosive nucleosynthesis (^{44}Ti lines)
Angular resolution	Better than 30"	SNR, galactic centre region
Sensitivity (3σ, 10^5 ks) for $\Delta E/E = 0.5$	$4 \cdot 10^{-8}$ ph/cm/s/keV @ 7 keV $2 \cdot 10^{-8}$ ph/cm/s/keV @ 100 keV $15 \cdot 10^{-8}$ ph/cm/s/keV @ 200 keV	All
Polarimetry MDP	1- a few % (0.1 Crab)	Pulsars, X-rays binaries, AGNs
Time accuracy	Better than 100 μs	Pulsars
Minimal count rate without pileup	a few Crab/ $2 \cdot 10^5$ c/s	Bright sources

Table 1.2: *Instrument performance requirements related to scientific objectives.*

estimate of their quantities and speed in their environment. In addition the study of the spatial structure and spectral emission of SNR would advance our knowledge of the dynamics of supernovae explosions, of particles acceleration mechanisms and how the elements are released in the interstellar medium.

In light of the scientific goals just described, table 1.2 summarizes the targeted instrument performance for PheniX, related to their main scientific drivers.

1.6 Summary

This introductory chapter has presented the context of X-ray astronomy, as the framework for the development of the detection system presented in this thesis. In the first part of the chapter, an overview of the state of the art in the field of X-ray astronomy has been given: a brief overview of the processes at the origin of X-rays, as well as the cosmic sources emitting them, has been provided, together with an inventory of the currently operational telescopes for X-ray observation. Then, the detection principles in semiconductor diode detectors have been described. A stress has been made on HPGe based devices, as it is the technology chosen for the detector which makes the object of this work. Next, the current context in X-ray astronomy has been discussed, explaining how the technological advances in optics allow to extend the use of focusing telescopes from the soft to the hard X-rays domain. This opens an opportunity for new instrument concepts, such as PheniX, a telescope aiming at a broad energy coverage from 1 keV to a few hundreds of keV. The purpose of this thesis is to study a complete detection system, featuring spectroscopy and imaging capabilities, based on an HPGe DSSD for this telescope. In the following chapters, an in-depth description of the system is provided, focusing on the digital signal processing in use for the calculation of the energy and position of the photon interaction inside the detector volume. The implementation of these algorithms entirely in the digital domain constitute

the core of this thesis and an innovative feature of this project.

Chapter 2

The PheniX detection system

This chapter describes the detection system utilized for the acquisition of data from PheniX's HPGe doubles sided strip detector (DSSD) introduced in chapter 1. The system is based on an early digitization of the signal waveform after preamplification, thus transferring the extraction of the radiation properties to the digital domain. Due to the physical characteristics of a DSSD, the interaction of a photon often induces significant signal to more than one strip in the same electrode. In consequence, several channels need to be processed together for an optimal detection of the interaction properties. This leads to the conception of a detection system where each readout channel has a dedicated ADC, and so the waveforms of all strips are synchronously digitized and acquired in parallel.

The chapter is divided in two sections: first, a description of the working principles of a DSSD is given, focusing on the charge collection process which is responsible for the apparition of the signal on the strips; second, the PheniX experimental setup is described, from the detector itself to the digitization of the signal, and including the readout electronics. Note that only the process of signal acquisition is addressed here. The description of the signal processing for the extraction of the interaction properties, implemented in the digital domain, is deferred to chapters 4 and 5.

2.1 Working principles of a DSSD

DSSD's are one type of planar detectors. In a planar geometry, the semiconductor bulk is enclosed between two parallel plates acting as electrodes and, as in any diode detector, a difference of potential is applied between the electrodes to obtain a reverse-biased p-n junction, i. e. positive pole (anode) applied to the N side and negative pole to the P side. Under these conditions, the electric field opposes

to the migration of the majority carriers from p to n side (and vice versa), so an almost null current across the junction is achieved.

In a DSSD, instead of a single contact, each electrode is composed of an array of strips which are read separately by means of a dedicated circuit on each strip. The strips on one electrode are oriented perpendicularly with respect to the ones on the opposite side, as represented in figure 2.1. The interaction of an incoming photon through the different processes mentioned in section 1.3.2 results in the generation of a large number of electron-hole pairs, which drift towards the electrodes under the effect of the biasing field. As a result of this charge migration, electric currents are read on the electrodes. The analysis of the currents provides the two basic measurements of the detector:

- The energy deposited in the interaction.
- The x,y, z, position of the interaction.

As explained in section 1.3.3, the number of electron-hole pairs generated in an interaction can be considered to be directly proportional to the energy deposition, with proportionality factor equal to the ionization energy, ϵ, which in the case of Germanium is 2.96 eV. [12, p. 340]. Hence, the current across the diode by effect of the carriers drift accomplishes:

$$\int I(t)dt = \frac{E}{\epsilon}q \tag{2.1}$$

So, the energy deposition E is inferred from the integration of the current measured on the electrodes, $I(t)$. Contrary to a simple planar detector, where the signal of a whole electrode is read by a single circuit, in a DSSD the charges may be collected by several strips of the same electrode. This implies that, often, the currents measured on multiple channels need to be added together in order to obtain a full measurement of the energy. Note also that, in the particular case of Germanium, from the fact that the mobilities of holes and electrons are of the same order of magnitude, two energy measurements are actually obtained: one due to the collection of the electrons on the N side and the other due to the collection of the holes on the P side.

The interaction position is determined thanks to the electrode segmentation. Following the scheme in figure 2.1 (which will be used as the reference coordinate system through all this document)), the position along x dimension is obtained by identifying the strip (or strips) collecting the charge on the P side. Similarly, the position along y is deduced from the analysis of the charge collected by the N side strips. The position determination in the z dimension, or depth of interaction, is deduced form the difference in drift time between the electrons and holes, which is reflected on the apparition time of the current pulses on the electrodes.

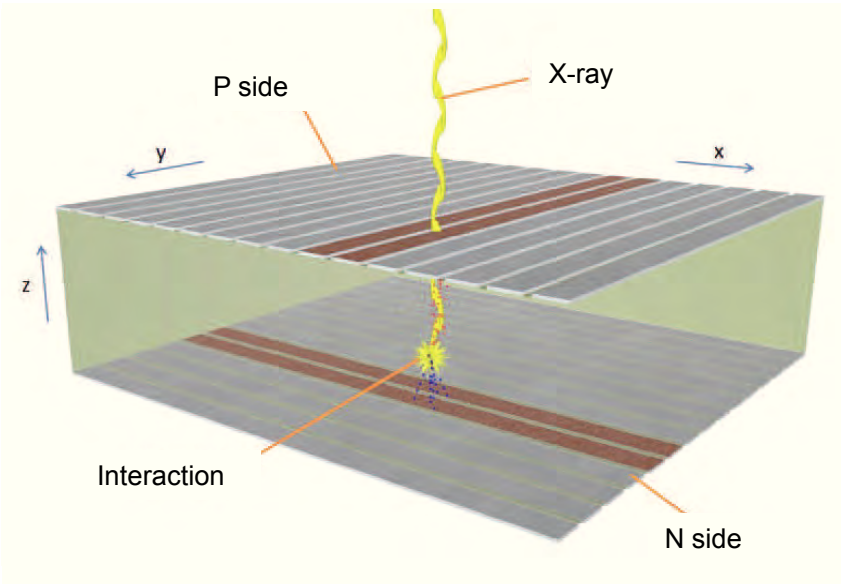

Figure 2.1: *Positioning principle of a DSDD. The sketched coordinate system is maintained as reference through all the document.*

2.1.1 The interest of 3D localization

Being able to determine the position of the interaction not only on the detector plane, but also along z is an interesting feature, as it provides a means of background rejection and, at the same time, makes possible to calculate the scattering angle in Compton events.

Background rejection

All the interactions due to particles of photons not coming from the telescope field of view form the detector background. The main sources of background to be expected for a detector on board a satellite are:

- Cosmic radiation from directions other than the observed region of the sky.
- Radioactivity of the satellite equipment, or the detector materials themselves.
- Earth's albedo.
- Photons product of the interaction of cosmic radiation with the satellite equipment.

3D localization allows the rejection of background events based on their penetration depth in the detector volume. From NIST [50], a narrow beam of monoenergetic photons with an incident intensity I_0, penetrating a layer of material with mass thickness x and density ρ, emerges with intensity I given by the exponential attenuation law:

$$I/I_0 = exp(-\mu/\rho)x \tag{2.2}$$

where μ/ρ is the mass attenuation coefficient. Mass thickness x is defined as the mass per unit area, and is obtained by multiplying the thickness t by the density ρ, i.e, $x = \rho t$. Thus, for each energy it is possible to define a thickness for which I/I_0 is sufficiently small to consider that the events detected deeper in the volume are mostly due to background coming from directions other than the telescope aperture. This way, the detector thickness can be "virtually" adapted to the optimum size for the observation of each energy and keep the detector background at a minimum.

Calculation of the Compton scattering angle

In a Compton interaction, the incoming photon undergoes a deflection from its original trajectory, as a result of transferring part of its energy to a recoil electron in the detector. The scattered photon may then interact again at another point of the sensor, thus resulting in an event with two separate energy depositions. The trajectory of the scattered photon may be defined by the azimuth angle η and scattering angle θ, as sketched in figure 2.2. Using this nomenclature, the scattering angle is related to the energies of the incoming and scattered photon through the following expression[12, p.53]:

$$\frac{hw'}{hw} = \frac{1}{1 + \frac{hw}{m_0c^2}(1 - cos\theta)} \tag{2.3}$$

where m_0c^2 is the rest mass energy of the electron (511 keV), hw and hw' are the energy of the incoming and scattered photon respectively. Note that hw is equal to the sum of both energy depositions, while hw' is equal to the energy deposited in the second interaction[1], so θ can be obtained directly from the measurement of the deposited energies.

Localizing both interaction positions in 3D allows to also calculate the scattering angle geometrically. Should the obtained angle not coincide with the one yield by expression 2.3, the event would be

[1] According to expression 2.3, below $m_0c^2/2$, i.e 255.5 keV, the energy deposited in the second interaction is always greater than in the first one. This upper limit mostly coincides with the energy range targeted by PheniX, os the identification of the first and second interaction is eased. At higher energies, the decision on whether each deposit corresponds to the first or second interaction would need to be made based on probability calculations.

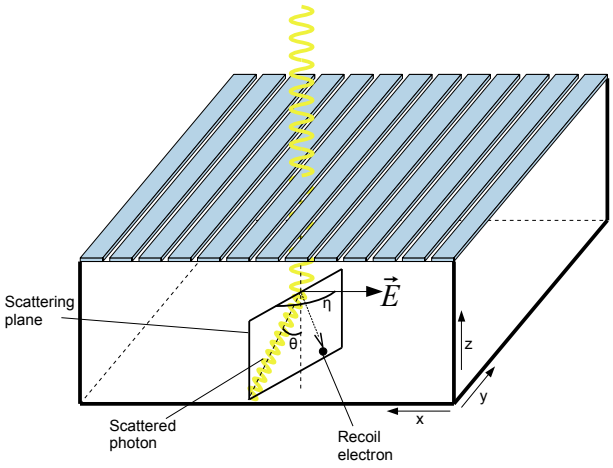

Figure 2.2: *Compton interaction in a DSSD. The direction of the scattered photon is defined by means of the θ and η angles.*

rejected as it would mean that the incoming photon arrived from a direction other than perpendicular to the detector plane. Therefore, 3D localization provides a means of background reduction also for Compton events.

Additionally, Compton scattering may be used to measure the polarization of the incident photons. For a linearly polarized beam, the scattering cross section is given by the Klein-Nishina formula [51, sec. 22]:

$$\frac{d\sigma}{d\Omega} = \frac{1}{2} r_e^2 \left(\frac{hw}{'hw} \right)^2 \left(\frac{hw'}{hw} + \frac{hw'}{hw} - 2sin^2\eta cos^2\theta \right) \tag{2.4}$$

where r_e is the classical electron radius, and θ is defined with respect to $\vec{E}$. The cross section for any other polarization is obtained from the combination of two linearly polarized distributions de-phased by 90°. Thus, the polarization of the incident radiation can be deduced from the analysis of the measured azimuth distribution of the scattered photons. This distribution is typically a sinusoid whose minimum amplitude angle coincides with the polarization angle.

2.1.2 Techniques for improving the lateral resolution

The simplest imaging system based on a DSSD has, by construction, as many pixels as intersections between anode and cathode strips. Such a system simply consists in assigning the detected event to the pixel corresponding to the intersection of strips of maximum energy. In the typical case where both electrodes are equally segmented in N strips of the same width, the total number of pixels is N^2 and the spatial resolution, or pixel size, is determined by the strip pitch. However, the effect of an interaction is never seen only by a single strip on each electrode. In fact, strictly speaking, a signal is always created on every contact of the detector, but it is strong enough to be measured only for those strips which are sufficiently close to the interaction. As a consequence, one could think of more complex imaging systems where the signal of multiple channels are analysed in order to enhance the intrinsic spatial resolution of the detector. These systems are based on the exploitation of two different phenomena: charge splitting and mirror charges.

Charge splitting

When an energy deposition takes place in the detector, a cloud of positive (holes) and negative (electrons) charge carriers is produced in the surroundings of the interaction point, whose size and shape depend on the amount of deposited energy and the type of interaction. As a first approximation, the charge cloud size can be likened to the stopping range of the recoil electron generated in the interaction.

The finite size of the charge cloud makes possible for carriers stemming from the same interaction to drift towards different strips, giving raise to what is known as charge sharing, or charge splitting phenomena. In these kind of events, the total energy deposition has to be determined through addition of the individual measurement on each strip involved in the charge collection process. Note that, as the size of the cloud charge increases with the energy of the incident photon, also does the probability of charge splitting.

A second effect responsible for charge sharing, and often more important than the initial size of the charge cloud, is the lateral diffusion underwent by the charge carriers along its path towards the electrodes, which causes the spreading of the charge cloud. The effect of diffusion can be modelled by considering that the charge seen by the electrodes follows a Gaussian distribution with standard deviation given by [52, p.55, eq. 107]:

$$\sigma = \sqrt{2D_p t} \tag{2.5}$$

where t is the drift time of the charge carriers from the interaction point to the electrodes, and D_p is a diffusion coefficient which depends on the type of material, its temperature and the bias voltage.

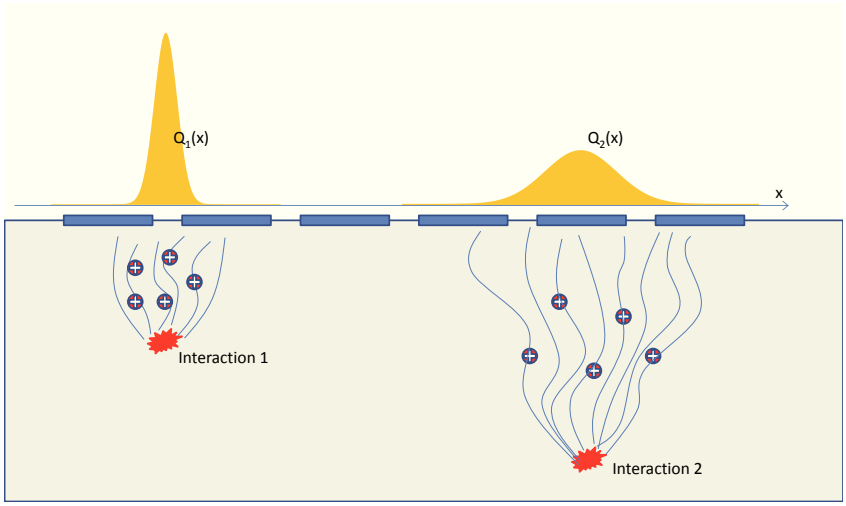

Figure 2.3: *Charge distribution on the electrodes as effect of diffusion. As the interaction moves further from the electrodes, diffusion increases.*

No clear values have been measured for D_p, but it is known that it increases with the temperature and decreases with the electric field[53]. The actual spread of the charge will then be the addition of the diffusion effect to the initial cloud size. Note that the shape of the distribution depends on the drift time (and thus, distance) from the interaction point to the electrodes (see figure 2.3).

Charge sharing can be taken advantage of for positioning purposes. If the charge distribution is expected of a certain shape, a position can be inferred from the energies calculated on several consecutive channels. Even, if no *a priori* knowledge of the distribution exists, an approximation where the energy increases linearly when the interaction approaches the strip will still provide better resolution than just assuming the position of the strip that detects the maximum energy.

Mirror charges

The Shockley-Ramo theorem[54] provides the following expression to calculate the signal induced on the electrodes due to the motion of a charged particle, q, through the detector bias electric field:

$$Q(t) = -q\varphi(\vec{r}(t)) \tag{2.6}$$

where $\vec{r}(t)$ is the trajectory of the particle in the detector volume, and $\varphi(\vec{r})$ is called the *weighting potential* of the electrode.

The weighting potential is not the real electric potential, but a mathematical artifice used for the calculation. It consists in the potential obtained when solving Poisson's equation with the electrode of interest set to potential 1, the rest of the electrodes grounded and all charges removed. Thus, the weighting potential takes values between 0 and 1 in all the detector volume, and by equation 2.6, charge is induced on all strips during the motion of the particle.

From equation 2.6 is also deduced that, at the end of the particle trajectory, the induced charge on the collecting strip (where the charge stops its trajectory) is equal to q (as the weighting potential is 1 on the strip surface), while the induced charge on the rest of the strips is 0 (as their weighting potentials are zero on the collecting strip surface). This implies that, in those strips where no net charge is collected, a transitory signal can still be measured whose duration depends on the drift time of the carriers. Such signals are referred to as *mirror charges* in this work.

Given the dimensions of PheniX the PheniX DSSD (1.1 cm thickness), and the velocity of the carriers, which is the order of 10^7 cm/s in saturation regime [12, p. 341], maximum drift times are expected to be of the order of 100 ns. Therefore, mirror charges are very fast transitory signals and its detection can be challenging if not impossible in some cases. Having said this, when detection is possible they can be used in the localization of the interaction. Indeed, as its shape and intensity are determined by the trajectory of the carriers, position information can be obtained from their analysis. In particular, mirror charges are more intense as the interaction approaches the strip, so comparing several signals from strips neighbouring the collecting strip may provide a means to determine the interaction point with a resolution better than the strip pitch. Techniques based on this principle have been successfully used for improving the spatial resolution in [55] and [45]. In order to study the usefulness of the mirror charges in our device, it is essential to know precisely the signal response of the detector due to an interaction occurring in a precise location. To fulfil this purpose, the MGS simulation tool has been used. The tool allows to build a 3D model of the detector geometry and calculate the pulses induced to the electrodes using the Shockley-Ramo theorem. This simulation is detailed in chapter 3.

2.2 Description of the system

The architecture for the signal acquisition in PheniX is outlined in figure 2.4. In the first experimental setup only the 16 most central strips of each electrode are read. As a consequence, only the interactions occurring in the zone where the two sets of 16 strips overlap are of interest. Each strip is connected to an analogue readout chain whose main purpose is the integration and amplification of the current pulse. The output of the analogue stage is fed into the trigger circuit and to a CAEN N6740 32 channel digitizer. The trigger circuit activates only when a coincidence is detected between a cathode and an

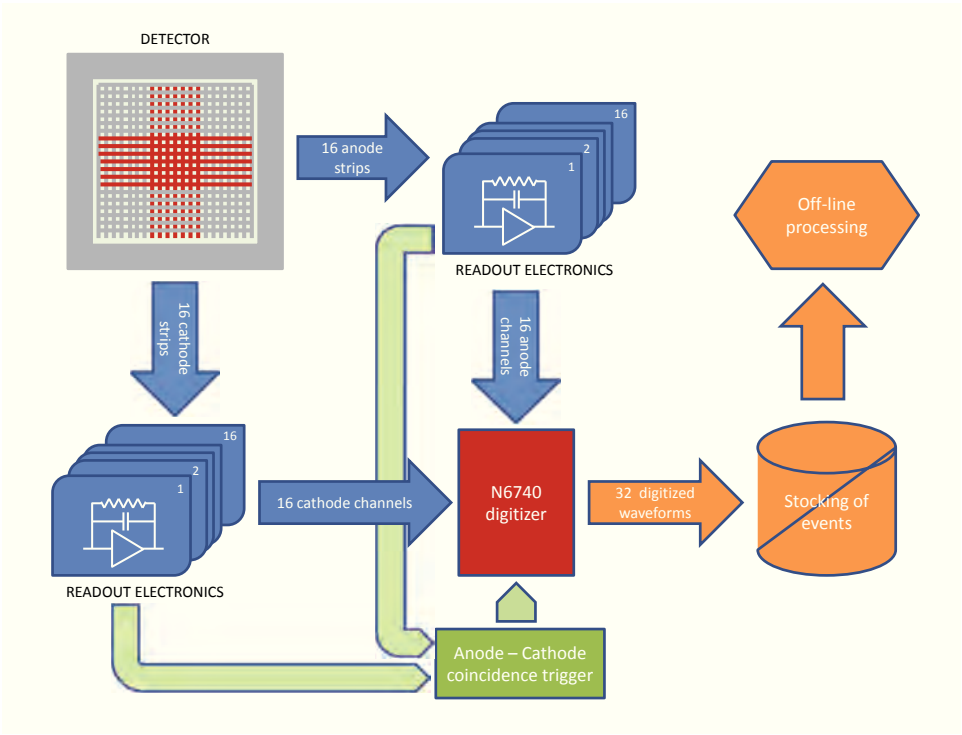

Figure 2.4: *Block diagram of the PheniX signal acquisition system.*

anode channel, so as to discriminate interactions within the zone of interest. The digitizer works in snapshot mode: upon the arrival of a trigger, it registers the waveform of all 32 channels in a pre-defined time window, so preserving the synchronization among the channels. Each obtained record is then transferred to a PC for off-line processing in the digital domain.

2.2.1 Detector

The PheniX detector prototype (figure 2.5) was manufactured by Canberra France. It consists of a 11 mm thick HPGe wafer, with a 4x4 cm useful surface of detection. Canberra specifies a concentration of impurities which varies from $1.11 \cdot 10^{10} cm^{-3}$ to $1.68 \cdot 10^{10} cm^{-3}$. The nature of the crystal, P type or N type, as well as the specific material used in the P-N junction, were not disclosed. The electrodes on both sides were implanted by lithography of aluminium and are segmented into 100, 40 mm long, 350 μm wide strips, with a 50 μm gap between strips, thus defining square pixels of 400 μm per side. The thickness of the electrodes is inferior to 2 μm. Both at the anode and the cathode, strips are surrounded by a 3 mm wide guard ring, to avoid deformations of the electric field on the outer most strips due to

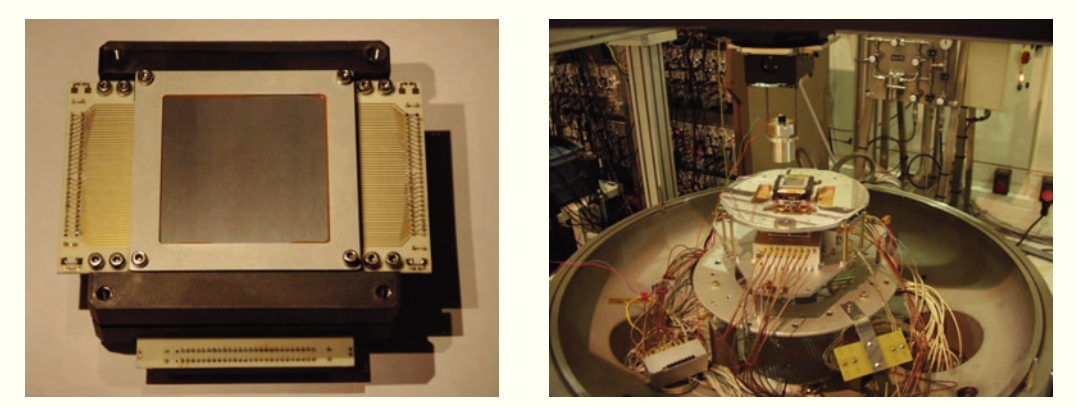

Figure 2.5: *The PheniX detector prototype. On the left, image of the detector as delivered by the manufacturer. On the right, the detector in its experimental setup.*

border effects.

The detector is encapsulated in a Vespel structure as shown in figure 2.7. A 300 μm thick beryllium window covers the detection surface on both sides of the detector. Electric connexion to the strips is implemented by means of four 64 pin Omnetics connectors, placed in line with the strip ends in order to minimize the length of the wires bounding the strip with the connector. Aluminium wires are used for this purpose (figure 2.6). Half of the strips of a detector face are directed towards a connector while the other half are directed to the connector on the opposite end of the strips. The distribution of the strips is made so as consecutive strips are wired to different connectors. This means that, if the strips of one electrode are numbered from left to right, the even strips are wired to a connector while the odd ones are wired to the opposite connector. As a consequence, in the present 32 channel configuration, each connector provides the output of 8 operative channels. All pins are oriented towards the N side of the diode so that all read-out electronics can be placed on that side, letting the P side free for irradiation.

The detector is mounted on a cold plateau as shown in figure 2.8. A "cold finger" refrigerated using a liquid nitrogen system, is used to lower the temperature of the plateau. Germanium detectors are usually operated at a nominal temperature of 77K[12, p.395], in order to lower the leakage current and prevent it from degrading the energy resolution. Unfortunately, such low temperature can not be attained with the current setup. Instead, a temperature of 115 K is measured on the PCB supporting the connectors. A second plateau at 200K supports the preamplifiers boxes, as well as the high voltage board providing the bias voltage to the detector. The whole setup is contained in a vacuum chamber equipped with a pump system able to attain a pressure of 10^{-7} mbar.

The leakage current is measured by inter-connecting all the strips on each electrode. A voltage of 1750V, equivalent to the bias voltage of operation, is applied to the N side. An ammeter is used to

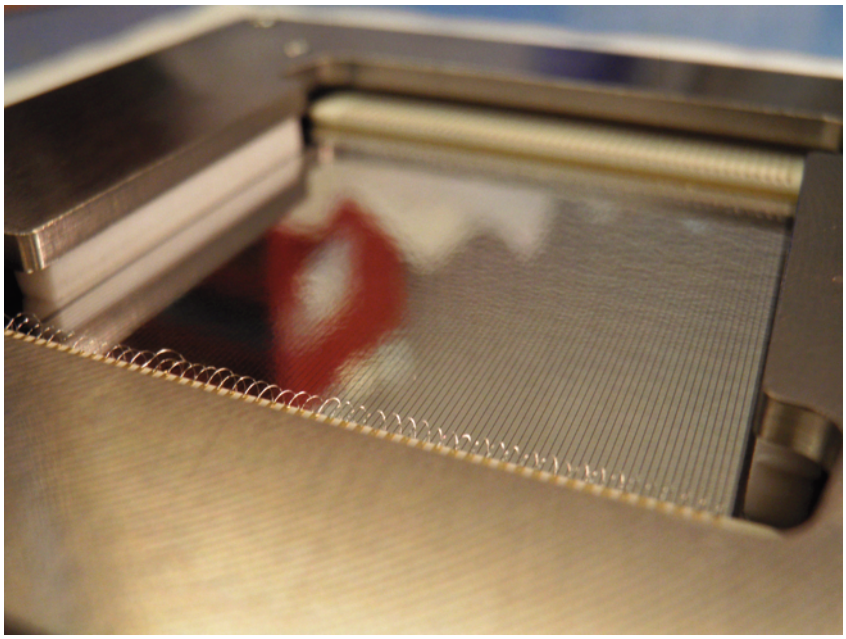

Figure 2.6: *Detail of the wires bounding the detector strips and the connector PCB.*

measure the current on the N side, yielding a value of 200 pA. This current must be divided by the number of strips on the electrode, so the leakage current per strip is estimated of the order of 2 pA. The measurement was carried out at a temperature of 107K.

2.2.2 Electrical interface and electronics

The interface between the detector and the readout electronics is illustrated in figure 2.9. Readout electronics have the function of converting the weak current pulses generated by the detector into voltage pulses suitable for digitization. An operational amplifier in charge-sensitive configuration constitutes the main stage of the readout chain. The readout of the 32 operative channels is grouped in four groups of eight, which concur with the outputs of the 4 Omnetics connectors in the detector. Recall that all the channels from the same connector correspond to the even or odd strips of the same electrode (N or P). The N side channels are directly connected (DC coupled) to the charge amplifier input, while on the P side the Omnetics connector and the amplifiers are interfaced through a High Tension (HT) distribution board, which provides the bias voltage to the sensor. A depletion voltage of 1200 V is specified by Canberra. However, the detector is operated overdepleted at a tension of 1750 V in order to attain the

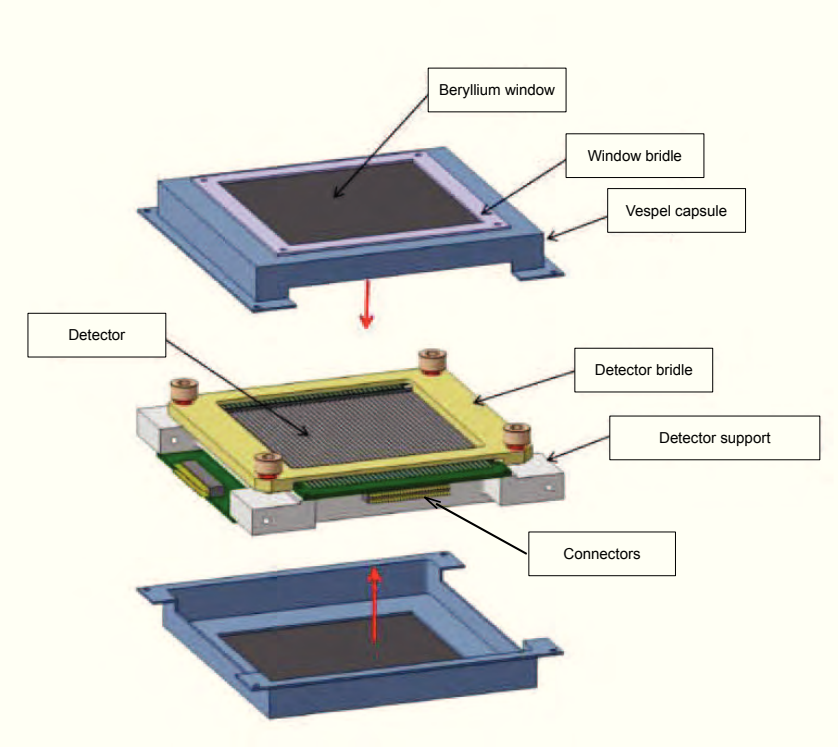

Figure 2.7: *Encapsulation of the PheniX detector. Detail of the vespel structure, the beryllium window and the connectors is given.*

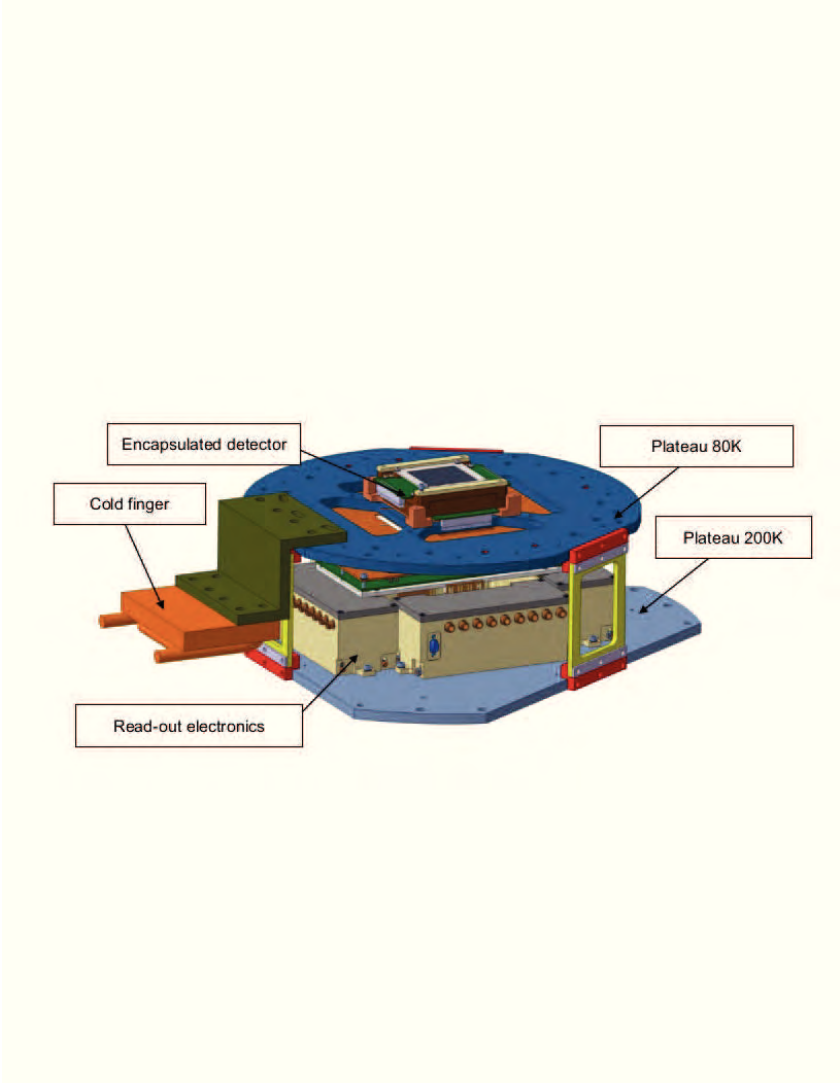

Figure 2.8: *Detector mounted on the cold plateau. Below, a second plateau supports the read-out electronics.*

regime of carrier velocity saturation[2]. In order to operate in reverse polarization, a tension of -1750 V is applied with respect to the 0V on the N side. The output of the HT distribution board is AC coupled to the amplifiers input in order to isolate them from the polarization voltage.

The signals coming from the detector (or the HT board) are fed to 4 boxes, each containing the charge-sensitive amplifiers for 8 channels. After amplification, a second board accomplishes three purposes: provide further amplification of the signal, remove the offset introduced by the charge amplifier, and generate a signal which is the sum of the 8 channels, for trigger purposes. Finally, the output signals of the second board are fed into a 32 channel digitizer.

Preamplification is usually the first stage of the electronic chain and is performed as close as possible from the detector to minimize losses and capacitive loading on the signal before amplification. It has the function of converting the weak current pulses generated by the detector into measurable voltage pulses for the subsequent stages. In semiconductor diode detectors, preamplification is typically achieved by means of an operational amplifier in charge sensitive configuration. Given that it is the first stage in the readout chain, the noise figure of the operational amplifier has a critical impact on the performance of the system. The Amptek A250F device has been chosen for PheniX, for its excellent noise performances. The device is encapsulated with internal circuitry as shown in figure 2.10, which is extracted from Amptek website[56]. The internal input FET is included to provide high input impedance.

The response of the circuit in the figure is calculated using Laplace transform:

$$V_0(s) = \frac{-1}{C_f}\frac{1}{s+1/R_fC_f}I(s) \quad \xrightarrow{\mathcal{L}^{-1}} \quad v_0(t) = -\frac{e^{-t/\tau}}{C_f} * \int_0^t e^{u/\tau} i(u)du \tag{2.7}$$

where $\tau = R_fC_f$ is the decay time constant of the amplifier. Let $i(t)$ be a current pulse of duration T_I, if $T_I << \tau$, then $e^{t/\tau} \approx 1$ for $t < T_I$. The previous equation can then be simplified to:

$$v_0(t) = -\frac{e^{-t/\tau}}{C_f} * \int_0^t i(u)du = \frac{Q}{C_f}e^{-t/\tau} \tag{2.8}$$

where Q is the area of the current pulse, which is equal to the charge collected by the strip (equation 2.1). The current pulse is therefore converted into a voltage pulse whose amplitude is proportional to the energy deposited by the interaction. The feedback $1G\Omega$ resistance and $0.25pF$ capacitor determine a time decay constant $\tau = 250\mu s$, so it is effectively much longer than the duration of the current pulse, which is of the order of 100 ns.

[2]Drift velocity saturation is of interest as it minimizes the charge collection time and charge losses due to recombination and trapping. Saturation drift velocities are reached with electric fields above 10^3 V/cm for electrons and fields three to five times higher for holes[12, p. 389]. Therefore, considering the 11 mm thickness of the detector, the saturation regime is attained for electrons, while for holes, a situation of near-saturation is expected.

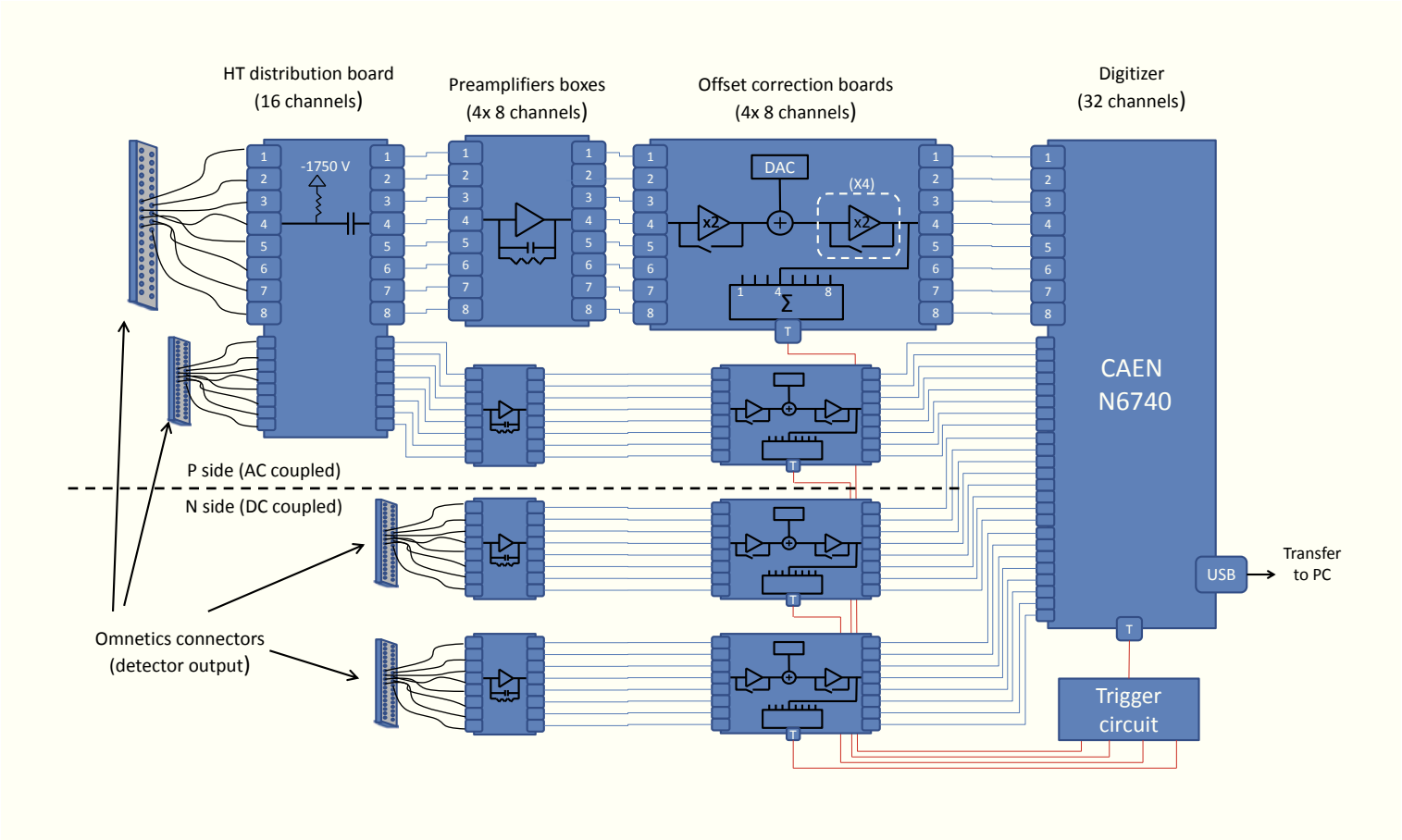

Figure 2.9: *Scheme of the readout electronics and their connexion with the detector. The readout of one set of 8 channels from the same connector is zoomed for more detail.*

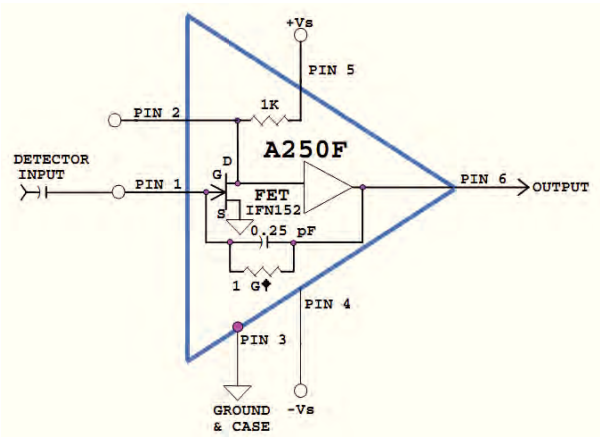

Figure 2.10: *Amptek A250F encapsulation.*

A simple non inverting 2x multiplier is implemented after the charge sensitive amplifier to provide further amplification to the output signal.

In order to assess the noise performance of the amplifiers, the degradation in energy resolution was measured using a pulse generator at their input. The degradation was of the order of 1 keV at 20^{o}C, and 0.7 keV at -80^{o}C. The measurement was obtained with a Gaussian shaping (4 μs peaking time) after the charge sensitive amplifier.

Offset correction board and trigger generation

The second board after the preamplification stage removes the continuum component introduced by the A250F. At the same time, the board provides several amplification stages whose gain can be switched from x1 to x2. This allows to modify the final gain of the readout electronic chain, in order to best adapt it to the input dynamic range of the digitizer.

The continuum value to be removed from each channel is calculated in the digital domain based on previously acquired data, and fed into the offset correction board by means of a digital to analogue converter (DAC). The amplifier prior to the offset subtraction provides high input impedance to the whole circuit and can act as a simple voltage follower or as a x2 multiplier depending on a switch position. After removal of the continuum value, the successive amplification stages allow the variation of the total gain of the board by multiples of 2 from x1 to x32.

Finally, the board provides a circuit to calculate a signal by addition of the 8 channels. This signal is used for triggering purposes, in combination with its counterparts from the other boards. In order to

select events that occur in the overlapping zone between the 16 anode and 16 cathode operational strips, the 4 trigger signals are combined as follows to generate the final trigger, T_F:

$$T_F = (T_{A,even} \oplus T_{A,odd}) \odot (T_{C,even} \oplus T_{C,odd}) \tag{2.9}$$

where T_x are the four trigger signals from each set of 8 channels. sub-indexes A and C correspond to anode and cathode, respectively, and sub-indexes odd and $even$ refer to the odd or even subgroup of channels.

2.2.3 Digitization

All signals are sampled using a CAEN N6740 digitizer[57]. The module features 32, 12 bit analogue-to-digital converters with a 2Vpp dynamic range. The digitizer works in snapshot mode, meaning that for each arrival of a trigger, a record (*event* from here on) is created containing the waveforms of all 32 channels in a time window of pre-defined length. The device allows the user to configure the number of samples to store before and after the trigger, which are common for all channels, thus maintaining the synchronization among all channels in the digital domain. Digitized waveforms are transferred via an USB link to a PC, where they are stored for off-line processing.

2.2.4 From the current laboratory setup to a real mission

The detection system described in this chapter has the purpose of studying the best possible performances of the detector in a laboratory environment. For this reason, no effort have been made yet to optimize the system in terms of data storage or time of data processing. The signal processing in the digital domain is carried out in an event-by-event basis, with no loss of information from the analogue domain, as the waveforms from all channels are preserved. This demands lot of storage capacity. At the same time, the signal processing algorithms described in chapters 4 and 5, try to optimize the spectroscopic and imaging performances, regardless of the calculation time.

In an eventual development for a real satellite mission, it is clear that the current system would need to be adapted taking into account the particular constraints of an on-board experiment. A more sophisticated (and selective) trigger system would need to be used in order to reduce the number of electronic channels to process on each event. At the same time, compromises would need to be made on the implementation of the algorithms in order to adapt them to the processing of data in real time using FPGAs. The trade-off between the computational cost of the signal processing and their required performances in regard of the scientific objectives of the mission is beyond the scope of this work.

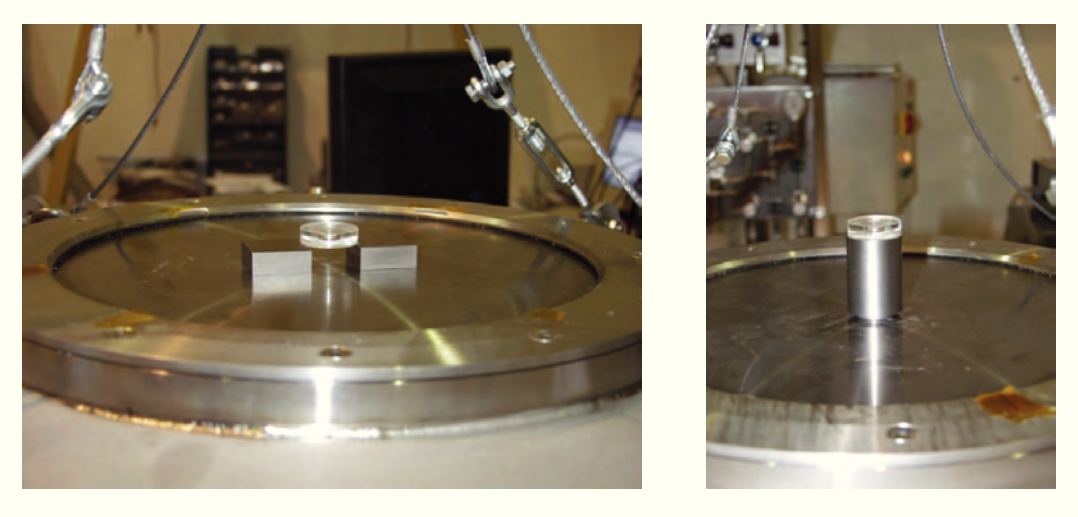

Figure 2.11: *Irradiation of the detector with a ^{241}Am source, during the tests of the prototype. On the left, direct irradiation, on the right, irradiation through a collimator. Figures 5.13 and 5.15, respectively, correspond to the obtained images after data processing.*

2.2.5 Test Conditions

For the first campaign of measurements with the prototype (which includes all the results presented throughout this thesis), a means to precisely position the radioactive sources used to irradiate the detector (such as a controlled XY table) was not available. In consequence, we had to content ourselves with very simple setups, where the sources are simply placed against the window of the vacuum chamber, or they are suspended on some support above different types of collimators and masks (Figure 2.11) Two different sources, ^{241}Am (with a main spectral line at 59.5 keV and ^{57}Co (122 keV) were used for this experiments.

2.3 Summary

This chapter is divided in two sections: first, the working principles of a DSSD are detailed; second, the experimental setup used for the readout, digitization and storage of the detector signals is described.

The localization of the interaction in a DSSD can be performed in the three dimensions. In the xy plane, the position is determined thanks to the pixellization provided by the segmentation of the electrodes. The interaction depth, along z axis, can be calculated from the difference in the timing measurements between the anode and the cathode pulses. The interest of 3D localization is twofold. On

the one hand, it may be used to reject part of the background seen by the detector; on the other hand, it allows polarization measurements through reconstruction of the Compton angle in double events.

Two phenomena, charge sharing among multiple strips and the transient mirror charges on the non-collecting strips, can be used to improve the intrinsic spatial resolution of the detector. For this, an algorithm capable of simultaneously analysing the waveforms of multiple strips is needed. The PheniX acquisition system has been conceived to make possible such an analysis. In the description of the system provided in this chapter, the geometry, characteristics and operation conditions of the detector have been given. The interface between the detector and the readout electronics has been detailed. These readout electronics mainly consist in an amplification stage which converts the weak current pulses which appear on the detector strips into voltage pulses suitable for digitization. A common trigger is used for the synchronous digitization of all channels, which are then stored in an event-by-event basis for off-line processing in the digital domain. This acquisition system is simulated using the software tools described in next chapter, whereas the signal processing algorithms for the calculation of the energy and position of the interaction will be the subjects of chapters 4 and 5.

Chapter 3

Software simulation of the PheniX detection system

The simulation of the detector response is of great importance. On the one hand, it allows the validation and the assessment of performances of the pulse shape analysis that will be described in the following chapters; on the other hand, in some algorithms, being able to calculate the signal response for a precise interaction point is a necessary feature for solving the interaction position. This the case for the *matrix method* presented in chapter 5. In such methods, the determination of the interaction position is based on a comparison between the signal measured on the strips, and a set of pre-stored responses for a grid of basis points.

MGS[58], a Matlab-based software developed in the IPHC in the frame of the AGATA[59] project was used to simulate the response of the PheniX detector. In a first section, this chapter describes the working principles of MGS, as well as the work that has been done to validate the tool for the DSSD case. Next, the Pspice model that was developed to simulate the analogue electronics used for the readout of the signal on each strip is detailed. The implementation of this Pspice circuit was done by a Master student in the framework of his Master Thesis [60].

The coupling of MGS with the Pspice simulation allows to obtain realistic signals, emulating those measured on the real prototype. In order to assess the accuracy of the simulation, the calculated pulse shapes were compared with those provided by the detector, for different depths of interaction. The results of the comparison are reported at the end of the chapter, and have also made the object of a publication[61] in *Nuclear Instruments and Methods in Physics Review A* (appendix B).

3.1 Simulation of the detector response with MGS

In order to simulate the signal response of the detector, the *MGS* software tool is used. This Matlab code was developed and validated in the *Institut Pluridisciplinaire Hubert Curien* (IPHC) of Strasbourg, in the frame of the project AGATA. MGS stands for *multi geometry simulation*, referring to the ability of the program to simulate solid state detectors of varied geometries. The program performs an analysis by finite elements of the detector, and uses numerical methods to solve the electric potential in the sensor volume and calculate the trajectory of the charge carriers and the signal induced to the electrodes.

3.1.1 Working principles

Unlike other tools such as Geant4, MGS does not aim at an accurate simulation of the physical processes taking place in the photon-matter interaction. Instead, it focuses on the electron-hole pair collection process and the synthesis of the current pulses induced at the electrodes by the motion of the charges. The program lets the user define the three dimensional position of the interaction, which is simplified to a single pair of positive and negative point-like charges carrying the whole deposited energy. The trajectory of the particles under the effect of the bias voltage is then computed and the shape of the electrode pulses are obtained through application of the Shockley-Ramo theorem[54]. The characterization of a detector in MGS is done through several calculation stages:

1. Definition of the geometry of the detector and its working parameters.
2. Solution of the electric potential for all the volume.
3. Calculation of the electric field.
4. Obtaining the velocity vector applied to the charge carriers at every point of the detector volume.
5. Calculation of the weighting potentials.

These are necessary steps for the determination of the charge carrier trajectories and signal response. After they have been performed, the user can define an interaction at any point of the detector volume. The program then places an electron-hole pair at that position, calculates the path of the charges from the interaction point to their respective electrodes (electron drifting towards the N side and hole drifting towards the P side), and uses these trajectories to determine the signal response of each electrode through application of the Shockley-Ramo theorem. Note that MGS simplifies the cloud of charge carriers that would appear in a real interaction to a single electron-hole pair carrying the whole energy of the photon.

Further detail on each of the listed steps of the simulation is provided next. The explanation of the weighting potential is grouped together with the charge carrier trajectory calculation and Shockley-Ramo theorem for a better understanding.

3.1.2 Definition of the geometry

The program uses a grid, a matrix of points in space, to represent the volume corresponding to the detector. The detector geometry is defined using several layers. Each one identifies the points of the grid corresponding to a part of the detector. There are 5 different layers: semiconductor bulk, anode, cathode (with their corresponding guard rings), isolating material surrounding the detector, and external capsule. In order to obtain a desired geometry, the user has just to choose among several pre-defined templates, each one corresponding to a common detector type, and enter the dimensioning parameters. For instance, some of the required parameters for the planar template –used for defining a DSSD– are: detector dimensions, number of strips per side, width of the strips, separation between strips, etc. An example plot of this template is shown at figure 3.1, where, for the sake of the figure clarity, the electrodes are segmented in only 10 strips (thus not corresponding with the real geometry of the PheniX prototype). The guard ring surrounding the electrodes can also be distinguished. A great advantage of this approach is that the template completely defines the detector, and the code is transparent to the chosen geometry for all subsequent steps of the simulation. This means that it is possible for a user to simulate a new type of detector just by creating the appropriate template, without having to modify the rest of the code.

3.1.3 Calculation of the electric potential and electric field

When an energy deposition occurs in the detector, a cloud of positive (holes) and negative (electrons) charge carriers is produced in the surroundings of the interaction point, whose size and shape depend on the deposited energy and the type of interaction. These charged particles immediately drift towards the electric contacts, as a result of the electric field produced by the bias voltage applied to the electrodes. Therefore, to determine the trajectory of the carriers, the first step consists in computing the electric potential inside the detector. This is done by solving Poisson's equation:

$$\nabla^2 \phi = -\frac{\rho}{\epsilon} \tag{3.1}$$

The boundary conditions of the problem are given by the bias voltage applied between the electrodes, and the grounding of the outer-most points of the grid, simulating an encapsulated detector. The

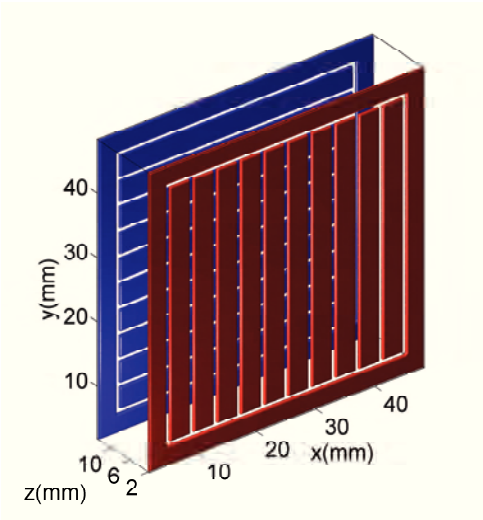

Figure 3.1: *Example of a DSSD geometry represented with MGS. Both electrodes are segmented in 10, 3.5 mm wide strips, with a 50 mm gap between strips. The sensor thickness is 11 mm.*

intrinsic space charge density in the bulk is proportional to the density of acceptors or donors in the P or N type detector material. The user has to define the concentration of impurities at the two extremes of the bulk (near cathode and near anode), which in the case of the PheniX detector are specified by Canberra (concentration varying between 1.11 cm^{-3} and 1.68 cm^{-3}). This way, a gradient of space charge density along the crystal is considered. The discrete version of the electric potential, u(i,j,k), is defined as follows:

$$u(i,j,k) = \phi(x_i, y_j, z_k)$$

where

$$x_i = i \cdot \Delta_x \qquad y_j = j \cdot \Delta_y \qquad z_k = k \cdot \Delta_z$$

and Δ_x, Δ_y and Δ_z are the distances between points of the grid (or grid step) in the three dimensions. The derivative operator is converted to finite differences as follows (for x dimension, and analogous for the other dimensions):

$$\frac{\delta\phi(x,y,z)}{\delta x} \longrightarrow \frac{\phi(x+\Delta_x/2,y,z) - \phi(x-\Delta_x/2,y,z)}{\Delta_x}$$

and so the second derivative:

$$\frac{\delta^2\phi(x,y,z)}{\delta x^2} \longrightarrow \frac{\phi(x+\Delta_x/2)+\Delta_x/2,y,z)-\phi((x+\Delta_x/2)-\Delta_x/2,y,z)}{\Delta_x^2}$$
$$-\frac{\phi((x-\Delta_x/2)+\Delta_x/2,y,z)-\phi((x-\Delta_x/2)-\Delta_x/2,y,z)}{\Delta_x^2} =$$
$$\frac{\phi(x+\Delta_x,y,z)-2\phi(x,y,z)+\phi(x-\Delta_x,y,z)}{\Delta_x^2} = \frac{u(i+1,j,k)-2u(i,j,k)+u(i-1,j,k)}{\Delta_x^2}$$

The finite differences version of equation 3.1 is then:

$$\frac{u(i+1,j,k)+u(i-1,j,k)}{\Delta_x^2}+\frac{u(i,j+1,k)+u(i,j-1,k)}{\Delta_y^2}$$
$$+\frac{u(i,j,k+1)+u(i,j,k-1)}{\Delta_z^2}-\frac{2u(i,j,k)}{\Delta_x^2+\Delta_y^2+\Delta_z^2}=-\frac{\rho(i,j,k)}{\epsilon}$$

If the equation is formulated for every point of the grid, the number of equations is equal to the total number of points in the grid, resulting in a determined system of linear equations. MGS allows for a direct solution of the system provided the computer has enough memory. Otherwise, two iterative methods are implemented: *Jacobi's method*[62, p.892] and *successive over relaxation (SOR)*[63]. The number of iterations required by SOR to converge is proportional to N, with N being the total number of grid points, while Jacobi's method converges with a number of iterations proportional to N^2. So SOR is usually faster. Figure 3.2 shows the potential obtained for the same detector example of figure 3.1, while figure 3.3 shows a comparison of the obtained potential between a DSSD and a non segmented parallel plate detector in the region near the electrodes, showing the effect of the segmentation on the field lines. After solution of the electric potential, the electric field is obtained from the negative gradient:

$$\vec{E}(i,j,k) = -grad(u(i,j,k))$$

3.1.4 Obtaining the velocity vector

The electric field is used for calculating the drift velocity vector matrices for positive and negative charge carriers. That is, for each point of the grid, the velocity vector that would be applied to a charged particle at that point is determined. At low electric fields (below approximately 100 V/cm for Germanium), drift velocities are directly proportional to the electric field with a mobility coefficient

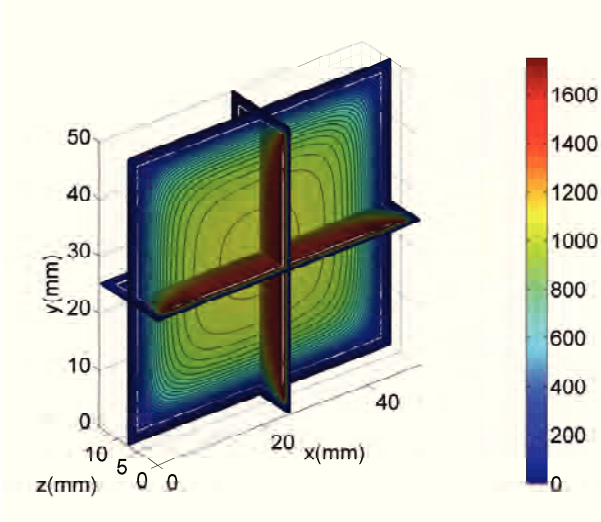

Figure 3.2: *Perspective view of the electric potential of a DSSD, as calculated by MGS.*

μ, which is different for holes and electrons. At higher electric fields, this linear relationship is lost and drift velocities increase slower with the field value, until reaching a maximum saturation velocity. This is the most usual operating mode for the investigated type of detectors (and it is also the case for our prototype). The mobility of the carriers is simulated in MGS by means of two models: the first, developed by Mihailescu et al.[64], accounts for the mobility of electrons, and the second, by Bruyneel[65], accounts for the mobility of holes. These models take into account anisotropy effects on the charge transport, due to the orientation of the semiconductor lattice. However, they do not consider the *Gunn effect*, observed by Ottaviani et al.[66] for high electric fields, above 3 kV/cm. This has no serious implications for our application, as our detector is operating at a voltage well below this threshold. The models assume a lattice temperature of 78 K, which is commonly used for Germanium. However, our detector is operating at 110 K. A difference in charge carrier velocity was expected from this difference in temperature, so we have modified the MGS code by re-scaling the calculated drift velocities, according the expressions for saturation velocity as a function of temperature given in [67].

3.1.5 Charge carrier trajectory, Shockley-Ramo theorem and weighting potentials

Using the drift velocity matrices, the program is able to compute the trajectory of point-like charges of either polarity drifting from the interaction point to the electric contacts. The actual charge cloud is modelled by a single positive and negative pair of particles whose charge is equivalent to the deposited energy. The interaction point does not need to belong to the grid, as the program interpolates the

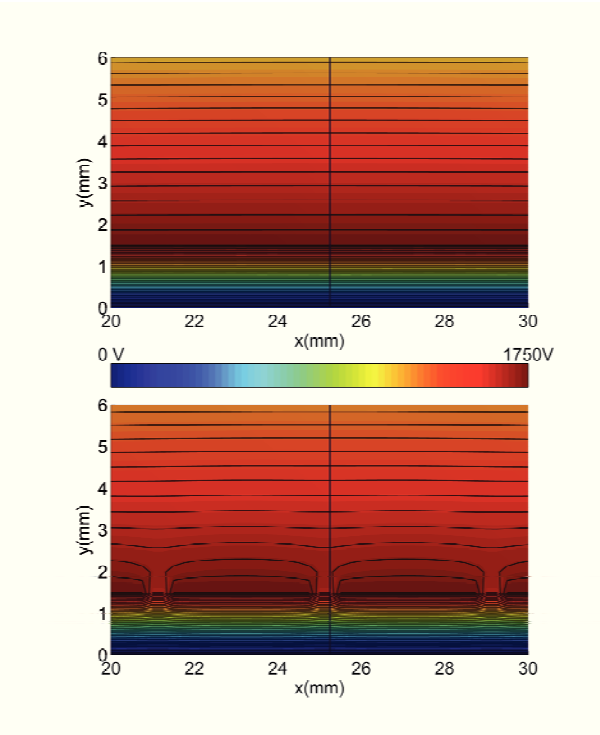

Figure 3.3: *Comparison of the potential calculated by MGS for a non segmented parallel plate detector (top) and a DSSD (bottom) in the region near the electrodes.*

velocity vector using the values of the grid points nearby. Having determined the velocity vector at the interaction point, a new position is computed as the initial position plus the velocity vector multiplied by a time step. This process is repeated iteratively until the carrier reaches an electrode. The sequence of intermediate positions defines the carrier trajectory. Again, interpolation is performed at each new calculated position to determine the velocity vector[1]. By default, interpolation is linear, but the code can easily be changed to include the MATLAB option for polynomial interpolation. However, for large matrices, memory outage can occur with this type of interpolation. A typical time step value is of the order of $1\ ns$, which for drift velocities of the order of $10^7\ cm/s$ (saturation velocity of carriers in Germanium[12, p. 342]), yields a displacement of about $100\ \mu m$ per time step.

The motion of holes and electrons inside the detector volume induces current on the electrodes. The signal response is obtained through the application of the Shockley-Ramo theorem. The charge induced on an electrode due to a point charge q moving under the effect of the electric field created by the bias

[1]Since the velocity is very close to saturation the error of assuming a constant velocity instead of integrating along each individual piece of trajectory is negligible.

voltage, is given by the following expression:

$$Q(t) = -q \cdot \phi_o(\vec{r}(t))$$

where ϕ_o is called the *weighting potential*, and is defined as the electric potential that would exist at the instantaneous position of q, designed $\vec{r}(t)$, if the electrode of interest was set at unit potential while the rest of electrodes were grounded and all charges removed. Applying the theorem for the whole carrier trajectory yields the induced charge as a function of time. Note that, as for the velocity vector, the weighting potential at each intermediate position of the trajectory is obtained by interpolation from the nearby grid points. As the potential is a cubic function, it varies rapidly in the proximity of the electrode, so attention has to be made to the choice of the grid step to avoid large variations of the weighting potential between two consecutive grid points; or, alternatively, cubic interpolation must be used. The total charge computed by MGS is the sum of the signals due to the drift of the positive and negative carriers towards the opposite electrodes of the detector. Finally, the current pulse is obtained through the derivation of the charge signal:

$$I(t) = \frac{dQ(t)}{dt}$$

In order to compute the response at one contact, Poisson's equation must be re-solved to obtain its weighting potential, and this is in fact the last step of the characterization of the detector. The process is identical to the one described above to solve the actual potential. Note that for highly segmented detectors, the need of computing the weighting potential for every contact may be problematic in terms of memory storage and simulation duration. If the total number of grid points is large, solving Poisson's equation may be significantly time-consuming, and the resulting matrices of a considerable size. In order to make the simulation more flexible, MGS allows the user to choose to compute the weighting potential only for certain segments. This may be useful if only the response of a limited region of the detector is of interest.

3.2 Validation of the weighting potentials calculated by MGS

Alternatively to the numerical solution of Poisson's equation, weighting potentials can be calculated analytically under certain assumptions. [68] gives an expression to calculate the real potential of a planar detector with segmentation only in one of the electrodes. The potential is calculated in the plane orthogonal to the strips (no variation is considered along the direction of the strips), and supposing a detector of infinite size. The expression is then:

$$\phi(x,y) = a_0\left(\frac{y}{D}\right) + \sum_{n=1}^{\infty} a_n cos\frac{2\pi n}{P}x \cdot \left(\frac{sinh\frac{2\pi n}{P}y}{sinh\frac{2\pi n}{P}D}\right)$$

with

$$a_0 = \frac{1}{P}\int_0^P \phi_D(x)dx, \qquad a_n = \frac{2}{P}\int_0^P \phi_D(x)cos\frac{2\pi n}{P}xdx \tag{3.2}$$

where x and y represent the position coordinates in the directions parallel and perpendicular to the electrodes, respectively. The potential is assumed to be periodic with period P, where P represents the strip pitch, so the formula applies only for $0 < x < P$. D is the detector thickness and $\phi_D(x)$ is the potential on the strip surface ($y = D$). The potential on the opposite electrode is set to 0 ($\phi(x,0) = 0$).

The expression is utilized for calculating the weighting potential for a strip at the center of our detector, assuming a segmentation pitch much larger than the strip width W, i.e, $P >> W$. The function $\phi_D(x)$ was defined as follows:

$$\phi_D(x) = \begin{cases} 1 & \text{if } |x| < W/2, \\ \frac{|x|-W/2}{G} & \text{if } W/2 < |x| < W/2+G, \\ 0 & \text{if } W/2+G < |x| < P/2. \end{cases}$$

where G is the width of the gap between strips. This approximates well the potential distribution considered for the weighting potential calculation, where the strip of interest is set to 1, and the rest of strips to 0. A linear decrease from 1 to 0 has been chosen for the gap, using the approximation proposed in [68] for a similar calculation.

In order to compare the analytical and numerical approaches, a small DSSD[2] is simulated with MGS. The strip and gap widths are the same as those of our prototype, but each electrode is segmented only in 21 strips, instead of 100 for the prototype. Detector thickness is also reduced to 5 mm. Figure 3.4 shows a comparison between the weighting potential along the axis of the central strip, calculated with MGS and using the analytical expression. Agreement between both figures is evident. This suggests that MGS could benefit from the use of the analytical approach in the regions of the detector where the assumptions of infinite size hold, that is in the central parts of the volume. However, the use of numerical methods remains necessary to properly simulate the effects of the borders on the outermost strips.

[2]The reason to use a reduced version of the detector is to shorten the simulation time, which for the real PheniX detector is quite onerous. It is assumed that the comparison using the small detector is sufficient to validate the numerical methods implemented by MGS.

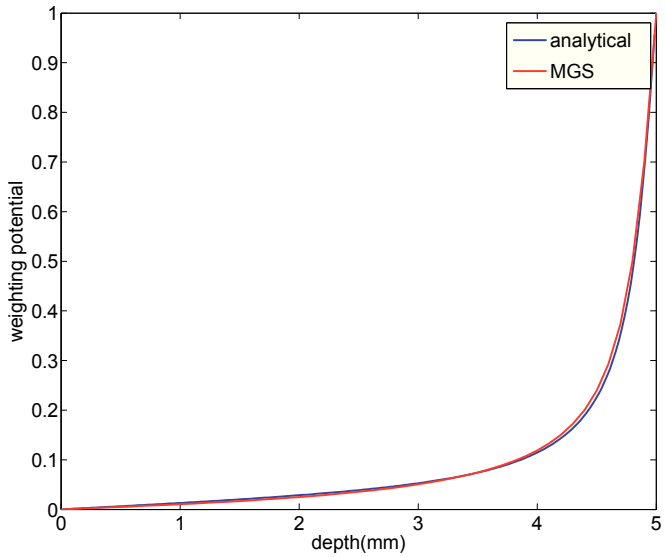

Figure 3.4: *Comparison of the weighting potential obtained with MGS and the one calculated using expression 3.2, for a 5 mm thick DSSD. Each electrode surface is segmented in 21, 350 μm wide strips, with a 50 μm gap between strips. Results are shown for the central strip in its axis along the z dimension.*

3.3 Implications of the step size choice

MGS uses a regular grid throughout all the detector volume, which might make the simulation heavy in terms of computational cost and memory requirements. The choice of an adequate value for the separation between points, or grid step, depends on the detail required to correctly characterize the detector. MGS was originally designed to simulate detectors for nuclear physics applications such as AGATA. Due to its large size, a grid of relative low density suffices to accurately describe this kind of detectors. For instance, [59] reports a grid step of 1 mm. For smaller detectors, smaller step sizes must be used. It is the case, for example, of our DSSD prototype, where the gap between two consecutive strips is $50\ \mu m$. This means that a step size of $50\ \mu m$ is the maximum value that should be considered for MGS to represent the discontinuity of the electrodes. However, using this value still yields a poor representation of the strips edges. The sharp transition from the metallic contact to germanium is modelled in the simulation as covering $50\ \mu m$. This affects the calculation of the response for interactions that occur in the gap between strips. Figures 3.5 and 3.6 represent the weighting potential of a strip in the gap for a small version of our prototype (only 4 strips per side), as calculated by MGS using two different grid steps: $50\ \mu m$ and $10\ \mu m$, respectively. Let us recall that the weighting potential of a strip gets value

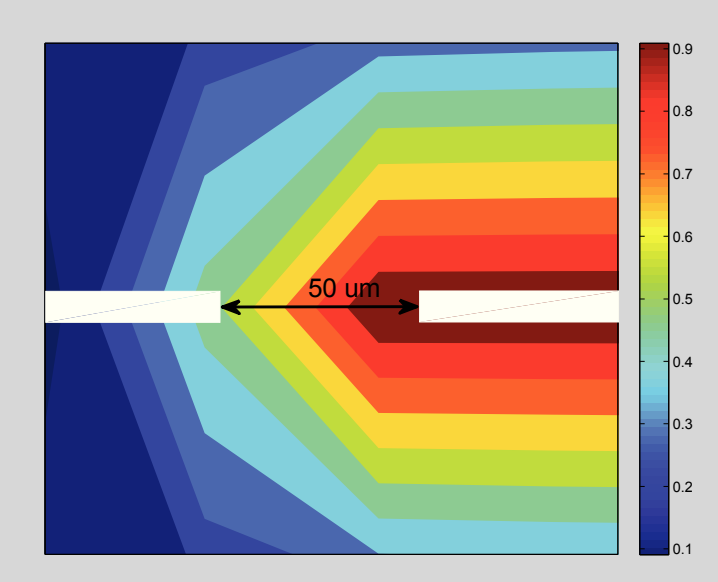

Figure 3.5: *Gap between two strips. The weighting potential of the right-hand strip is represented, calculated using a* $50\ \mu m$ *step size.*

1 on its surface, and 0 on the rest of strip surfaces, so one would expect the transition between these two values to happen along the $50\ \mu m$ gap. We see that this is well approximated with the $10\ \mu m$ step, while for the $50\ \mu m$ step the neighbour strip surface is significantly overlapped by non null weighting potential values, as if the gap was in reality of $100\ \mu m$. This is explained by the fact that, with a $50\ \mu m$ step, the last grid point of a strip and the first of the following are indeed separated by 2 steps of $50\ \mu m$. Seeing that, further reduction of the step size must be considered to properly simulate events within the gap. On the contrary, the $50\ \mu m$ grid step provides an accurate representation of the weighting potentials below the strips. In that region, a step smaller than $50\ \mu m$ is of no interest. This is demonstrated in figures 3.5 and 3.6, where the weighting potentials, calculated with $50\ \mu m$ and $10\ \mu m$ step sizes, appear in perfect agreement below the strip surface.

3.3.1 Possible improvements of the MGS code

Taking into account the dimensions of our detector plus the surrounding space, the total volume to represent is a box of $5 \times 5 \times 1.5\ cm$. With a $50\ \mu m$ step, this implies a matrix of 300 million points. The amount of time (more than a day) needed by the iterative algorithms to solve Poisson's equation has been found non-viable for matrices of this size. In order to mitigate the impact of the step reduction, we modified the MGS code to accept different step sizes in each dimension, passing from a cubic grid to a

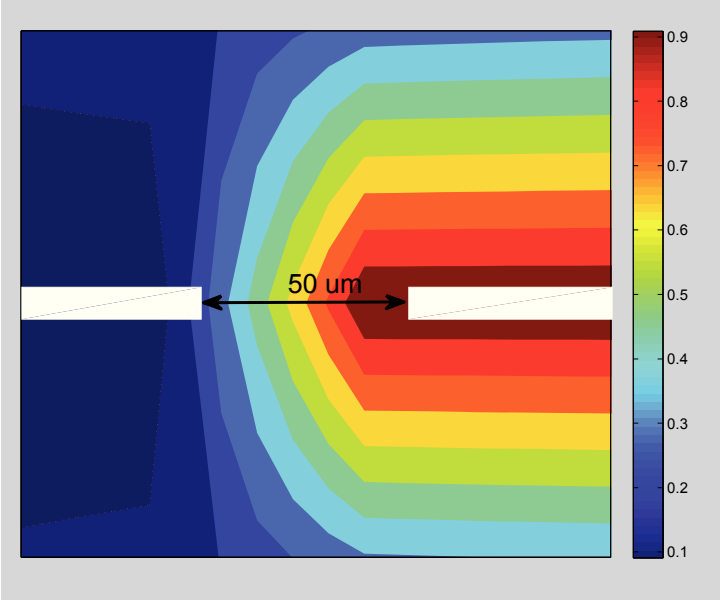

Figure 3.6: .
Gap between two strips. The weighting potential of the right-hand strip is represented, calculated using a 10 μm step size.

rectangular one. This way, the step size for the two dimensions of the detector plane remained at $50\ \mu m$ (for the strip representation), while in the third dimension (orthogonal to the electrodes) a $0.5\ mm$ step size was chosen. In this direction there is no change in the type of material, we have just to represent a linear gradient of impurities in the semiconductor, so a small step is not required. This modification reduced the number of grid points by a factor of 10, to 30 million. The time to solve Poisson's equation is significantly reduced but is still around 5 hours. The total simulation time, comprising the calculation of the weighting potential of the 8 central strips of each side was less than 100 hours.

Further improvements to MGS could be made that would imply more profound modifications of the current code. In the case of DSSD's, the use of analytical expressions to calculate the weighting potential for the inner-most strips of the detector, instead of the numerical solution approach has already been discussed in section 3.1.5. As the weighting potential of each contact is calculated independently from the others, another way of reducing the simulation time would be the parallelization of these computations. The symmetries of certain detector geometries could also be exploited to reduce the volume in which Poisson's equation needs to be solved. For instance, a DSSD presents symmetries along the x, y and z coordinates. By setting the appropriate boundary conditions, the potential would only need to be solved in one of the eight octants of the coordinate system, thus reducing the total

number of points of the matrix by a factor of eight. Finally, a way of greatly enhancing the computation speed would be the implementation of adaptative grids instead of the current rectangular grid of fixed step size. Therefore, a fine mesh could be used to represent in detail the small parts of the detector, such as the electric contacts in segmented detectors, with no need to maintain it in other regions where such a detail is not required.

That said, most of the proposed modifications would probably require rewriting most of the code, which means a great investment in terms of time and workload. At the same time, what today is a very simple tool to use, would become more complex, as it probably would be up to the user to define more in-depth the functioning of the program (e.g. in the case of adaptative grids, the step size and scope of the different grids). The difficulty to add new templates and extend the program to new detector geometries would also be increased.

3.4 Pspice model of the analogue readout chain

The current pulses generated by MGS are fed into a Pspice model of the readout electronics. The general block diagram of the circuit is depicted in figure 3.7. The Pspice model of each stage is presented next.

Charge-sensitive amplifier. The charge-sensitive amplifier (figure 3.8) converts the input current pulse into a voltage signal whose amplitude is proportional to the total charge (area) of the current pulse. As described in 2.2.2, the charge amplifier of the PheniX detection chain is an Amptek A250F. The Pspice modelling of the device was done based on the diagram shown in figure 2.10. We see that the feedback resistance and capacitance, as well as an input FET, are integrated with the amplifier in the same chip. The A250F has been replaced by a generic amplifier because its Pspice model is not publicly available.

Amplifier. A second amplifier after the A250F multiplies the signal by a factor 2. This stage is implemented using the Analog Devices AD8011 chip. The Pspice schematic of the amplifier, used in non-inverting configuration, is shown in figure 3.9.

Offset correction. The purpose of the offset correction block is to remove the continuum component of the signal. The circuit (fig. 3.10) is based on a resistive voltage divider structure that sums the incoming signal with the output of a DAC. The addition is performed after a first amplifier which provides high input impedance to the circuit at the same time that multiplies the signal by a factor 1 or 2 (depending on the position of a switch). The DAC input value is supposed to be the opposite of the

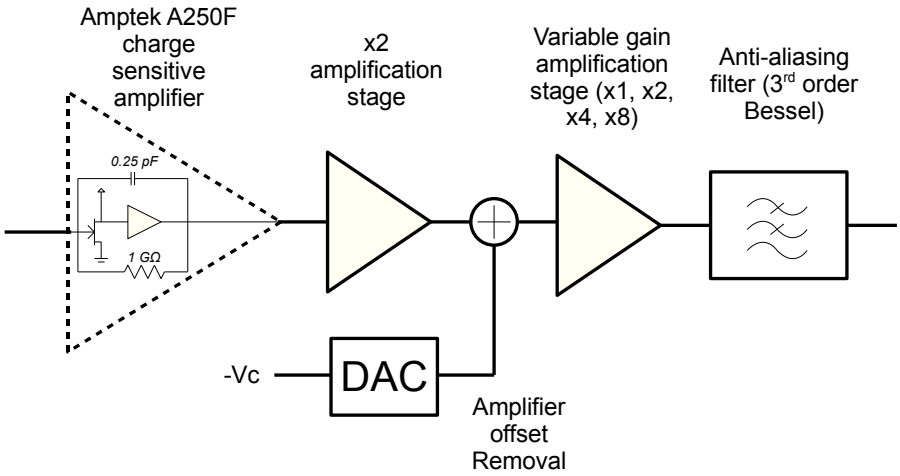

Figure 3.7: *Block diagram of the Pspice model used for the readout of the pulse shapes generated with MGS.*

continuum to be removed. In reality, it is calculated in the digital domain and back fed to the analogue board. After the sum, four additional amplification stages are implemented. The gain of each stage can also be switched between x1 and x2 so that the total additional gain of the offset correction block may vary from x1 to x32, thus providing a means to control the dynamic range of the signal before reaching the ADC input

Low pass filter. The technical documentation of the N6740 CAEN digitizer states that an anti-aliasing filter with cut-off frequency $f_c = 30MHz$ and linear phase response is set as the first stage of the board. Unfortunately, no information is given about the specific implementation of the filter, so in order to fulfil the cut-off frequency and linear phase response requirements, the third order Bessel filter of figure 3.11 was used for the Pspice model. Bessel filters present a flat group delay response along the passband. The transfer function for the chosen configuration is:

$$H(s) = \frac{1}{RLC_1C_2s^3 + LC_2s^2 + (C_1 + C_2)Rs + 1} \tag{3.3}$$

Capacitors and inductor values need to be adjusted to correspond to the generic expression of a 3rd

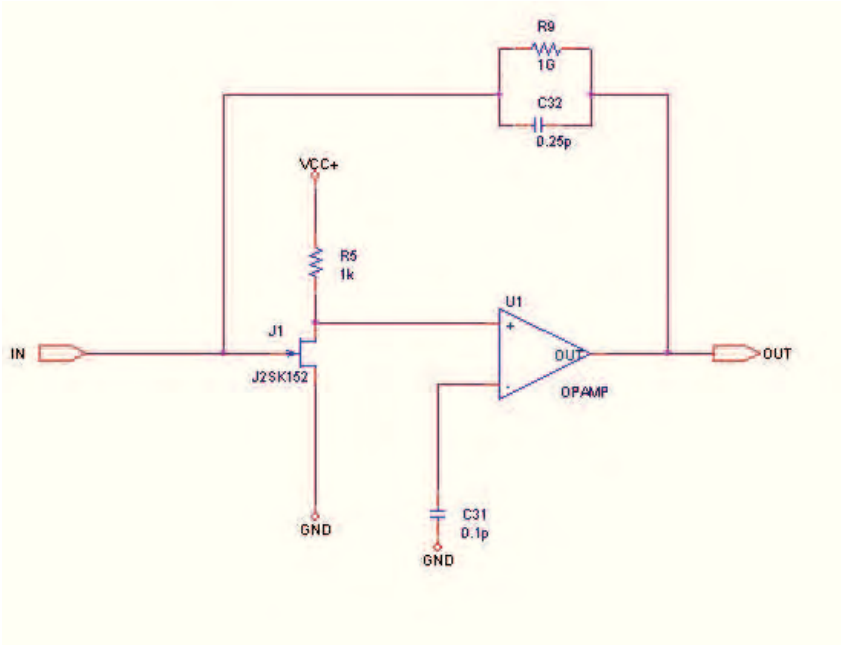

Figure 3.8: *Pspice model of the charge sensitive amplifier*

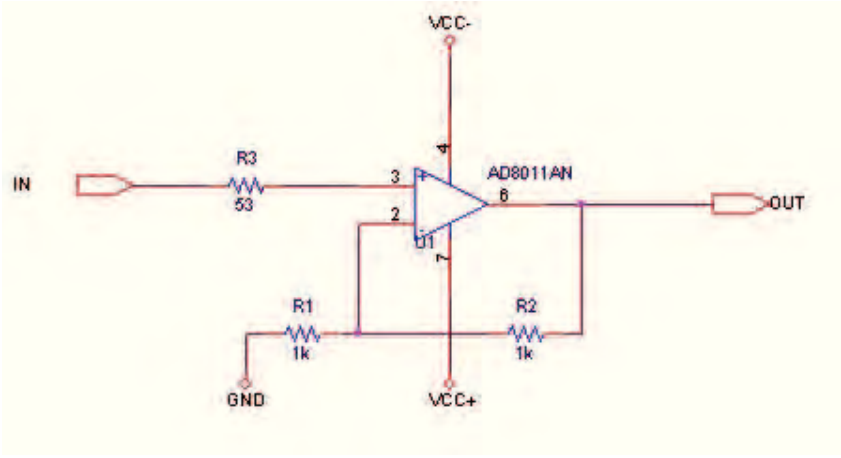

Figure 3.9: *Pspice model of the second amplifier.*

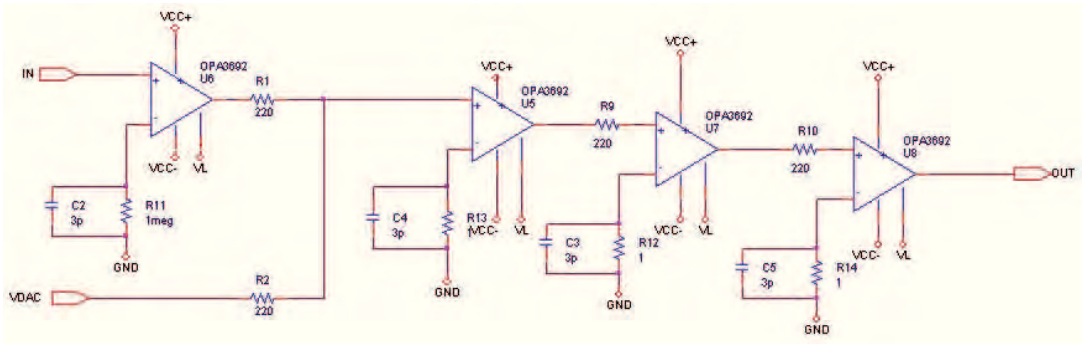

Figure 3.10: *Pspice model of the offset correction block.*

order Bessel filter:

$$H(s) = \frac{15}{(\frac{s}{w_0}^3 + 6\frac{s}{w_0}^2 + 15\frac{s}{w_0} + 15)} \tag{3.4}$$

where w_0 is a frequency that has to be adjusted to obtain the desired cut-off frequency. The relationship between w_0 and w_c is obtained from the filter gain, as follows:

$$|G(w)| = \sqrt{H(s = jw) * H(s = -jw)} = \frac{15}{\sqrt{\frac{w}{w_0}^3 + 6\frac{w}{w_0}^2 + 15\frac{w}{w_0} + 15}}$$

By making $|G(w_c)| = \frac{1}{\sqrt{2}}$, we obtain:

$$w_0 = w_c/1.76 = 17.05MHz$$

Equation 3.5 can be rewritten to:

$$H(s) = \frac{15}{15RLC_1C_2w_0^3\frac{s}{w_0}^3 + 15LC_2w_0^2\frac{s}{w_0}^2 + (C_1 + C_2)Rw_0\frac{s}{w_0} + 1} \tag{3.5}$$

which, attending to equation 3.4, yields the following expressions for the components of the filters:

$$15RLC_1C_2w_0^3 = 115LC_2w_0^2 = 6(C_1 + C_2)Rw_0 = 1$$

Setting $R = 1K\Omega$, we obtain the rest of the component values: $C_1 = 1.55pF$, $C_2 = 7.75pF$,

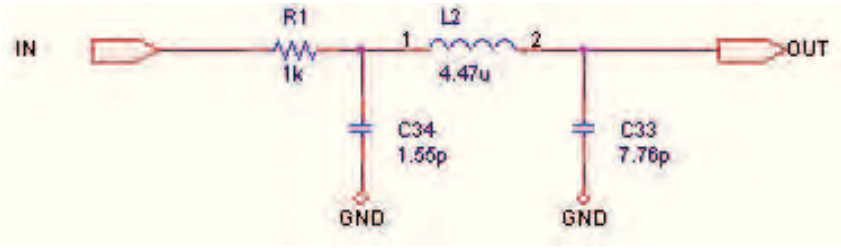

Figure 3.11: *Pspice model of the anti aliasing filter.*

$L = 2.47\Omega H$.

3.5 Comparison of simulated and measured pulse shapes

In order to assess the validity of the pulse shapes obtained with MGS, a simulation of the PheniX prototype is carried out, and the predicted signals are compared to pulses measured in the laboratory. One of the main features of this kind of detector is its ability to locate the depth of the interaction, thus providing a three-dimensional estimation of the position of the interaction. The *matrix algorithm* for the estimation of the interaction position, described in chapter 5, is based on an *a priori* knowledge of the detector response for a number of predefined grid points. This response basis can be obtained through precise scanning of the actual detector, or simulated using tools such as MGS. The spatial resolution of this kind of algorithms directly depends on the density of the basis mesh. For our prototype case, the target is a resolution between 1 and 2 mm in the depth direction. Therefore, measured and simulated pulses were compared for 8 equispaced points along the detector thickness, separated by steps of 1.375 mm. The good matching between simulation and measurements validated MGS as a tool for studying the achievable performances of the intended 3D localization algorithms.

3.5.1 Comparison method

As mentioned above, measured and simulated pulses were compared for each intersection between an anode and a cathode strip, and for 8 different depths of interaction. We denote z the depth of the interaction, and provided that the laboratory prototype is irradiated from the P side, we define $z = 0$ at that electrode. The electrode on the N side is then placed at $z = D$, D being the detector thickness, i.e. $11\ mm$. The comparison is therefore carried out for

$$z_k = \Delta_z/2 + k\Delta_z, \qquad k = 0, \ldots, 7 \tag{3.6}$$

with

$$\Delta_z = D/8 = 1.375mm \tag{3.7}$$

Obtaining the simulated pulse shapes at each z_k is straightforward using MGS, since the program allows to define the exact position(s) of the energy deposition(s). For simplicity, x and y dimensions were kept constant to simulate pulses in the center of the intersection, as lateral displacements within the pixel have no appreciable influence on the pulse shape [3]. The depth of the interaction of measured events, on the contrary, needs to be deduced from the analysis of the pulses. This analysis consists in comparing the *time of arrival* of the measured pulses at both electrodes, defining time of arrival as the instant when the pulse reaches 50% of its peak value.

To deduce the relationship between the interaction depth and the timing measurement, in a first approximation we assume that an energy deposition consists of a pair of positive and negative point-like charges drifting from the deposition point towards the electrodes at constant (saturated) speed: the positive charge or hole drifting towards the P side at speed v_h and the negative charge or electron drifting towards the N side at speed v_e. We assume also that the pulses seen at each electrode rise instantaneously[4] when the respective particles get to them, and that we are able to determine exactly those instants (t_h for the instant of arrival of the hole and t_e for the instant of arrival of the electron). Under these assumptions, and taking $t = 0$ as the instant of deposition, figure 3.12 shows examples of interactions occurring at different depths in the detector and the relationship between the time of arrival of the pulses and their interaction depth. Note that t_e takes its maximum value when $z = 0$, as the electron needs to travel all the detector thickness, D, before reaching to the electrode. We then have:

$$t_{e,max} = \frac{D}{v_e} \tag{3.8}$$

Similarly, t_h is maximum when $z = D$:

$$t_{h,max} = \frac{D}{v_h} \tag{3.9}$$

And at any z between 0 and D:

$$t_e = \frac{D - z}{v_e}, \qquad t_h = \frac{z}{v_h}$$

[3] Energy depositions close to the strip boundary result in charge shared events which are rejected in the DAQ system.

[4] As it is represented in figure 3.12, the weighting potential presents a strong gradient at the proximity of the strip, so the pulse raises very rapidly when the charges approach the electrode.

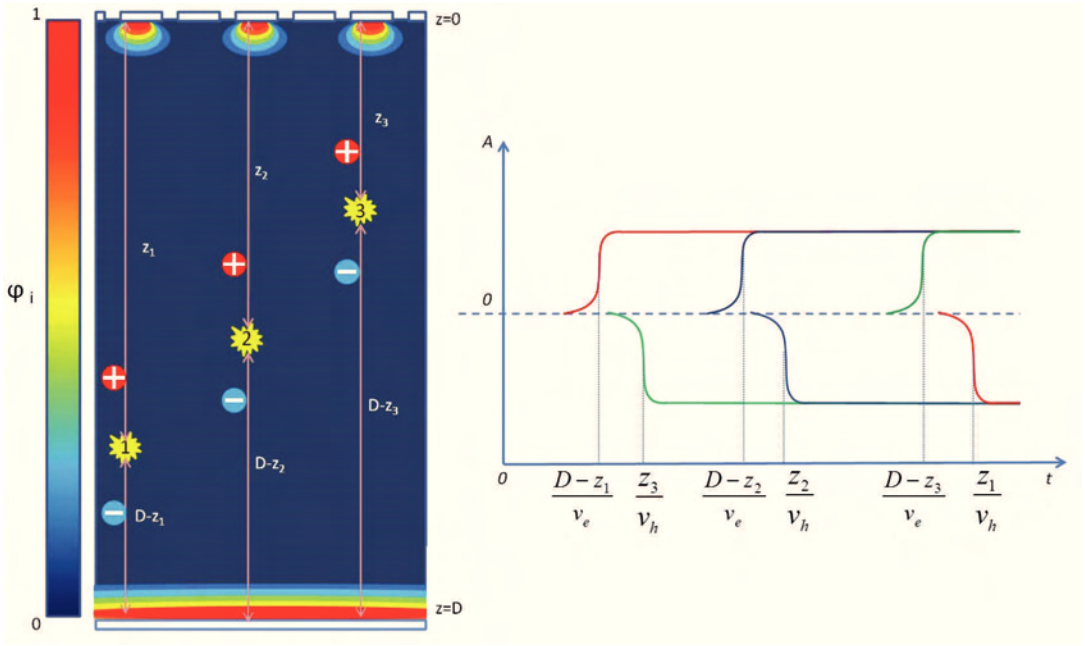

Figure 3.12: *Examples of pulses timing as a function of the interaction depth. On the left, representation of three interactions at different depths, together with the weighting potential of the three collecting strips on the P side (top side in the figure), and the orthogonal strip on the N side (bottom side). On the right, their associated pulses. Positive pulses are measured on the N side, while the negative are measured on the P side. Colour code is as follows: interaction 1 (red), interaction 2 (blue), interaction 3 (green).*

By taking the difference of the last two expressions we obtain:

$$t_h - t_e = \frac{z}{v_h} - \frac{D-z}{v_e} \tag{3.10}$$

We call the term on the left the *difference in time of arrival* (dtoa) between the cathode and anode pulses. That is, $dtoa = t_e - t_h$. Note that from equations 3.8 and 3.9 we have $dtoa_{min} = -t_{e,max}$ and $dtoa_{max} = t_{h,max}$. Combining these with equation 3.10, we are able to express z as a function of $dtoa$:

$$z = \frac{dtoa - dtoa_{min}}{dtoa_{max} - dtoa_{min}} \times D \tag{3.11}$$

Therefore, with the approximations stated above, there is a linear relationship between z and $dtoa$, so we can define a Δ_{dtoa} equivalent to Δ_z (equation 3.7), as:

$$\Delta_{dtoa} = \frac{dtoa_{max} - dtoa_{min}}{8} \tag{3.12}$$

This way, the measured pulses at the depths z_k given by the equation 3.6, are those whose dtoa take the following values:

$$dtoa_k = \Delta_{dtoa}/2 + k\Delta_{dtoa}, \qquad k = 0, \ldots, 7 \tag{3.13}$$

Due to the fact that, in reality, the charge distributions that follow an interaction are not point-like, but form charge clouds of different shapes and sizes, the dtoa measurement can not be considered as the measurement of the exact depth of the interaction, but rather as the measurement of the depth of the charge distribution center. Taking this into account, each MGS pulse at depth z_k was not compared to a single measured pulse, but to an average of pulses whose calculated dtoa is in the range of values $[dtoa_k - \delta, dtoa_k + \delta]$. It was assumed that those pulses were due to interactions close enough to z_k so as their averaged response would be a fair approximation to the response of an interaction occurring at that point. The choice of δ supposes a trade-off: on one hand, the bigger the value, the more pulses will be averaged thus increasing statistics; on the other hand, as δ increases, the averaged signal becomes less representative of the response to a point-like deposit at z_k (as the range of depths that are included in the average also increases). $\delta = 3\ ns$ was finally retained, privileging the fact that responses to be averaged were not too spread in depth around z_k.

3.5.2 The timing measurement

Real measured pulses have a finite rising time, so the *time of arrival* has to be defined. The criterion selected for this work is to define it as the instant when the pulse reaches 50% of its peak value. Note that this is an arbitrary measurement and does not mark the actual time of arrival of the charges to the electrodes. Indeed, the shape of the pulse is determined by the bandwidth of the electronics that do the acquisition.

The timing measurement is based on the *constant fraction discrimination* (CFD) method described in [12, pag. 628]. This technique consists in the addition of the incoming signal (scaled by the fraction value at which the measurement wants to be made, in our case 50%) with an inverted and delayed version of itself. The arrival time is then determined by the zero crossing time of the resulting signal. A linear interpolation has been used in this work to determine this instant with a precision better than our sampling frequency (see 3.13)

The timing measurement error is assessed through simulation. MGS is used for simulating an

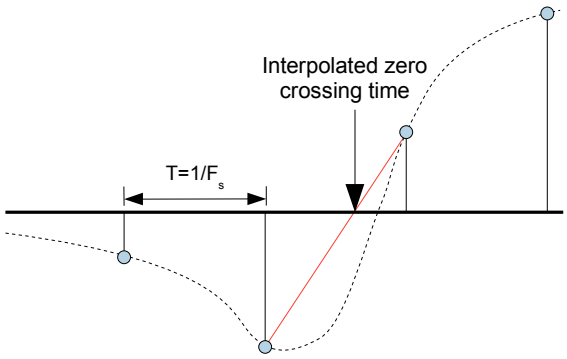

Figure 3.13: *CFD output signal. Linear interpolation is used to estimate the zero crossing time with precision better than the sampling frequency.*

acquisition of events occurring all along the detector thickness and calculating the standard deviation of the *dtoa* measurement as a function of the interaction depth. The event energy is set to 100 keV, and a 1.5 keV FHWM equivalent white Gaussian noise is added to the signal. Noise is added at the output of the Pspice simulation, right before digitization. Under these conditions, $\sigma_{dtoa} < 1\ ns$ is obtained for all z. The same simulation is repeated without linear interpolation of the CFD output, yielding $\sigma_{dtoa} < 8\ ns$. This shows the great benefit of interpolation to improve the precision of the timing measurement. We see also that the timing measurement for energy deposits of 100 keV is not affected by the 1.5 keV noise (typical value of our system).

3.5.3 Acquisition of the pulses

The acquisition of the measured pulses is carried out with the detector exposed to a ^{226}Ra source. The decay scheme of this isotope presents emission of gamma rays at 187.10, 242.00, 295.22, 351.93 and 609.31 keV. These emission lines are energetic enough to ensure that interactions will occur at any depth along the detector thickness. All events whose measured energy is below 100 keV are discarded to avoid degradation of the timing measurements due to a poor signal to noise ratio. 3.14 shows the histogram of measured events as a function of dtoa, obtained under these conditions. The plot includes all energy deposits above 100 keV, as well as double events resulting from Compton interactions (assuming that enough energy is deposited at each interaction). For this reason, its shape does not correspond to the theoretical exponential attenuation curve expected for the combination of energies of the source. However, a decay on the number of counts can still be observed as we move from negative values of

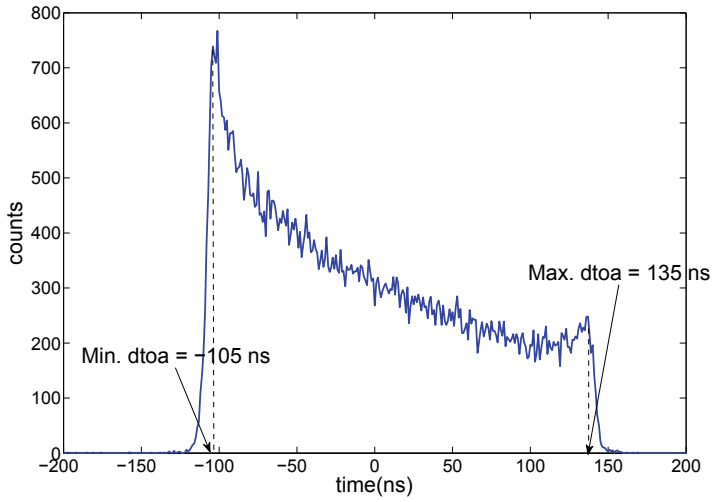

Figure 3.14: dtoa *histogram. Detector is irradiated from the P side (negative values of* dtoa*). As expected, the number of counts decreases as the N side is approached (positive values).*

dtoa to positive values, which is consistent with the fact that the detector is irradiated from the cathode side.

This is used to determine the values of $dtoa_{min} = -110\ ns$ and $dtoa_{max} = 135\ ns$, thus allowing to compute Δ_{dtoa} and $dtoa_k$ from equations 3.12 and 3.13, respectively. Note that dtoa takes slightly higher positive values than negative ones, due to the fact that holes travel at a slower speed compared to electrons. Also, note that some counts can be found at values lower than $dtoa_{min}$ and higher than $dtoa_{max}$. These may correspond to events that occur within the gaps between strips. Those events could first drift to a region close to the gap surface and then drift laterally to the electrodes at slower speed (as the electric field between electrodes is weak), thus yielding higher dtoa values.

3.5.4 Validity of the linear approximation

Equation 3.11 is obtained supposing that the observed pulses rise instantaneously at the moment when charge carriers arrive to the electrodes. It is also supposed that the signal on an electrode is only due to the charge drifting towards it, while in reality some current is also induced by the motion of charges of opposite polarity.

A simulation is carried out using MGS to take into account the effect of finite pulse rise time and the signal induced by the charges of opposite polarity on the dtoa measurement. Figure 3.15 compares the calculated dtoa as a function of depth obtained for the MGS simulation with the values yield by

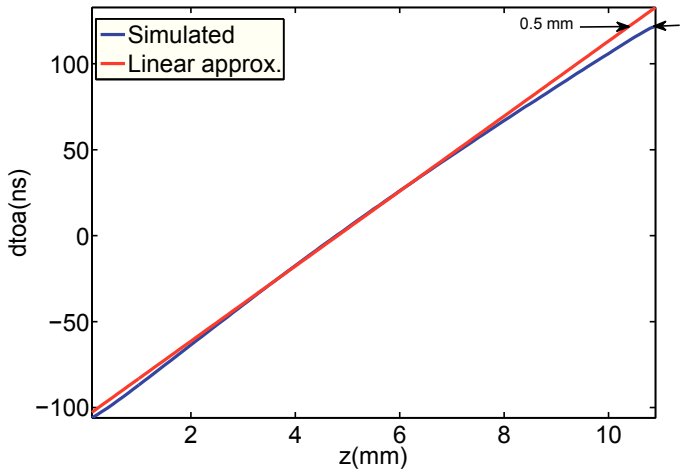

Figure 3.15: *Comparison between the dtoa as a function of the interaction depth obtained through simulation and the values yielded by equation 3.11.*

equation 3.11, taking $dtoa_{min} = -105\ ns$ and $dtoa_{max} = 135\ ns$ (as observed in figure 3.14). We see that the simulation and the linear expression yield very similar results at the center of the detector, while they diverge near the electrodes. This can be explained because for interactions occurring near an electrode, the charge drifting in the opposite direction is sufficiently close at the beginning of its trajectory to induce significant current to the electrode, thus altering the pulse shape. This effect is not taken into account in the linear approximation. In addition, it can be observed that the difference between both curves is more pronounced for near-anode events, where the maximum dtoa value obtained in the simulation (122 ns) is 13 ns less than the measured one. We suspect it to be due to a slight overestimation of the hole drift velocity in the MGS transport model. In light of this , we should expect a discrepancy between the measured and simulated pulse shapes for near anode events. The 13 ns difference corresponds to a maximum error of 0.5 mm in depth positioning (see figure 3.15). In conclusion, the linear approximation appears valid over a large domain of depth.

3.5.5 Results of the comparison between measured and MGS pulse shapes

Figure 3.16 displays measured and simulated pulses for the z_k given by equation 3.6. The signals represent the rising edge of the pulses seen by the strips collecting the charge both at the P side (negative pulse after inverting amplifier) and the N side (positive pulse). Each measured pulse is the average of 1000 events in the range $[dtoa_k - \delta, dtoa_k + \delta]$ (see section 3.5.1). z is the distance of the interaction from the cathode. The evolution of the pulse shape is as expected: for small depths, holes travel a

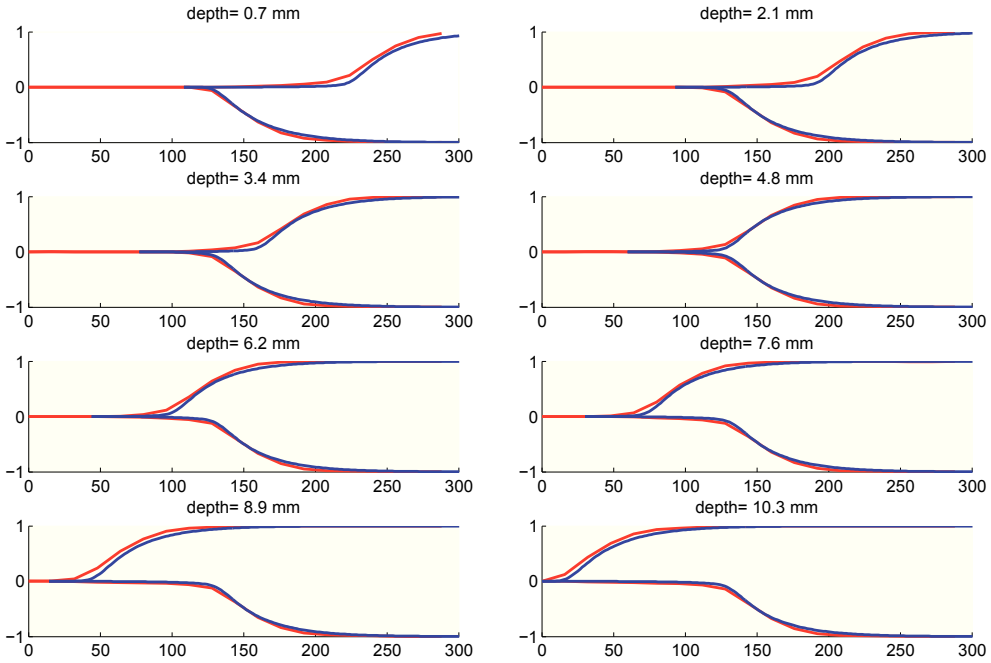

Figure 3.16: *Comparison between simulated (blue) and measured (red) pulse shapes for different depths of interaction. Graphic units: normalized amplitude vs. time (ns).*

short distance before being completely collected in the P side, while the electrons need to cross all the detector volume before reaching the opposite electrode. This translates into negative pulses rising faster than positive ones. As the interaction penetrates deeper into the volume, the opposite effect is observed.

From figure 3.16 we see an excellent agreement between simulations and measurements for all depths of interaction. However, for the events near the electrodes small timing mismatches are observed of the order of 10 ns in the worst case. This reminds the results illustrated in figure 3.15, and discussed in section 3.5.4. They are likely due to the linear approximation used for calculating the depth as a function of dtoa, with probably a slight overestimation of the hole carrier velocity in the MGS code. It is also worth to note that the measured pulse shapes rise slightly faster than the simulated ones, which could indicate some inaccuracy in our Pspice model slowing down the simulated pulses. In figure 3.17 we compare the amplitudes obtained by measurements and simulations. We see that, for all cases, the error is below 10% of the peak value.

Considering the close similarity between the pulse shapes generated with MGS and those obtained through the method of averaging measurements used in this work, we conclude that both methods are

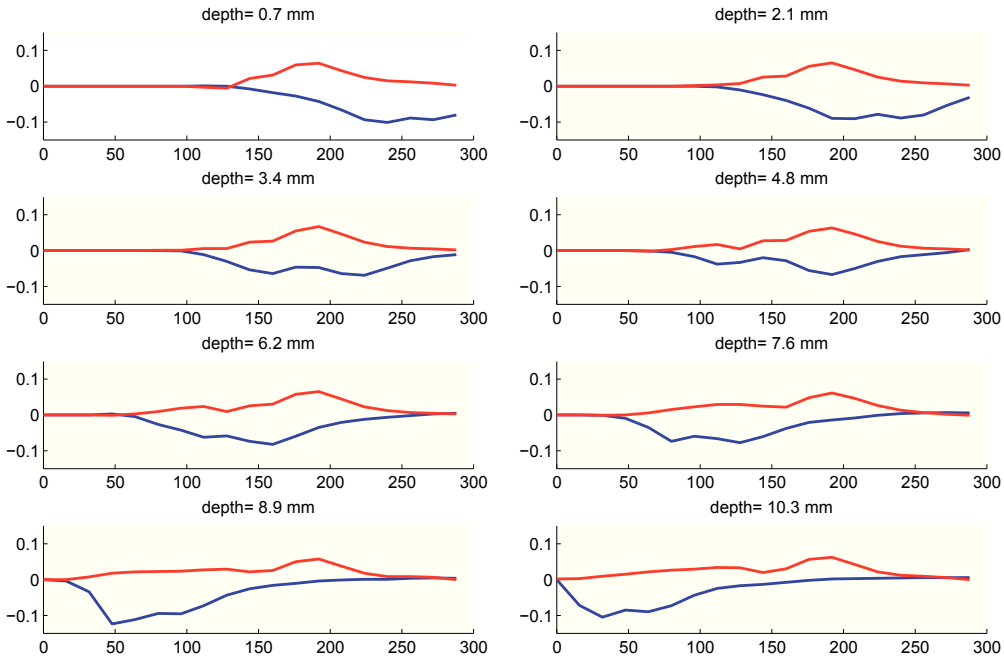

Figure 3.17: *Difference of amplitude between measurements and simulations (simulated minus measured). Red curve corresponds to the cathode and blue curve to the anode. Graphic units: difference of normalized amplitudes vs. time (ns).*

equally valid to generate a library containing the signal response to a basis of grid points, destined to be used by the position estimation algorithms foreseen in our detection system.

3.6 Summary

This chapter has presented the software tools used for the simulation of the PheniX detector signal response. The MGS code has been used to calculate the current pulses induced to each strip when a photon interacts with the detector at a given point in the volume. The accuracy of the simulation has been verified through comparison of the weighting potentials calculated by MGS with those obtained using analytical approximations.

The influence of the grid step size in the MGS approach have also been discussed. Due to the narrowness of the strips, an accurate representation of the electrode segmentation requires a small step size, resulting in very large matrices and thus greatly increasing the computational cost of the simulation.

A lateral step of 50 μm is enough to correctly simulate events below the strip surface. However, the simulation of events in the gap between strips would require a much smaller step, making impractical the simulation. To overcome this limitation, MGS would greatly benefit from a representation of the detector volume through grids of adaptative step size. This way, a small step size could be used to represent with detail the plane of the electrodes, while a bigger step could be used for the Germanium bulk in order to keep a low number of points in the matrix.

The Pspice model used to simulate the readout electronics chain of the system has also been described. The model is composed mainly of a charge-sensitive amplifier and several amplification stages in order to match the dynamic range of the ADC. A low-pass filter is also implemented to emulate the ant-aliasing filter at the ADC input.

Finally, in order to validate the simulation, the pulses calculated by MGS have been compared to real measurements obtained on the PheniX prototype for different depths of interaction. The interaction depth is in almost linear relationship with the time of arrival between the anode and the cathode pulses, as it has been verified in an MGS simulation. Therefore, the interaction depth of the measured pulses have been obtained from the timing of the pulses, which has been measured using a simple CFD. An excellent agreement has been found between the simulation and the measurements, which validates the use of both MGS and the Pspice model as tools to study the performances of the system. The generated pulse shapes can also be used as the basis set of signals needed for the estimation of the interaction position by the *matrix algorithm*, which will be described in chapter 5.

Chapter 4

Energy calculation and detector calibration

This chapter covers the first part of the signal processing in the digital domain, which consists, first, in the calculation of the energy measured by each strip, and then, in the combination of these individual measurements in order to obtain the whole energy deposited by the interaction. Indeed, provided that the detector is a continuous volume with segmented electrodes, the charge carriers generated by the interaction of a photon may be collected by more than one strip of the same electrode. We refer to this phenomenon as *charge sharing* or *charge splitting* in this work.

A description of the different stages of the measurement for a single channel is provided in the first section of the chapter. Following, the effect of charge splitting on the energy measurement is discussed. To do so, the energies measured on consecutive strips when the detector is irradiated with two different sources, ^{241}Am and ^{57}Co, are analysed as a function of the interaction position. Next, a method for the calibration of a DSSD is presented, as well as its practical application for the PheniX prototype. Finally, the spectra measured for those sources after calibration, with their associated energy resolution, are reported.

4.1 Energy calculation on one channel

Energy information is carried by the amplitude of the pulses after integration by the charge-sensitive amplifiers. The direct measurement of the exponential peak gives a poor estimation, due to noise, rounding effect of digitization, etc. Alternatively, pulses are filtered to obtain a shape that facilitates the

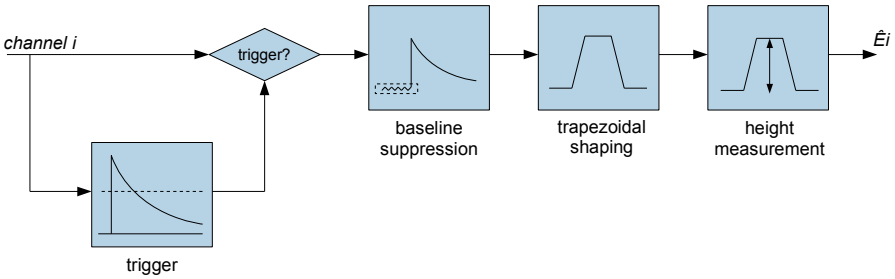

Figure 4.1: *Block diagram of the energy calculation on one strip.*

measurement, while reducing noise at the same time. It has been shown[69] that trapezoidal shaping is optimum for measuring pulses with variable collection times. The trapezoid is a combination of the optimum function in terms of signal to noise ratio performances, which is a finite width cusp, and the optimum function for finite charge collection time, which is a constant for the duration of the charge collection process.

Figure 4.1 shows the block diagram of the energy measurement process on a single electronic channel. The process is identical for all channels. The input signal is the exponential pulse coming from the analogue electronic stage, sampled at a frequency of 62.5 MHz. A digital trigger is used in the first place for detecting the presence of an impulsion in the channel. In case of positive detection, the signal is fed into the trapezoidal shaping filter, with an intermediate baseline removal stage. Finally, the last block is in charge of measuring the trapezoid height for obtaining the energy measurement.

4.1.1 Digital trigger

The trigger algorithm is used as a fast selection of those channels containing an impulsion, prior to the accurate energy calculation provided by the trapezoidal shaping. Due to charge sharing phenomena, the event energy may be distributed among several strips, so some means needs to be provided in order to discriminate which channels are to be taken into account in the measurement and which not. Note that the systematic addition of the energy measured on all channels is impractical, as most of them (corresponding to strips far from the interaction) do not present a significant signal and would only contribute to increase the noise of the measurement. Therefore, the trigger needs to be as sensitive as possible to detect impulsions of low energy, but restrictive enough to reject those channels dominated by noise.

The pulses delivered by the charge amplifier present a rise time approximately equivalent to the charge collection time (around 100 ns), and long decay ($\tau = 250\mu s$). The developed algorithm aims at

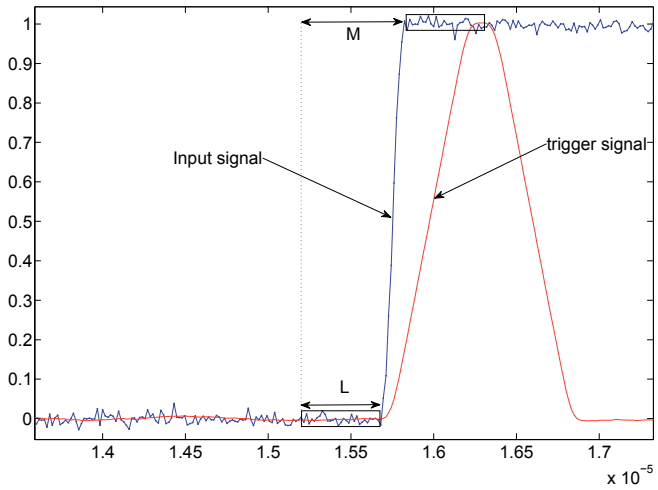

Figure 4.2: *Trigger signal, as calculated by expression 4.1.*

detecting this sudden step in amplitude by calculating the difference between two moving averages of the input signal separated by a certain offset, as:

$$s_{tr}[n] = \frac{1}{L} \sum_{k=n-L+1}^{n} s[k] - \frac{1}{L} \sum_{k=n-L+1}^{n} s[k-M] \tag{4.1}$$

where L is the length of the moving average windows, and M the offset between windows. Note that expression 4.1 is equivalent to a differentiation-integration shaping, with L being the integration constant and M the differentiation constant. The differentiation constant is fixed at a value of 5 samples, i.e. 80 ns, which is approximately the raising time of the pulses (figure 3.16). The integration constant determines the bandwidth of the low pass filtering carried out in the averaging, and it can be increased to relatively high values, as long as it remains small with respect to the decay time constant of the exponential. A good sensitivity to impulsions as low as 5 keV is verified experimentally for $L = 50$ (i.e. 800 ns).

An example plot of the input signal, together with the result of the calculation is shown at figure 4.2. We see that, at the moment when the raising edge falls between the two windows, a pulse appears on s_{tr}. The noise reduction provided by the averaging is evident. Following, s_{tr} signal is compared to a threshold value to decide on the presence of impulsion in the channel.

Equation 4.1 can be seen as a filter in the frequency domain. We obtain its transfer function by calculating the Fourier transform of the response to the impulse:

$$H_{tr}(w) = \sum_{n=-\infty}^{\infty} \left[\frac{1}{L} \sum_{k=n-L+1}^{n} \delta[k] - \frac{1}{L} \sum_{k=n-L+1}^{n} \delta[k-M] \right] e^{-jwn} \tag{4.2}$$

Operating, we obtain a filter gain equal to:

$$|H_{tr}(w)|^2 = 4sin^2\left(\frac{M}{2}w\right) * \left(\frac{sin(\frac{L}{2}w)}{sinw2}\right)^2 \tag{4.3}$$

The last term of the equation corresponds to the low pass filter expression of a moving average of L samples. The first term reflects the effect of the subtraction of the second averaging window, which is mainly the suppression of the continuum component. This way, the filter achieves a double purpose: on one hand, it lowers the noise thanks to the low pass filtering, and removes the baseline of the signal for the threshold comparison that follows.

4.1.2 Pulse shaping

The recursive algorithm presented in [70] is used to implement the trapezoidal shaping filter. The filter output is given by the following expression:

$$s(n) = s(n-1) + p'(n) + d^{k,l}(n)M \tag{4.4}$$

with

$$p'(n) = p'(n-1) + d^{k,l}(n) \tag{4.5}$$

and

$$d^{k,l}(n) = v(n) - v(n-k) - v(n-l) + v(n-k-l) \tag{4.6}$$

where v(n) is the input exponential pulse, M is the decay time constat (in number of samples) of the exponential, and k and l are parameters of the filter defining the length of the raising edge and the trapezoid flat top, respectively. As demonstrated in [69], the flat top width should be greater than the charge collection time, which for the PheniX detector is expected slightly over 100 ns, while the optimum width of the raising edge is determined by the noise profile: increasing the shaping time reduces ballistic deficit and the contribution of series noise (due to fluctuations in the channel current

of the preamplifier FET input stage), but increases the sensitivity to parallell noise (due to fluctuations in the detector leakage current), so an optimum value needs to be found in order to achieve the best possible resolution. The results of simulations performed using simulated signals combined with true noise acquired from the PheniX detector prototype are reported in section 4.2.

4.1.3 Baseline removal

As described in section 2.2.3, PheniX events are stored in blocks of L samples, of which, the first P samples correspond to the pre-trigger. Both L and P are defined by the user. Typically, a channel carrying a pulse also contains a superposed continuum component which can affect the measurement of the pulse amplitude. The effect of this baseline depends on how P and L are chosen with respect to the trapezoid dimensions, as shown in figure 4.3. There we see the output of the trapezoidal filter separately for an input exponential pulse and for a constant value. The effect of the continuum is reflected on the filter output as a trapezoid occupying the start of the record. Note also that a small baseline shift remains after the trapezoid. This effect can be seen as a pileup phenomenon where the beginning of the record acts as a first impulsion. As the amplitude of the baseline shift is smaller than that of the trapezoid, the number of pre-trigger samples, P should be chosen greater than the trapezoid width in order to avoid an overlap of the undesired trapezoid with the pulse of interest. Provided that P is chosen adequately, the following expression (justified in appendix A is obtained for the error in the energy measurement due to a continuum of value C:

$$\epsilon = \frac{3C(2T_r + T_t)(T_r + Tt)}{\tau(2T_r + 3T_t)} \tag{4.7}$$

which, for typical values of the system ($\tau = 250\mu s$, $T_t = 0.2\mu s$ and $T_r = 2.5\mu s$) yields:

$$\epsilon = 0.03C \tag{4.8}$$

This shows that a rough estimation and removal of the signal baseline at the input suffices to practically suppress the error due to the baseline shift. Indeed, even with an error of 1 keV in the baseline estimation, the committed error would only be of 30 eV. The baseline estimation is achieved by simply calculating the average value in a small window of samples immediately preceding the pulse.

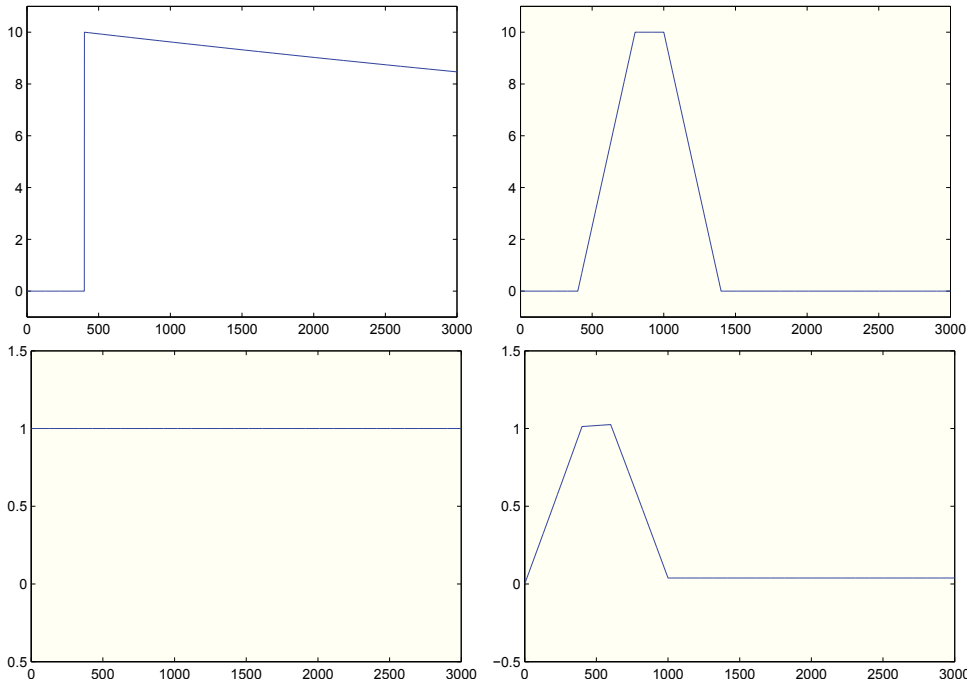

Figure 4.3: *Response of the trapezoidal filter to an exponential pulse(top) and to a continuum component (bottom).*

Impact of a baseline drift on the energy resolution

In the first data acquisitions, a strong parasitic low frequency signal appears on all channels on the P side, as a result of a microphony effect due to vibrations of the vacuum pump that propagate to the high tension board. The interference has a frequency of 660 Hz, which is equivalent to a period of 1.5 ms. This is much longer than the shaping time of the trapezoid filter, which is of the order of a few μs, so, for energy measurement purposes the interference can be seen as a linear drift of the baseline value. The error in the energy estimation due to this interference can then be studied by analysing the response of the trapezoidal filter to an input ramp signal given by:

$$s_i(t) = mt \tag{4.9}$$

The analysis, which is detailed in appendix A, yields the following expression of the error committed in the calculated energy.

$$\epsilon \approx \frac{3m(T_r + T_t)(2T_r + T_t)}{2T_r + 3T_t} \tag{4.10}$$

where T_r is the width of the raising edge of the trapezoid, and T_t is the width of the flat top.

In order to quantify the degradation of the energy measurement due to the interference, the standard deviation of m is calculated for every channel using real data acquired on the prototype. To do so, for each event the digital trigger is used to select those channels where no impulsion is detected, and so only noise and the microphony or ramp signal are present. Then, for a single record, m is calculated as:

$$m = \frac{v_L - v_0}{L} \tag{4.11}$$

where v_0 and v_L are the signal values at the start and at the end of the record (averaged over a number of samples), respectively, and L is the record length. The obtained σ_m are converted to energy units using expression 4.10. The results for two different acquisitions (using ^{241}Am and ^{57}Co sources) are displayed in figure 4.4, where the standard deviation has been multiplied by 2.35 to illustrate the degradation of the resolution in terms of FWHM. Channels 1 to 16 correspond to the P side strips (channel 16 being defective), while channels 17 to 32 correspond to the N side. It can be observed in the figure that the resolution is degraded by approximatively 0.5 keV for all N channels, while on the P side the degradation is higher and largely varies from one channel to another, ranging from the 0.7-0.8 keV of channel 2 to the 2.5-3.9 keV of channel 7. While the worsened resolution on the P side is a direct consequence of the microphony, the source of the degradation observed on the N side is less evident to determine. Three different causes are identified that might contribute to it:

- Vibrations on the P side being mechanically transmitted to the N side, thus inducing microphonic interference also on this side.
- Presence of low energy impulsions which are not detected by the trigger algorithm.
- Inherent error of the m measurement due to the signal electronic noise.

4.1.4 Determining the pulse amplitude

Two methods are proposed for the estimation of the trapezoid height. The first consists in simply calculating the average of the samples belonging to the flat top. In the second, the energy is calculated using a matched filter. That is, a filter whose impulse response is equal to the shape of the trapezoid coming

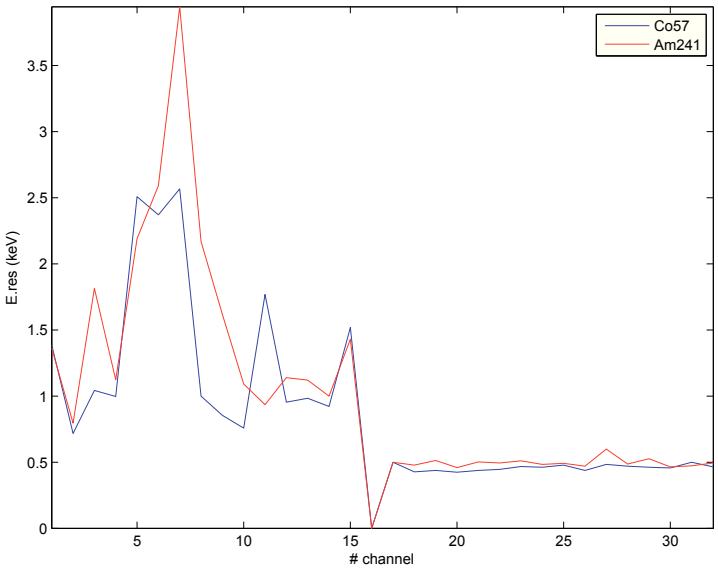

Figure 4.4: *Energy resolution degradation due to the microphonic interference.*

from the pulse shaping stage. The filter acts as a correlation and the energy value is obtained from the amplitude of the correlation peak. Both methods have been utilized in a simulation for determining the optimum trapezoid width, which is described in section 4.2. Compared results yield better energy resolution for the correlation method at equal trapezoid width. The drawback of this approach is that it represents a considerable increase of the computational cost.

4.2 Optimum trapezoid width in PheniX

The optimal duration of the triangular portion of the trapezoid, T_r, in similar noise conditions as those measured in PheniX, is investigated through simulation. MGS pulse shapes are used to simulate an acquisition of 10000 events of fixed energy in the same pixel, for different values of T_r. A 200 ns flat top is chosen to ensure the condition of width longer than the charge collection time. The simulated events are contaminated with real noise records acquired from the prototype, and the energy resolution is measured for every T_r value. The simulations are carried out using noise acquired from the P side and noise from the N side, to study how the microphonics observed on the P side modify the optimum T_r value.

Figure 4.5 shows the calculated resolution as a function of T_r, for four different simulations combining the two noise profiles (P and N side) with the two energy measurement methods explained in 4.1.4. All curves present poor resolution for short T_r values, improve rapidly as T_r increases, reach a minimum value and become to worsen for longer T_r. The variation of the signal to noise ratio does not modify the shape of the obtained curves aside from a scaling of the obtained values. So, the optimum value for T_r is independent of the energy measured.

It can be observed that microphonics penalty long T_r values, so a shorter pulse needs to be used on the P side compared to the N side, to achieve the optimum resolution. Note that, although the best resolution value does not differ much from the one obtained without microphonics, the absolute resolution values presented in the graphics are not representative, as the superposed noise was scaled to a constant total noise power value, meaning that the sum of high frequency noise and microphony in one case has the same power as only the high frequency noise in the other. In reality, the microphonics signal is of much greater amplitude than the noise, resulting in a much worse resolution on the P side, as shown in section 4.1.3. Optimum values of T_r are reached at about 5 μs in absence of microphony, and 2.5 μs with microphony. However they could be shortened to 2.5 μs and 1.5 μs respectively, if needed, without significant loss of resolution.

With regard to the energy measurement methods, the plot shows that better resolution is achieved for the same T_r when the correlation energy measurement method is used in front of the simple average of the flat top samples. This allows a shorter pulse shaping time, which may be important in case of high event count rate, to minimize pileup.

4.3 Influence of charge sharing effects in the energy measurement

As explained in section 2.1.2 (page 30), the finite size of the charge cloud generated in the interaction of a photon with Germanium, as well as the thermal drift of the charge carriers when drifting towards the electrodes, make possible the apparition of charge splitting phenomena. As a consequence, the whole energy deposited by a photon often needs to be determined by adding the individual energy measurements of a few neighbouring strips.

The spectroscopy performance of a DSSD -and in general, of all detectors where the electrodes are segmented in multiple readout channels-, is inevitably affected by charge sharing phenomena. At the very least, for each additional channel that intervenes in the charge collection process, the electronic noise of its readout chain supposes additional degradation of the energy measurement. But, aside from the increased noise, charge sharing affects the performance of the detector in other ways.

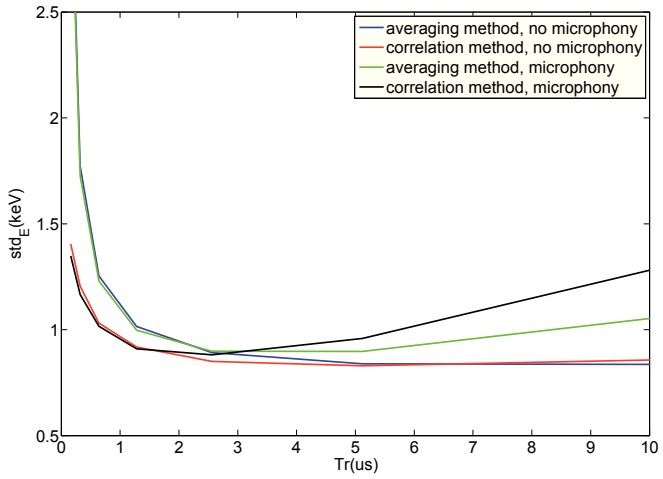

Figure 4.5: *Energy resolution measured for different widths of the trapezoid triangular portion. Values are compared for different noise profiles (with and without microphony), and energy measurement methods.*

As the charge distribution is Gaussian shaped (see figure 2.3), theoretically all the strips on an electrode collect charge, so the energy measurement should take into account the individual contributions of all the strips in an electrode. However, doing so would largely degrade the resolution, as most of the strips lie within the tails of the distribution, with negligible collected charge compared to their electronic noise. To avoid this, the digital trigger is used to select only those channels where a significant amount of charge is detected. As a consequence, the charge collected by the rest of strips is lost. This type of charge loss is more important for wide charge distributions, presenting long tails, than for narrow ones. Therefore, it is more accused for interactions occurring far from the electrodes. The trigger threshold, dependent on the noise performance of the system, also determines the severity of the loss.

A second type of charge loss, which has already been observed in [71] and [72], is to be expected due to charge sharing. Indeed, the fact that all the strips are at the same potential produces a weakening of the lateral electric field in the region between strips and near the gap surface. As a consequence, the charges travelling through those regions may reach the gap surface, and then drift at slower speed towards the electrodes, thus increasing the charge collection time. if this increase is greater than the pulse measurement time, charge loss occurs. Contrary to the loss related to the trigger, the charge loss in the gap is more important when the interaction is close to the electrode and the charge is little spread, because the amount of charge collected through the gap is greater.

The effects of charge loss on data acquired with the detector irradiated by ^{241}Am and ^{57}Co are

presented in the next section.

4.3.1 Effect on the ^{241}Am measurements

The data acquired with the detector exposed to the ^{241}Am source allows a clear observation of the charge loss just described. In figure 4.6, the sum of energies of two consecutive strips is examined as a function of the interaction position, both for P and N sides. The procedure to obtain the graphs is as follows:

1. For each event, a high trigger threshold (5 keV) is used to avoid false detections.
2. The energy is calculated on all triggered channels, and also on their right and left adjacent channels.
3. The channel with the maximum energy deposit is selected, together with the most energetic of its adjacent strips (left and right). Of the two selected channels, E_1 is taken to be the energy of the left channel and E_2 the energy of the right channel.
4. Two vectors are constructed: v_1 containing the ratio $E_2/(E_1+E_2)$ of all events, and v_2 containing the sum of energies $E_1 + E_2$. Hence, v_1 is an indicator of the interaction position between the strips. As the interaction moves from left to right, the energy measured on the right-hand strip increases, and, in consequence, so does the v_1 ratio.
5. v_1 and v_2 are sorted by ascending order of the values in v_1. Thus, the first elements in the vector correspond to events near the left-hand strip, and the last ones to events near the right-hand strip.
6. If the interactions distribution in the volume is uniform and the total number of events is large enough, we can assume that the lateral position of the events in v_1, v_2 also follows a uniform distribution. Thus, the i^{th} event in the vectors is assigned the position $x(i) = i \cdot P/N$, where P is the strip pitch, i.e. 0.4 mm. The graphs are obtained by plotting v_2 versus x.

Charge loss in the gap

Interpretation of the plot corresponding to the P side is as follows: $x = 0$ corresponds to interactions occurring centred with the left-hand strip (strip 1). In this situation, the charge collected by the right-hand strip (strip 2) is the same as the one collected by the strip on the left of strip 1 (strip 0), which is not considered in the measurement . As the interaction shifts towards strip 2, the charge loss through

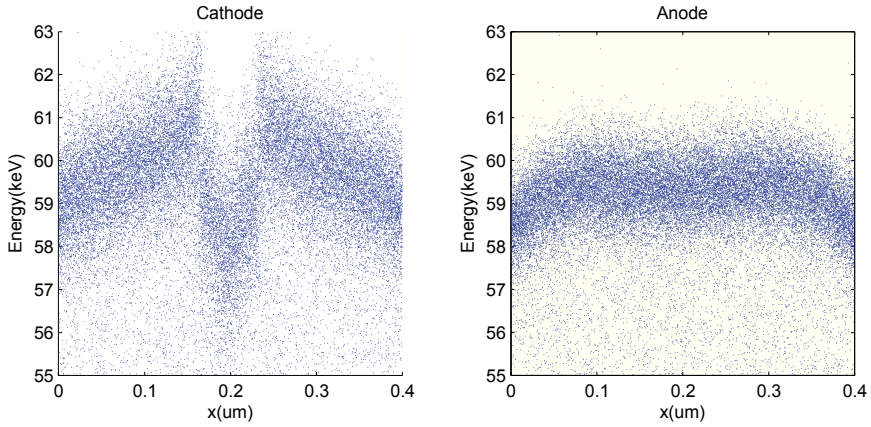

Figure 4.6: *Measured energy on two consecutive strips for P (cathode) and N (anode) sides.* $x = 0$ *corresponds to the centre of strip 1 (left-hand strip), and* $x = 0.4$ *to the centre of strip 2 (right-hand strip).* $E_1 + E_2$ *is plotted versus* x*.*

strip 0 diminishes, thus resulting in a steady increase of the $E_1 + E_2$ measurement. When the lobe of the Gaussian distribution reaches the gap between strips, an abrupt descent of the measured energy is produced due to the charge loss in the gap, which reaches its maximum for $x = 0.2$ (interaction occurring in the gap center). The symmetric behaviour occurs from the gap centre to the centre of strip 2.

If we now compare with the plot of the N side, we see the same type of behaviour near the strip centre, where the measured energy also increases as the interaction moves towards the gap. However, the increase ends earlier than in the P side, and the energy seems to decrease slightly from that point. Unlike the P side case, no abrupt charge loss is observed. This indicates that the charge distribution is much more spread on the N side compared to the P side. This could explained partially by the effect of diffusion[1], but the difference in charge spread between both electrodes seems too important for diffusion to be the only cause. Other effects could also be present such as defects of the crystal near the N side due to which the detector would not be perfectly depleted. This can not be verified with the current experimental setup, but will be verified in future experiments where the diode will be reversed for inspection of the opposite electrode.

[1]As most of the interactions at 59.5 keV occur near the P side, diffusion produces an important charge spread on the opposite electrode (because the charge carriers need to travel all the detector thickness). Therefore, less charge is lost in the gap, but it affects a more important fraction of the events

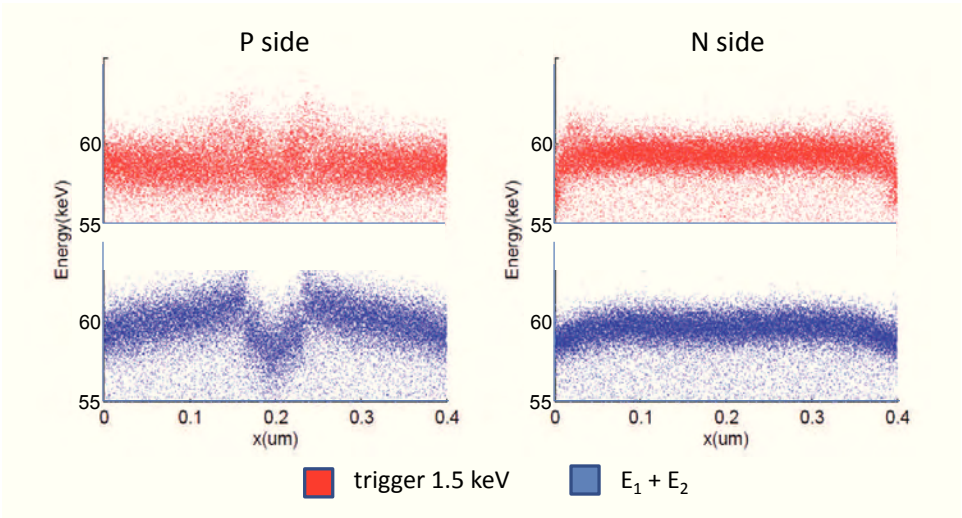

Figure 4.7: *Measured energy on two consecutive strips (blue), compared to the energy event when using a trigger threshold of 1.5 keV on all channels (red). Detector is irradiated with a ^{241}Am source.*

Charge loss due to trigger

The effect of the trigger is reflected on figure 4.7. There, the sum energy of two consecutive strips, obtained using the method described above, is compared with the event energy obtained when a 1.5 keV threshold is used to select the channels to be considered in the measurement. On the P side we see a diminution of the energy measured for the events outside the gap. This is due to the fact that the charge collected by strip 2 is not enough to be detected by the trigger, thus only the energy on strip 1 is measured. For the events inside the gap, charge sharing is more pronounced, so both channels are triggered and the measured energy is the same in both cases. On the N side both plots are very similar, which denotes that, for most of the events, two strips are triggered. Only near the strip centres we observe some differences, which consist in the presence of a small fraction of events outside the cloud of points. Those events above the cloud are due to the triggering of a third strip, while those below correspond to events where only one strip is triggered.

Charge loss correction

The charge loss due to the trigger sensitivity is determined by the noise level of the readout chain and the temperature of the detector (responsible for diffusion), and thus, there is not much that can be done in the signal processing to mitigate it. If the strips adjacent to that collecting the maximum charge were always included in the measurement, even when no impulsion was detected on them, charge loss would

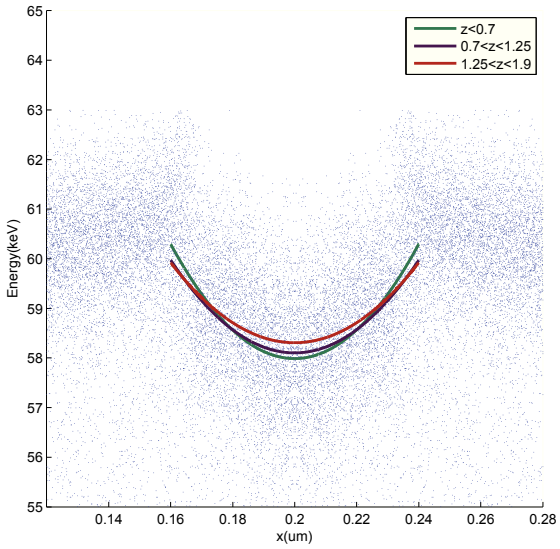

Figure 4.8: *Second order polynomial fits of the ^{241}Am energy distribution in the gap (P side) for interactions at different depths.*

be reduced but at expense of introducing additional noise to the measurements, which in the end would result in poorer performance in terms of energy resolution. To preserve energy resolution at expense of efficiency, a solution would be to reject those events where charge loss is expected to be greater, based on the position of the interaction.

On the contrary, charge loss in the gap may be effectively corrected from the energy measured on the strips. Figure 4.8 shows second order polynomial fits of the energy distribution in the gap, for different depths of interaction. The polynomial coefficients permit to calculate the percentage of charge loss as a function of the position and relate it to the $E_2/(E_1 + E_2)$ ratio (figure 4.9). Thus, upon the processing of a new event, a correction factor can be obtained from the energy on each channel and the interaction depth. Note that, as the charge sharing behaviour depends on the cloud size, these curves should be traced for different energies. A full characterization of the detector, through irradiation using different radioactive sources should allow to determine the correction factors for all energies and interaction depths.

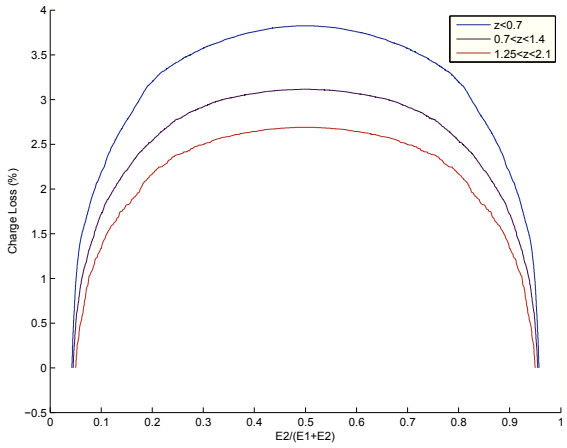

Figure 4.9: *Calculated charge loss for the ^{241}Am energy distribution (P side).*

4.3.2 Effect on the ^{57}Co measurements

Charge sharing is expected to be more accused on the data acquired with the detector exposed to the ^{57}Co source, due to its increased energy with respect to ^{241}Am. For the same reason, the distribution along z should show events penetrating deeper in the detector volume.

Figure 4.10 shows the same type of plot that has already been presented for the ^{241}Am source, where the sum of energies on two consecutive strips is compared to the event energy obtained using a 1.5 keV threshold. Similar distributions as the ones observed for ^{241}Am are observed, with some slight differences. In the P side, the charge loss in the gap affects a larger number of events, due to the increase of the charge cloud size and diffusion, as interactions occur deeper in the volume, and thus, further from the electrodes. As for ^{241}Am, for most of the events (except for those within the gap) the trigger occurs in just 1 strip, thus causing the measured energy to be below $E_1 + E_2$. On the N side, the effect of charge loss in the gap affects a smaller fraction of the events if we compare it with figure 4.9, which is logical due to the diminution of the diffusion on this side (as interactions occur closer). Also like for ^{241}Am, when using the trigger, we notice an increase of the dispersion near the strip centres due to the events triggering one or three strips.

^{57}Co allows to study the charge loss in the gap at higher depth than for ^{241}Am. Figure 4.11 shows the second order polynomial fits of the energy distribution in the gap, measured on the P side, for different depths up to 4 mm, and for the rest of events between 4 and 11 mm. Figure 4.12 displays the equivalent charge loss as a function of the $E_2/(E_1 + E_2)$ ratio. If we compare it with the same plot for ^{241}Am (figure 4.9), a diminution of the charge loss percentage is observed at equivalent depths. This

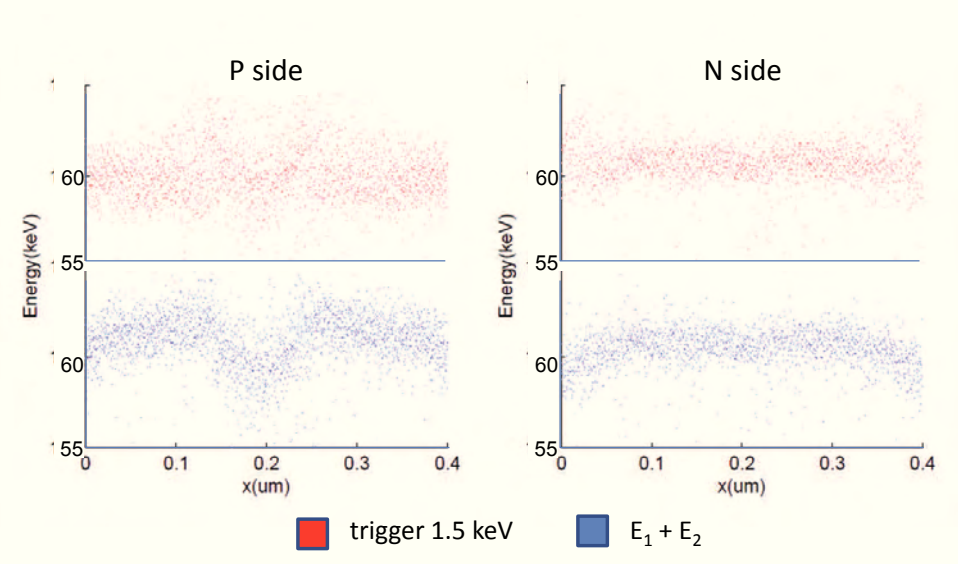

Figure 4.10: *Measured energy on two consecutive strips (blue), compared to the event energy when using a trigger threshold of 1.5 keV on all channels (red). Detector is irradiated with a ^{57}Co source.*

is likely due to the larger charge cloud in the case of ^{57}Co, which causes more charge spread on the electrodes, resulting in less charge being collected through the gap.

4.4 Detector calibration

An essential requirement for the correct determination of the photon energy is that the gain of all channels must be properly calibrated. A radioactive source may be used to adjust the gain of each channel so that the measured energy matches the nominal energy of the source.

If the charge carriers produced by each interaction were always entirely collected by a single strip, calibration could be carried out separately for every channel. In practice, however, charge sharing between strips causes the energy spectrum measured on a single strip to differ from the real emission of the source. As an example, the effect of charge sharing is illustrated in figure 4.13. There, we see plots of the spectra calculated for different channels with the detector irradiated with ^{241}Am, prior to the calibration. Left column shows the spectra of three different P side strips, where the main emission line of ^{241}Am can be observed. Note that, from the fact that no calibration has been performed, the line is centred on different energies from one channel to another, due to the differences in gain for each analogue readout channel. The continuum that appears below the main line is mainly due to charge sharing between strips. On the right column, three N side channels are plotted. As discussed in

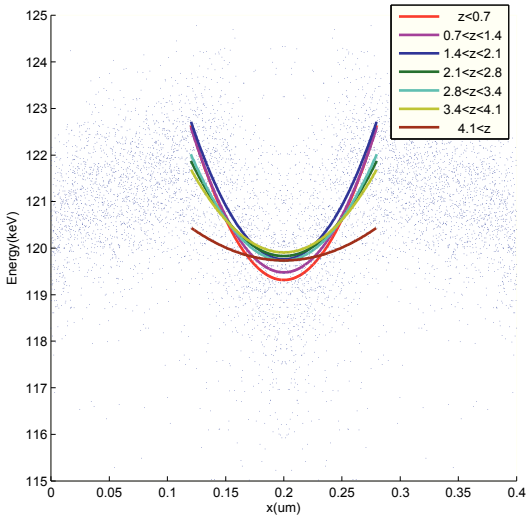

Figure 4.11: *Second order polynomial fits of the ^{57}Co energy distribution in the gap (P side) for interactions at different depths.*

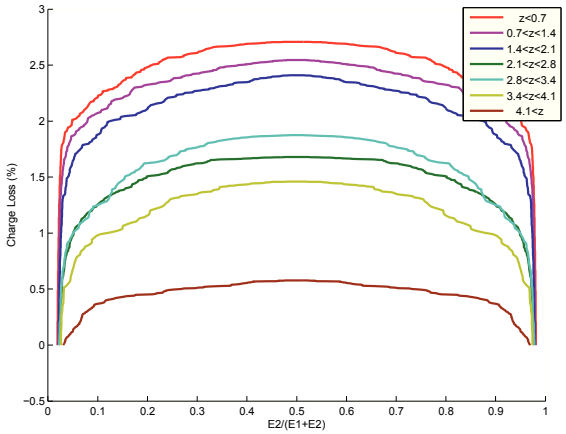

Figure 4.12: *Calculated charge loss for the ^{57}Co energy distribution (P side).*

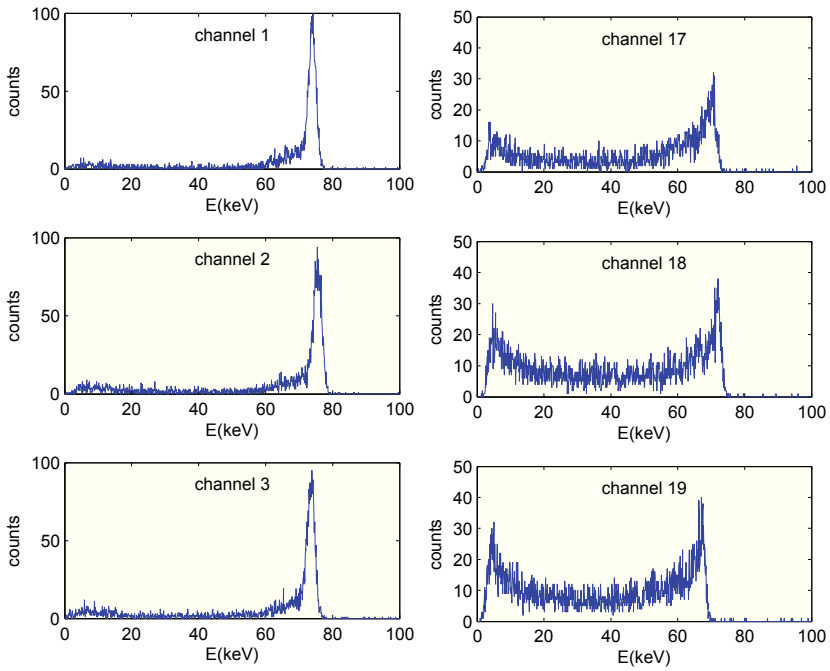

Figure 4.13: *Individual spectra measured on different channels. On the left, channels corresponding to P side strips. On the right, channels corresponding to the N side.*

4.3.1, charge sharing occurs more frequently on the N side than on the P side, up to the point that it is impossible to distinguish the main emission line of the source. This way, it is not the energy measured at each channel that must match the energy of the source, but the total energy considering the sum of all strip energies of the same electrode. To calibrate all channels simultaneously, a *least mean square error* (LMSE) algorithm is implemented to adjust the gain coefficients.

4.4.1 Calibration method

Considering an acquisition of N events, and the detector irradiated by a source of known energy, E_0, the gain coefficients $g_1, g_2, ..., g_M$ that minimize the error in the energy estimation, ε_E, need to be found. ε_E is expressed as:

$$\varepsilon_E = ||\vec{E}_m - E_0||^2 \tag{4.12}$$

where $\vec{E}_m$ is the vector containing the N energy measurements, obtained as the addition of the

energies measured on every channel, multiplied by the g_i coefficients, as

$$\vec{E}_m = g_1\vec{E}_1 + g_2\vec{E}_2 + ... + g_M\vec{E}_M \tag{4.13}$$

Deriving the error with respect to the gain coefficient g_i yields:

$$\frac{\delta\varepsilon_E}{\delta g_i} = 2||\vec{E}_m - E_0||\vec{E}_i \tag{4.14}$$

By making the derivative equal to zero to minimize the error, and setting out the equation for all coefficients, we obtain the following system:

$$\begin{pmatrix} \vec{E}_1\vec{E}_1 & \vec{E}_1\vec{E}_2 & \dots & \vec{E}_1\vec{E}_M \\ \vec{E}_2\vec{E}_1 & \vec{E}_2\vec{E}_2 & \dots & \vec{E}_2\vec{E}_M \\ \vdots & \vdots & \ddots & \vdots \\ \vec{E}_M\vec{E}_1 & \vec{E}_M\vec{E}_2 & \dots & \vec{E}_M\vec{E}_M \end{pmatrix} \begin{pmatrix} g_1 \\ g_2 \\ \vdots \\ g_M \end{pmatrix} = \begin{pmatrix} ||\vec{E}_1|| \\ ||\vec{E}_2|| \\ \vdots \\ ||\vec{E}_M|| \end{pmatrix} E_0 \tag{4.15}$$

which can be solved by inversion of the matrix in the left term to obtain the gain coefficients.

This method is valid considering that all recorded events correspond to photons emitted by the source at the energy of interest, E_0. However, the source will usually emit at other energies which can also be detected by the device, and besides, background events are also collected by the detector. The inclusion of all this events in the estimator induces an error to the obtained gain coefficients.

If the proportion of valid events with respect to background was constant through all the detector volume (and thus, for all channels), there would be no reason for the gain of a channel to be under or overestimated with respect to the rest, so the error on the gain coefficient would be the same for all channels. This error could easily be corrected by tracing the spectra of $\vec{E}_m$, locating the calibration line and re-scaling to center-it on E_0. In practice, however, the detector volume is not irradiated uniformly, so the background proportion differs from one strip to another. This has the effect of introducing different errors on the gain measured for each strip, resulting in a broadening of the spectral line in the $\vec{E}_m$ spectrum.

To correct the inter-channel errors, a second iteration of the calibration algorithm is performed. Through visual inspection of the spectrum obtained after the first calibration, thresholds on the measured energy can be set to select only those events contained in the broadened line on E_0. Depending on the lobe width, the process may be repeated a third time after the second calibration for further background rejection. Figure 4.14 provides a graphical explanation of the method.

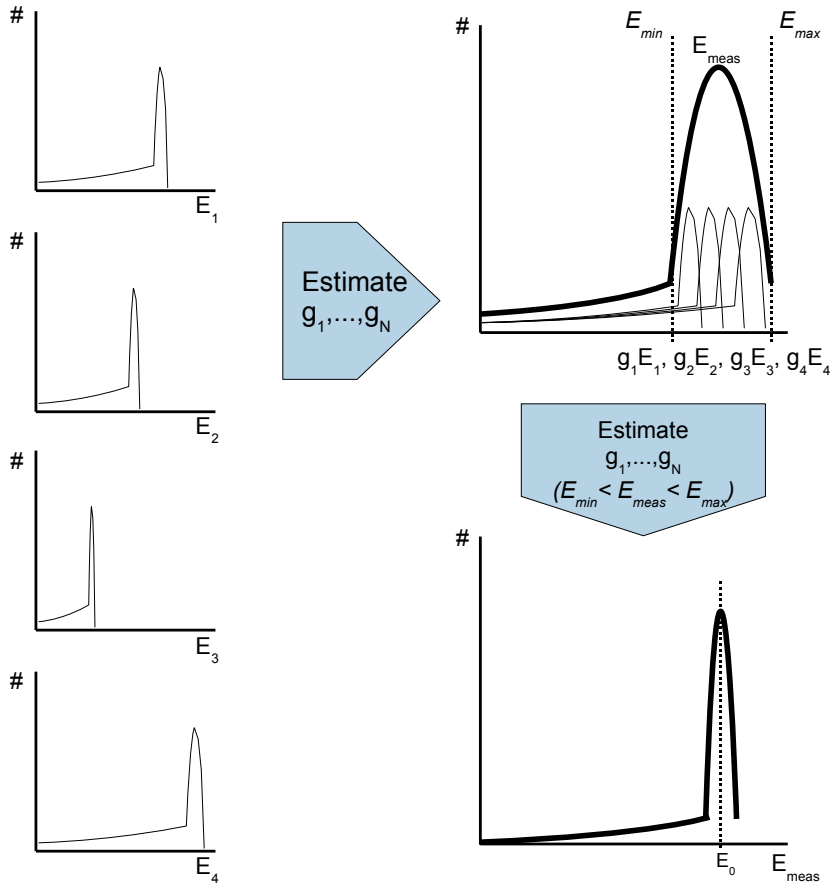

Figure 4.14: *Calibration method. After applying the LMSE estimator for the first time, the sum spectrum presents a broadened lobe. A second iteration of the method, setting up and down energy thresholds, results in a narrower peak. This process can be repeated several times (with further adjustment of the thresholds) until no improvement in resolution is obtained.*

4.4.2 Application of the method

The calibration of the detector is carried out at the main energy lines emitted by the ^{241}Am and ^{57}Co sources.

As it has been shown, with the system current noise level, the loss due to charge not being detected by the trigger algorithm is significant. Depending on the interaction position, figures 4.9 and 4.12 show a loss of the order of 1–2 keV. To minimize this effect, calibration is executed using an “extended trigger”, which consists in forcing the trigger on the strips neighbouring the ones were an impulsion is detected.

This way, each energy measurement is based on the charge collected by at least three consecutive strips. Doing this increases the noise of each individual measurement, but this is not of great importance for the LMSE estimator, provided that a large number of events is considered.

The observation of the data after calibration uncovered an overestimation of the gain coefficient on the outer-most strips. To illustrate it, figure 4.15 shows a plot of the measured energy along the y dimension, after calibration. Coordinate references are those of figure 2.1. We see that the events located near the borders of our useful area of detection present higher energy with respect to the rest, which, as expected, present a flat response. This is caused by the presence of events whose charge collection is shared between the first (or last) investigated strip, and its immediately adjacent which is not read out by our system. This causes a charge loss for a fraction of the events detected on the first and last strip, which tends to be compensated by the LMSE algorithm with an over estimation of their gain coefficients.

The overestimation of a gain coefficient could result in an underestimation of the coefficient in the adjacent channel due to the charge sharing events between them. To avoid this error propagation, an additional calibration step has been added after the estimation of the interaction position by the event solver[2], with the purpose of excluding the conflictive events. To do so all events located within half a strip pitch (i.e. 200 μm) from the borders of our useful area of detection are rejected in this new iteration of the LMSE algorithm.

4.4.3 Measured spectra after calibration

After applying the calibration algorithm on the data recorded with the detector exposed to the ^{241}Am source, the obtained gain coefficients have been used to draw the energy spectra. These spectra have been obtained using the energies calculated by the event solver[2], which for each analysed event returns the following elements:

- Number of interactions.
- Energy of each interaction, as measured on the P and N side.
- x,y,z position of each interaction.

Given that two energy measurements (P and N side) are obtained, two different spectra are traced. Besides, disposing of these two independent energy measurements can be used to enhance the energy resolution. Indeed, if the energy on the P side, E_P, is measured with resolution σ_P, and the energy

[2]The event solver is the object of chapter 5

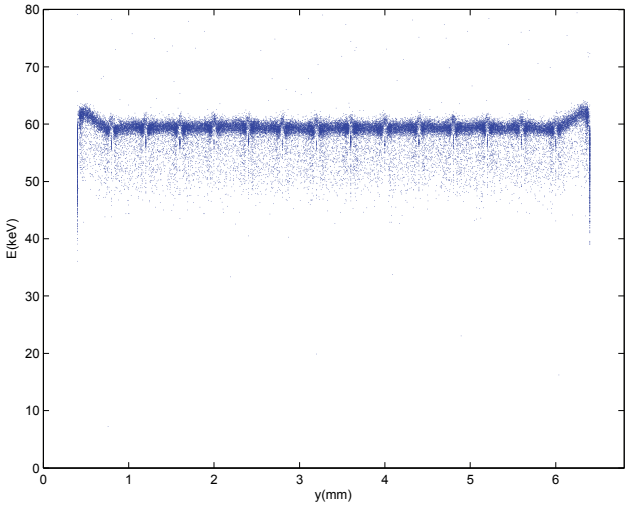

Figure 4.15: *Measured energy (N side) as a function of lateral position. The overestimation of the gain on the two outer-most strips makes necessary an additional calibration iteration where the events on the borders are excluded.*

on the N side, E_N, is measured with resolution σ_N, the combination (average) of both measurements, $E_c = (E_P + E_N)/2$ yields a resolution:

$$\sigma_c = \frac{1}{2} sqrt\sigma_P^2 + \sigma_N^2 \tag{4.16}$$

Therefore, the combined spectrum is also represented together with the spectra on each electrode.

The total energy of multiple interactions could be recovered just by simply adding the individual energy depositions, and thus be considered in the spectra. However, multiple interactions usually involve more channels being triggered, with the consequent increase in noise. Due to the poor noise performance on these first measurements, multiple interactions were rejected for the production of the spectra.

Figure 4.16 presents the spectra for ^{241}Am. Results are obtained from a historic of 58000 events. A trigger threshold of 1.5 keV was used on all channels. Measured resolutions on the 59.5 keV emission line are 1.7 keV FWHM on the N side and 1.9 keV on the P side. The resolution degradation on the cathode is mainly due to the microphonic interference. The combination of both measurements yields a final energy resolution of 1.4 keV.

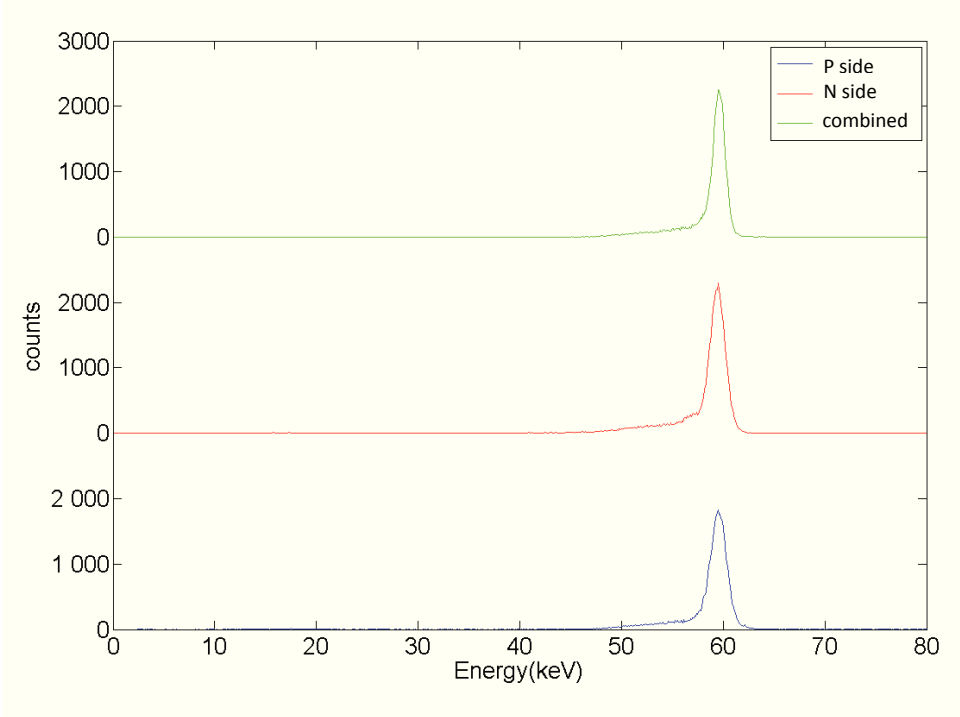

Figure 4.16: *Measured ^{241}Am spectra after calibration.*

Note that a continuum appears for energies above 48keV, which is likely due to second interactions of Compton events whose first interaction occurs outside our useful area of detection. Indeed, the minimum energy of a Compton scattered photon for an incoming energy of 59.5 keV is obtained from equation 2.3, and is equal to 48.6 keV

The detector has also been calibrated at 122 keV, using an acquisition of 9000 ^{57}Co events. The trigger was maintained at 1.5 keV. Resulting spectra are displayed in figure 4.17. Measured resolutions at 122 keV are 2.0 keV on the N side and 2.6 keV on the P side. The combined spectra presents a resolution of 1.7 keV.

4.5 Summary

This chapter has addressed the problem of the energy measurement on a DSSD. First, the signal processing chain used to obtain the measurement on each individual channel has been described. Then, the charge sharing phenomena observed on the data acquired with the PheniX detector, and their influence on the measured energy have been discussed. Finally, a method for the calibration of the detector has

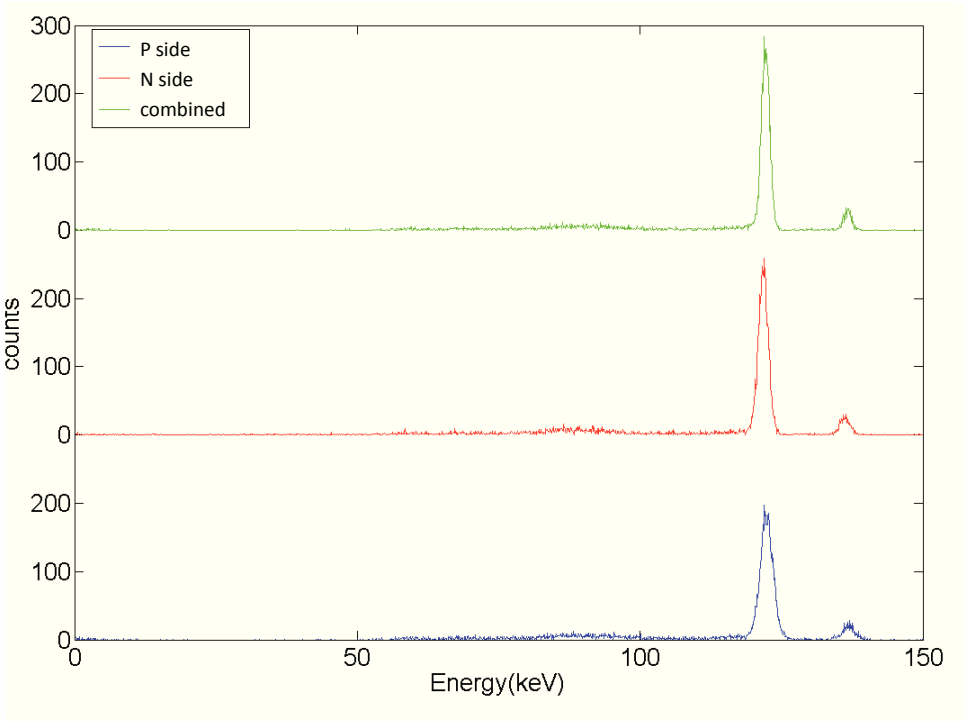

Figure 4.17: *Measured ^{57}Co spectra after calibration.*

been presented, together with the measured spectra and measured energy resolutions using two different radioactive sources.

The measurement of the energy on each channel is based on the trapezoidal shaping of the pulses delivered by the charge-sensitive amplifier. A digital trigger is used to select the channels containing an impulsion, which are then entered on the shaper after removal of the baseline. The measurement of the trapezoid amplitude can be obtained as the average of the sample belonging to its flat top. Alternatively, the amplitude can be obtained through correlation of the signal with a matched filter. Simulations have shown that the use of the matched filter yields better energy resolution at equal integration times, compared to the simple average.

The study of the charge sharing revealed that, for most of the cases, non negligible amounts of charge are collected by more than one strip. Two or even three strips usually present significant charge, although this may be undetected by the trigger giving raise to charge loss. In addition, the interactions that occur within a gap between two strips also present charge loss, linked to the presence of weak lateral fields on those regions. This loss can be corrected based on the ratio of the energies measured on the surrounding strips.

The calibration of the detector must take into account the observed charge sharing phenomena, For this purpose, a method for the joint calibration of all the electrode channels is proposed. The algorithm is based on minimizing the error between the addition of all channel energies and the energy of the source used for irradiating the detector. Using this calibration method, the spectra of two ^{241}Am and ^{57}Co sources are measured, with final resolutions (combining the measurements on P and N sides) of 1.4 kev at 59.5 keV, and 1.7 keV at 122 keV.

Chapter 5

3D location of the interaction

After the calculation of the energy measured on each channel, which was described in the previous chapter, next step consists in determining the energy and position of the interaction (or interactions, in the case of Compton events). To do so, an algorithm capable of estimating the distribution of energy depositions in the volume, from the simultaneous analysis of the waveforms on multiple channels, is required.

The event solver uses the *matrix method* presented by Khaplanov[73]. The algorithm is based in the knowledge of the detector response to a basis grid of interaction points, to which the measured events are compared in order to find the best fit in the least square error sense. A full description of the method is provided here, followed by some examples of application on real data acquired from the PheniX prototype.

The interest of utilising this kind of algorithm instead of simply calculating the position from the energies measured on each strip is twofold: on the one hand, it provides an automatic resolution of the interaction, something which is of particular interest when the energy is collected by multiple strips, for example in the case of Compton events, where we have multiple candidate pixels that need to be evaluated; on the other hand, the algorithm allows to investigate the possibility of improving the spatial resolution by taking into account the phenomena of charge splitting and/or mirror charges, described in section 2.1.2. The algorithm is programmed in a flexible way to include, or not, the strips containing only mirror charges. The final position is calculated taking into account the contributions from multiple basis grid points, thus making possible to obtain a resolution better than the granularity of the grid.

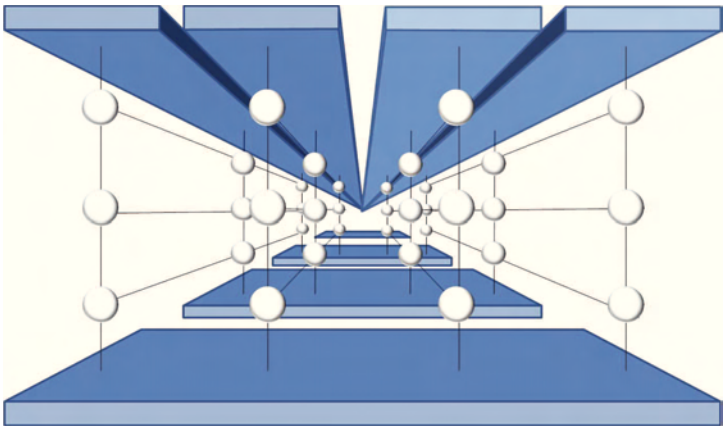

Figure 5.1: *Representation of the basis grid. The signal response to an interaction occurring at any point of the grid is known by the algorithm.*

5.1 The algorithm: the matrix method

The algorithm is based on a sampling of the detector volume using a rectangular grid. Each point of the grid constitutes a candidate position for an energy deposition (figure 5.1). Provided that the signal response induced to the strips is known for each individual basis point, then a matrix M can be constructed, which allows to calculate the signal response to any combination of energy deposits. This is formulated mathematically as:

$$M\vec{x} = \vec{s} \tag{5.1}$$

where $\vec{x}$ is a vector containing the energy deposited on each point of the basis grid, and $\vec{s}$ is called the meta-signal, and is obtained by concatenating the waveforms measured on each strip. i^{th} column of M contains the meta-signal due to an unitary energy deposition on the grid point corresponding to the i^{th} position of $\vec{x}$.

The signal responses at each strip due to interactions occurring at each grid point are called the basis signals and need to be known *a priori*. They can be obtained by simulation, using a software such MGS, or through scan of the detector using a system capable of a precise irradiation of the detector on each grid point.

To calculate the interaction position, the expression 5.1 is inverted. This is, from a known meta-signal, the values in $\vec{x}$ have to be found. Note that, in general, the system of equations that is obtained when developing equation 5.1 can not be solved. Provided that the length of the meta-signal is greater

than the number of grid points (which is typically the case), the system has more equations than unknowns. This implies that some equations on the left of the equality are a linear combination of others. For the system to be solvable, the constant terms on the right of the equality must follow the same linear relationship, which can not be assured as the meta-signal is the product of a measurement. Instead of an exact solution, therefore, a best fit in the least square sense is targeted. This is, the solution for $\vec{x}$ is the one that minimizes the expression:

$$min_{\vec{x}}||\vec{s} - M\vec{x}||^2 \tag{5.2}$$

In addition, a non negative constraint must be taken into account for the values of the elements in $\vec{x}$. Solutions with negative energy deposits do not have a physical sense and must be discarded. To avoid them, a *non negative least squares algorithm* (NNLS), based on the method first described by Lawson and Hanson [74], is used. It consists in iteratively adjusting the values of each element in the vector using only positive values, until some level of tolerance in the error is reached.

Up to here, the basic functioning of the matrix method, as found in the literature, has been described. However, its practical application requires additional considerations. In the next sections, the decisions made for an efficient application of the algorithm to our DSSD case are explained, starting with the need to reduce the amount of data to process by the NNLS algorithm. The time synchronization between the measured waveforms and the basis waveforms is discussed next, followed by the solution of multiple interactions which might lead to ambiguities. Finally, the method used to translate the energy depositions on the basis grid to a few interaction positions and energies is explained.

5.1.1 Data reduction

If we consider the PheniX DSSD, with each electrode segmented in 100 strips (so a total of 200 signal channels), and a granularity of the basis grid at least equal to the intrinsic pixellization of the detector (10000 points multiplied by the number of steps along z, for a 3D grid), we rapidly realize that the amount of data to process by the NNLS to solve one event is unaffordable. Luckily, most of this information is unnecessary to correctly solve the event, so a means needs to be provided to reduce the sizes of x, s and M in equation 5.1. This is done in the three different ways detailed below.

Reduction of the number of segments considered in the meta-signal

The signal induced on the strips far from the interaction(s) point(s) is negligible. Therefore, a digital trigger identical to the one described in section 4.1.1 is used to select the channels to be included in s.

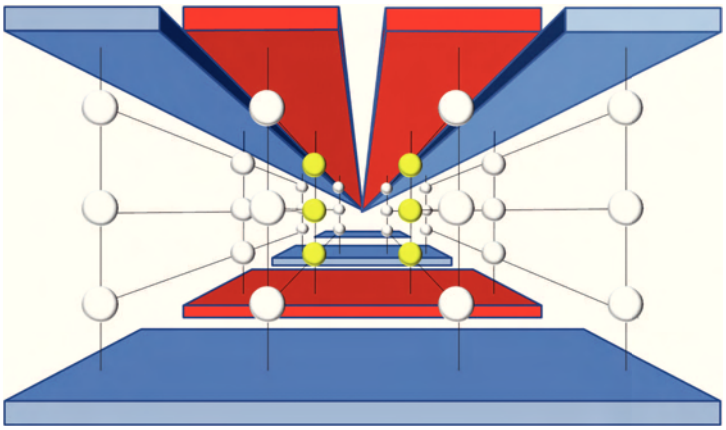

Figure 5.2: *The triggered strips (in red in the figure) is used to discriminate which grid points (in yellow) are candidate to host an energy deposition.*

In addition , if position improvement through the use of mirror charges is aimed, the channels adjacent to the triggered ones must be also be taken into account, as mirror charges are usually unnoticed by the trigger.

Care must be taken for the inclusion of the channels containing the mirror charges in the algorithm. As their amplitude is significantly lower than the main impulsion, it can happen that mirror charges are buried in noise. In this case, their use results in a degradation of the position estimation. This is analysed in section 5.2, where a simulation is carried out in order to assess the spatial resolution gain provided by the mirror charges as a function of the system noise level.

Rejection of improbable grid points

In the same way as the digital trigger helps selecting the channels to be included in s, it is used to select the grid points which are likely to host an energy deposition. The selection of candidate grid points is made by pixels. All the grid points contained in a pixel whose corresponding P and N side strips are triggered are considered, as illustrated in figure 5.2.

Adjustment of the number of samples per segment

The drift of charge carriers from the interaction point to the electrodes determines the shape and timing of the pulse raising edge in the strips that collect charge, and the mirror charges in the non-collecting strips. Therefore, the relevant information concerning the position of the interaction is contained in a small time window. Only the samples in that window are copied to the meta-signals.

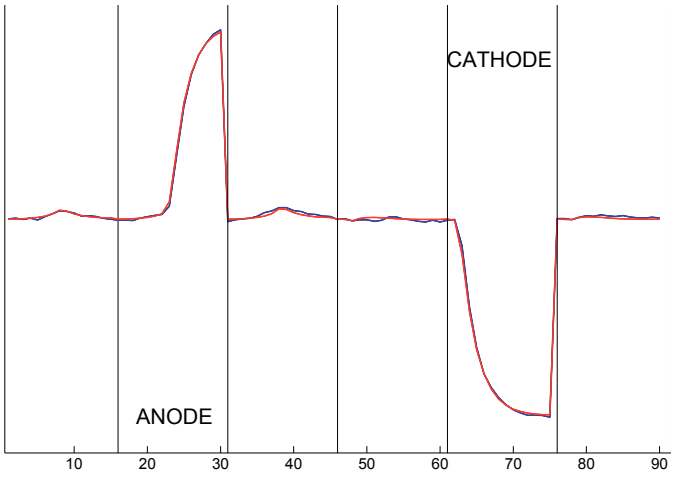

Figure 5.3: *Obtained fit of a meta-signal composed of 6 relevant strips. Blue line represents the meta-signal, and red line the calculated fit. The anode (N side) and cathode (P side) triggering strips are considered in the algorithm as well as their neighbouring strips. Mirror charges can be appreciated on the anode side*

The window lower bound is taken as the instant where the most advanced of all pulses reaches 10% of its peak value. Similarly, the upper bound corresponds to the instant where the most retarded pulse reaches 90 % of its peak value. CFDs are used to calculate the timings. Note that considering samples outside those boundaries, as for example the pulse tails, would only reduce the weight of the significant samples in the fitting algorithm, while at the same time increasing its computational cost.

Figure 5.3 shows a simulation example of a meta-signal, along with the fit calculated by the algorithm. 6 segments are included in the meta signal: a triggering N side channel along its two adjacent channels, and a triggering P side channel also with its neighbouring strips. As explained, only the portion of the pulses corresponding to their raising edges is taken into account. The mirror charges on the non-triggering channels can slightly be appreciated on the N side.

5.1.2 Time synchronization between the meta-signal and the basis signals

For the NNLS algorithm to work, it is needed that the time window used to construct each basis signal is synchronized with the time window of the meta-signal. To achieve this, the channel where the maximum energy has been detected is used as reference. This is, the time window for each basis signal is determined so as the raising edges of the measured and basis signals in that channel are aligned in time.

5.1.3 Solving the position ambiguity of double interaction points

Some precautions must be adopted when using the matrix method in a DSSD, specially in the case of multiple interactions, as the geometry of the detector may induce some ambiguities to the estimation. To illustrate, consider the double event sketched on the left-hand detector in figure 5.4. If both interactions occur at similar depths, all the pulses on the P side will appear at the same time. The same will happen with the pulses on the N side. In this situation, the signals observed by each strip will be very similar to the ones that would be observed if the energy distribution was in reality that of the right-hand detector. There, the less energetic interaction has been decomposed into two depositions occurring at the intersections with the strips that detect the most energetic interaction, producing an estimated waveform that fits well the measurement despite of being completely erroneous.

This false estimations are easy to detect because they are characterized by two very similar energy depositions at a 90° angle with a third deposition. In those cases, the solution consists in simply re-solving the NNLS algorithm after removal of the conflictive grid points from x.

5.1.4 Calculating the final position of the interaction points

After solving the NNLS problem, $\vec{x}$ contains a list of energy depositions associated to a set of basis points. The final step consists in grouping these energy deposits into one or a few interaction positions. Note that in this section a distinction is made between:

- **Depositions:** the result of the estimator for each grid point.
- **Interactions:** which need to be calculated and are the final result of the event solver. An interaction may be formed by a cluster of several depositions and its position is not attached to the grid, but can be anywhere in the detector volume.

Distinguishing interactions that are separated by several strips is straightforward, but multiple interactions may occur at a closer distance, or at different depths within the same strip. In those cases, the decision between one or multiple interactions is less trivial. In this work, the following procedure is proposed to group the grid points in clusters:

1. Energy depositions are evaluated in decreasing order, starting by the most energetic. Depositions under a certain threshold are considered as noise and are discarded.
2. When evaluating a deposition, if its distance from the nearest interaction is lower than the distance between two basis points (Along x, y or z), it is considered that the deposition is a part of that

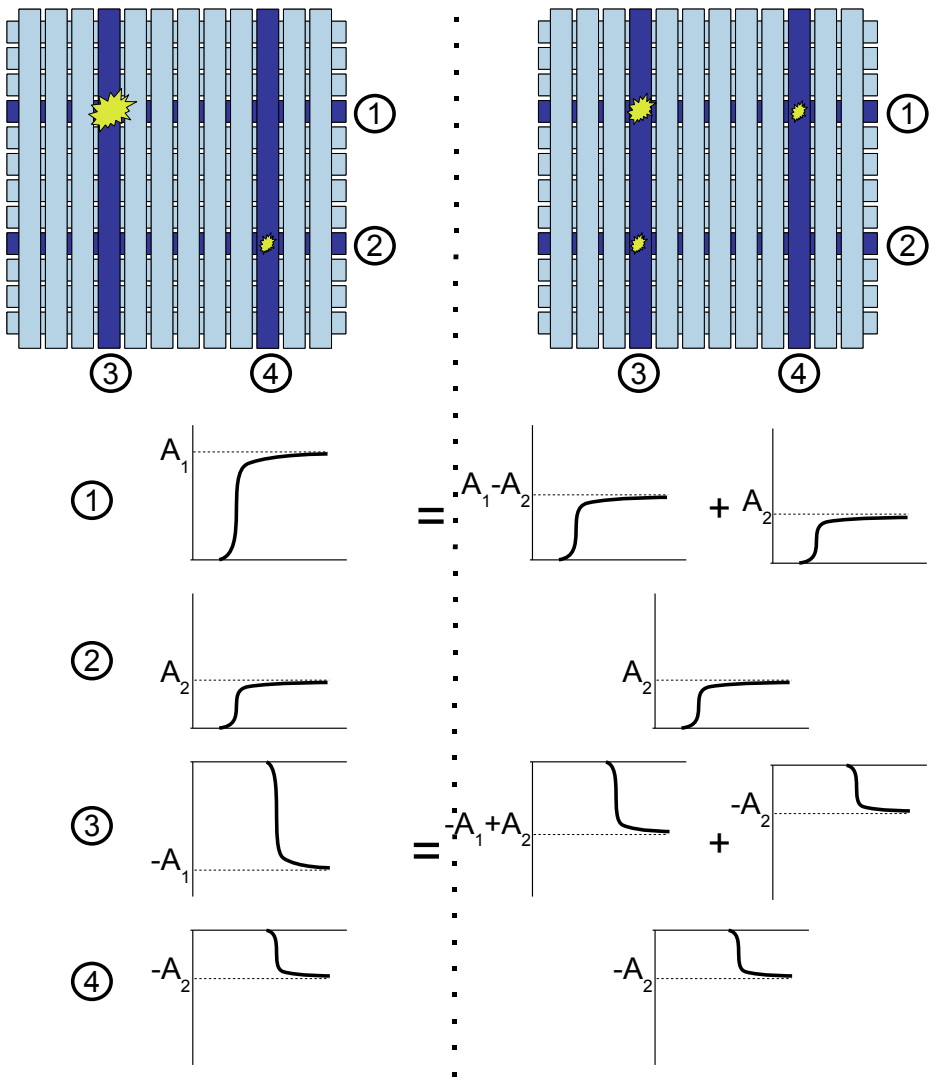

Figure 5.4: *Example of ambiguity when solving a double interaction. The actual event is illustrated on the left-hand detector. On the right-hand, a false event which results in the same signals measured on the strips.*

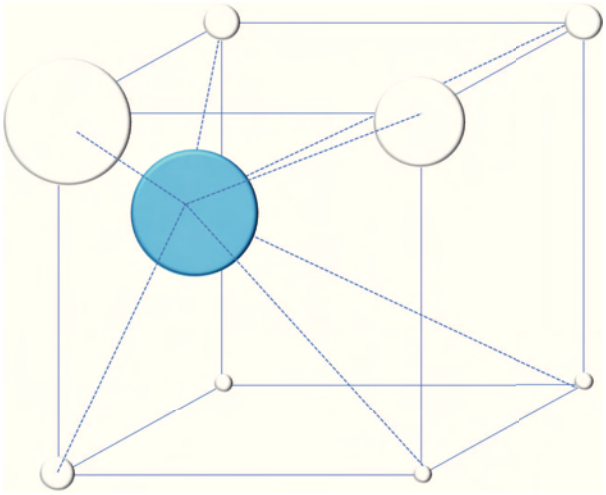

Figure 5.5: *Calculation of the interaction point (in blue) based on the energy and position of all deposits in a cluster (white), using expression 5.3. The size of the spheres is proportional to the energy of each deposit.*

interaction cluster. The interaction position and energy are recalculated to take into account the new deposition in the cluster. If no interaction is found near the deposition (e.g. when evaluating the first deposition), a new interaction is created and its position is assigned as the position of the deposition.

3. The positions of the interactions formed by clusters of more than one energy deposition are calculated as the average position of those depositions weighted by their energy (figure5.5). That is:

$$I(x,y,z) = \frac{E_1 D_1(x,y,z) + E_2 D_2(x,y,z) + ...E_M D_M(x,y,z)}{\sum_{k=1}^{M} E_k} \tag{5.3}$$

Each time a new energy deposition is assigned to a cluster, the interaction is re-calculated using this expression.

4. In the case that an energy deposition is located at less tan two basis position from two or more interactions, its energy is divided and distributed to them proportionally to the distance from the deposition to each interaction.

5.1.5 Calculating the energy of each interaction

As the position estimator is based only on the raising edge of the pulses, the amplitudes calculated for the fitted solution will be less accurate than the energy measurement obtained through the trapezoidal filtering described in the previous chapter. To combine the fine energy measurement obtained using the trapezoid with the 3D positioning, the assignment of energies to each interaction is made by re-scaling the energy depositions in the grid using the energies calculated on each strip.

To carry out the re-scaling, the grid points are grouped according to their nearest strip. The energy deposited on each grid point is recalculated by dividing it by the sum of all valid depositions within that strip, and multiplying by the energy measured on that strip using the trapezoidal filter. The energy of each interaction is then obtained by adding the energy deposited on all grid points belonging to its cluster. Note that re-scaling can be done using the energy measured on the N side or on the P side strips, so two different energy measurements are obtained for each interaction.

5.2 Effect of the mirror charges on the spatial resolution

The improvement on the lateral position estimation that is obtained by considering the mirror charges in the positioning algorithm is analysed through simulation. Lateral errors on randomly generated events are calculated for different energies as a function of the electronic noise. The simulations are repeated for different amplification factors in the analogue stage, to study also the influence of the quantization noise.

Two different sets of simulated signals are generated, using MGS:

- The "basis set" containing the responses for the basis grid. The coordinate system is that of figure 2.1. The basis points are separated in $1mm$ steps along z. In the plane of the electrodes, basis points are spaced by half the strip pitch, that is $200\mu m$ so as to have two rows of basis points within the width of each strip.
- The "events set" is used to simulate the interactions in the detector. A dense scan is performed within a pixel so as to obtain an uniform distribution of events in the volume. The scan is carried out in a square window of $300\mu m$ of side centred with the pixel. This is a little narrower than the strip width so as to avoid having events outside the strips. The scan is performed in $25\mu m$ steps in x and y, and in $1mm$ steps along z.

Having two rows of basis points within each strip causes the response associated to the points closer to the right-hand edge of the strip to present a right-hand mirror charge of higher amplitude than the

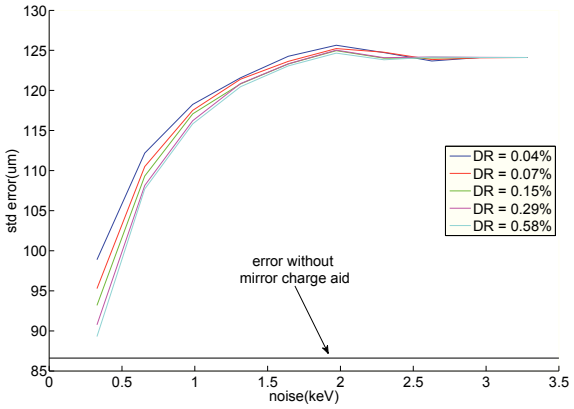

Figure 5.6: *Lateral error measured taking into account the mirror charges for 60 keV events energy. Legend indicates the level of amplification in the electronic stage, expressed as the percentage of the full dynamic range of the ADC occupied by the pulse*

left-hand one. And vice versa for the grid points near the left-hand edge. Hence, the mirror charges of any event within the strip can be obtained by linear combination of the two basis responses. This should entail an improvement of the lateral position estimation provided a sufficient signal to noise ratio. The calculated errors are compared to the error that is obtained with a simple detection, where the lateral position of the interaction is assigned to the center of the strip that collects the charge. This error may be calculated theoretically, for a uniform distribution of events along x, as follows:

$$\sigma_0 = \int_0^{300\mu m} (x - 150\mu m)^2 dx = 86.6\mu m \tag{5.4}$$

Figure 5.6 shows the results obtained for an event energy of 60 keV and a noise varying between 0.3 and 3.2 keV (1 sigma value). The error for each noise value has been obtained from statistics on 10000 simulated pulses. Different curves represent different amplification levels of the analogue stage. We can see that the error diminishes as the signal dynamic range approaches the full input span voltage of the ADC, showing that the mirror charges are affected by the quantization noise. The error obtained without the aid of mirror charges has been plotted as a reference, and we observe that the use of the mirror charges does not improve the measure, even for very low noise levels. On the contrary, it has a degradation effect on the measure which is explained by the addition of additional noise (on the channels containing the mirror charges) to the estimator.

Figure 5.7 shows the results obtained for an event energy of 120 keV. We see that at this energy the use of mirror charges becomes advantageous when the noise is below 1 keV approximatively. Finally,

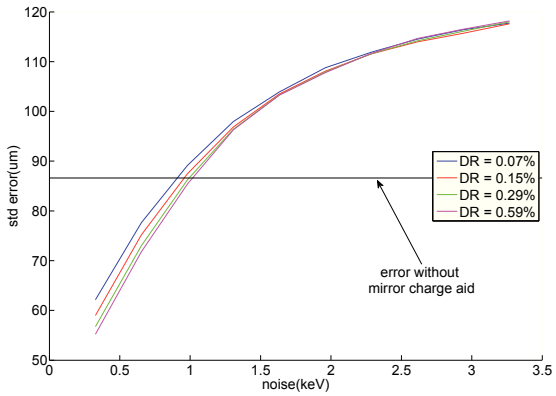

Figure 5.7: *Lateral error measured taking into account the mirror charges for 120 keV events energy. Legend indicates the level of amplification in the electronic stage, expressed as the percentage of the full dynamic range of the ADC occupied by the pulse*

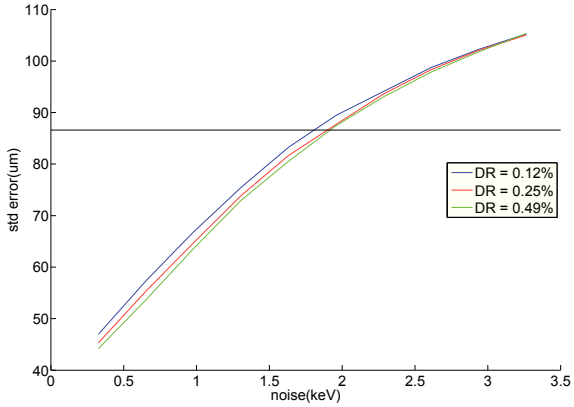

Figure 5.8: *Lateral error measured taking into account the mirror charges for 200 keV events energy. Legend indicates the level of amplification in the electronic stage, expressed as the percentage of the full dynamic range of the ADC occupied by the pulse*

at 200 keV event energy (figure 5.8), mirror charges improve the measure for noise levels below 2 keV approximatively.

This results demonstrate that the use of mirror charges to improve the spatial resolution is not possible at the current status of PheniX, for event energies up to 200 keV, as noise levels of the order of 2 keV (1 sigma) and greater are measured for all channels. However, their use could be foreseen in the future if the noise performance of the system is improved.

5.3 Using charge sharing phenomena to improve the lateral resolution

As seen in section 4.3, charge splitting is largely observed on the data acquired with our prototype. While this effect has a negative impact on the spectroscopic performance of the system, it can be taken advantage of to obtain a spatial resolution better than the strip pitch. Indeed, as it has been discussed is section 4.3, the energies collected by two consecutive strips vary as a function of the interaction position between them.

If we look at the expression used by the matrix algorithm to calculate the interaction position (eq. 5.3), the position along each dimension is obtained as the weighted average of the basis grid position, using the energy depositions on each grid point as the weighting coefficients. Thus, considering a typical case where the basis grid has the same granularity as the detector pixellization (in the detector plane), charge sharing results in two consecutive energy depositions, E_1, E_2, on the basis grid. Taking x_1, x_2 as the x coordinates of the two consecutive grid points, the x coordinate of the interaction point is obtained as:

$$x = \frac{x_1 E_1 + x_2 E_2}{E_1 + E_2} \tag{5.5}$$

as $x_2 = x_1 + P$ (with P equal to the strip pitch), the previous expression is equivalent to

$$x = x_1 + P \frac{E_2}{E_1 + E_2} \tag{5.6}$$

Hence, the position interpolation between x_1 and x_2 is given by the ratio $\frac{E_2}{E_1+E_2}$. However, this supposes that the position varies linearly with the energy measured on E_2. As discussed in section 4.3, the real behaviour is quite different, and depends on the spread of the charge distribution when arriving to the electrodes, which at its turn is conditioned by the energy and depth of the interaction.

If we observe the cloud of positions calculated by the matrix algorithm for an irradiation of the detector by a ^{57}Co source (figure 5.9) through a collimator, the calculated positions are not uniformly

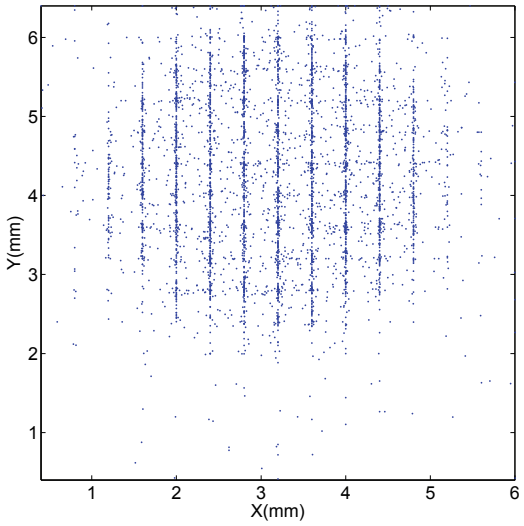

Figure 5.9: *Cloud of positions yield by the matrix algorithm. The detector was irradiated by a ^{57}Co source through a collimator.*

distributed, but appear concentrated around the positions corresponding to the intersections between the N side and P side strips. The effect is especially noticed in the x direction, corresponding to the cathode segmentation, as charge splitting on that electrode occurs less frequently. As a consequence of this, an image obtained calculating the 2D histogram of the cloud of points, using a pixellization greater than the detector segmentation would yield an irregular distribution of counts among the pixels.

In order to be able to increase the pixellization, the distribution of points needs to be corrected, to do so, a fine calibration of the detector response is required to calculate how the lateral position varies as a function of $\frac{E_2}{E_1+E_2}$, and also taking into account the energy and depth of interaction. Such a calibration was not possible in this first set of measurements due to the scarcity of data, but should be performed in the next measurements campaign. However, figure 5.9 shows already that it is possible to gain position information by taking advantage of the charge sharing events.

5.4 Positioning measurements using the PheniX prototype

The first data acquisitions using the PheniX detector have allowed a basic test of the positioning estimator, with results presented below. First, the distribution along z obtained using the algorithm is compared to the distribution obtained using a simple CFD, and to the theoretical absorption of Ger-

manium. Second, the 2D images obtained when placing different masks between the sources and the detector are presented.

5.4.1 Distribution of events along the detector depth

The calculated distributions along z for the ^{241}Am and ^{57}Co acquisitions are compared to the theoretical absorption of Germanium at the corresponding energies.

Figure 5.10 shows the z distribution for ^{241}Am. It has been obtained taking into account all photopeak detections and complete Compton events[1] with energy between 57 and 63 keV. For each event, z was determined from the timing difference between the P side and N side pulses, using equation 11 of the article presented in B. The timing measurements were obtained using a CFD at 50 % of the pulse final amplitude. Superposed to the measured distribution, the theoretical absorption of Germanium at 60 keV is plotted. The curve is calculated using the exponential attenuation law of expression 2.2. The measured and theoretical distributions show almost perfect agreement. This result validates the use of the linear relationship between timing difference and z.

The same plot is displayed for ^{57}Co in figure 5.11. In this case, events between 118 and 126 keV were selected. The variance of the measured distribution is increased with respect to the one obtained for ^{241}Am, as it was obtained with a much shorter acquisition (approximately 4000 events compared to 43000 for ^{241}Am). However, the agreement between the data and the theory can be clearly observed.

In figure 5.12, the depth distribution obtained through direct measurement of the pulses timing has been compared to that calculated using the matrix algorithm. A divergence between both curves is observed for events interacting very close to the cathode surface ($z = 0$). This is due to the fact that the position obtained with the matrix algorithm is a weighted average of the positions of the basis grid, which can never yield a depth lower than that of the first grid point. These measurements are obtained using a basis grid consisting of 16 steps along z, which yields a step size of 0.6875 mm. The first grid point is located at half the step size from the cathode, i.e. 0.35 mm. So, the interactions occurring in the range 0<z<0.35 mm are estimated at z=0.35 mm by the algorithm. This causes the observed increase of the number of counts at this position in the histogram. The overall difference between measurements using the CFD and the estimator is calculated, yielding a standard deviation of 0.25 mm.

[1] Complete Compton events refers to Compton events where both interactions are detected inside the useful area of detection.

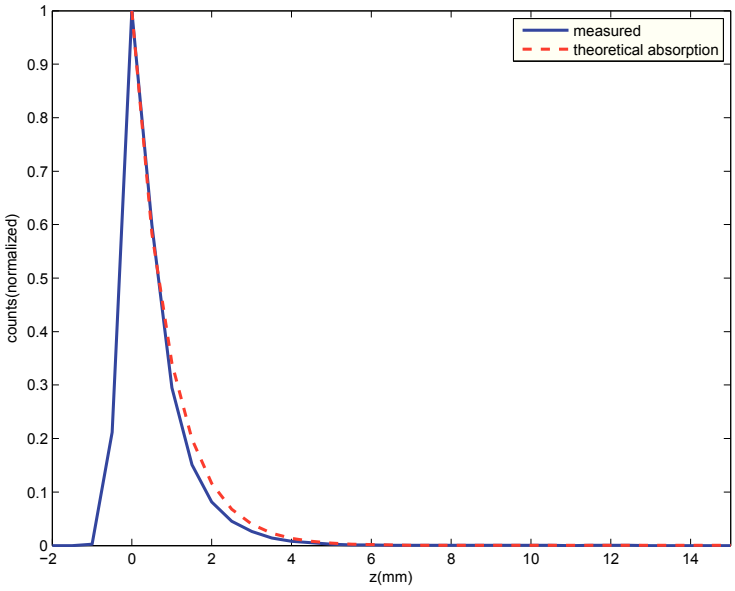

Figure 5.10: *Distribution of events along the detector depth for an irradiation with* ^{241}Am.

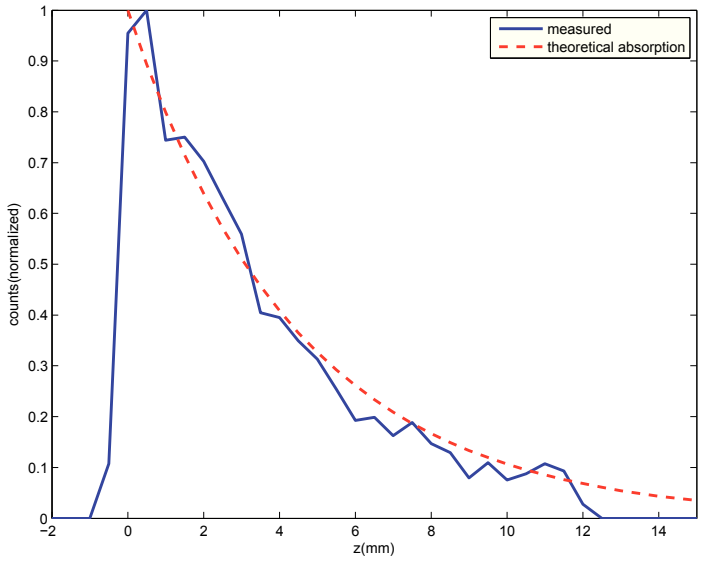

Figure 5.11: *Distribution of events along the detector depth for an irradiation with* ^{57}Co.

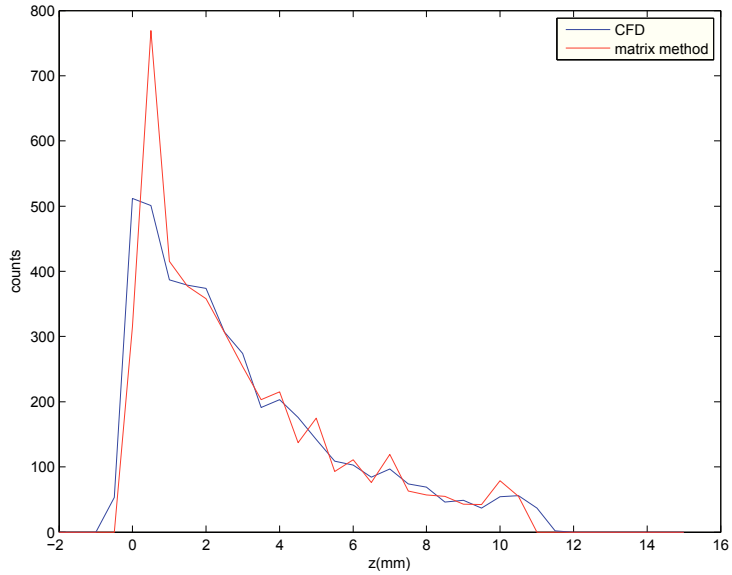

Figure 5.12: *Comparison of the event distribution along the detector depth as measured using a CFD, and as calculated by the matrix method.*

5.4.2 Imaging examples

In order to test the imaging capabilities of the detector, several acquisitions were carried out using different masks to shade parts of the detector. Acquired data was then processed using the matrix algorithm to calculate the interaction position of each event. The 2D histograms of all X-Y positions for each acquisition are presented here.

Due to the high noise, no gain of spatial resolution could be obtained through signal processing. As it has been shown in the simulations, the exploitation of the mirror charges would require much better noise performance than what is measured in our system. The alternative to the use of mirror charges would be to take advantage of charge sharing phenomena. However, the trigger sensitivity (also determined by noise) does not allow sufficient detection of such events on the N side to introduce an intermediate pixel. As a result of all this, for these first test we content ourselves with tracing images at the pixel resolution determined by the strip segmentation, i.e. 0.4 mm. We thus have 15 x 16 pixel images (as one strip was defective on the P side).

The results presented below correspond to the irradiation of the detector in thee situations: first, without any mask between the source and the sensor; second, with a 2 mm round collimator placed

against the Beryllium window of the detector, and third, with a metallic rectangular piece oriented approximately 45° with respect to the strips.

Direct (no mask) irradiation of the detector

Figure 5.13 shows the image obtained with the detector irradiated by the ^{241}Am source, without any shading of the diode. The source was separated 15 mm from the detector to obtain a more uniform distribution of events. Only the events with calculated energy between 57 and 63 keV were considered in the histogram

We see, indeed, a fairly regular density of events along the surface. The reduced number of counts in the first and last strips in the Y dimension is due to the events where the charge collection is shared with strips outside the investigated zone. The effect is less noticed in the X dimension as charge sharing occurs much less frequently on the P side.

The expected result from a uniform irradiation would be a noisy image, with white noise. However, note that some correlation exists among the pixels belonging to a same strip. That is, some rows or columns of pixels appear "darker" than others. Indeed, the observation of the individual spectra on the cathode strips, which is less affected by charge sharing, revealed that significant differences in the number of events seen by each strip exist. The average number of photo-peak counts was approximately 2400 per strip, with deviations up to 10% from this value for some of the channels. The origin of this effect is not clear and will be investigated in the next campaign of measurements.

Straight mask at 45°

A thin (2–3 mm) rectangular iron sheet has been placed on the surface of the detector oriented 45° with respect to the strips. The detector has been irradiated with ^{241}Am and ^{57}Co.The obtained images are plotted in figure 5.14.

For ^{241}Am (left-hand image), the edge of the sheet is clearly distinguished, as it delimits two zones with differentiated intensity of counts. Note that, again, some strips appear brighter than others, due to the irregularitites on the number of counts mentioned above. On the right-hand image, the more penetrating ^{57}Co are little absorbed by the mask, which makes more difficult the observation of the pattern.

Collimator

A tungsten collimator with a 2 mm round aperture was finally used as mask. The piece was approximately 1 cm thick, enough to stop practically 100% of photons both at 60 keV and 122 keV. Obtained images are displayed in figure 5.15. Note that the edges of the collimator are better defined for the image

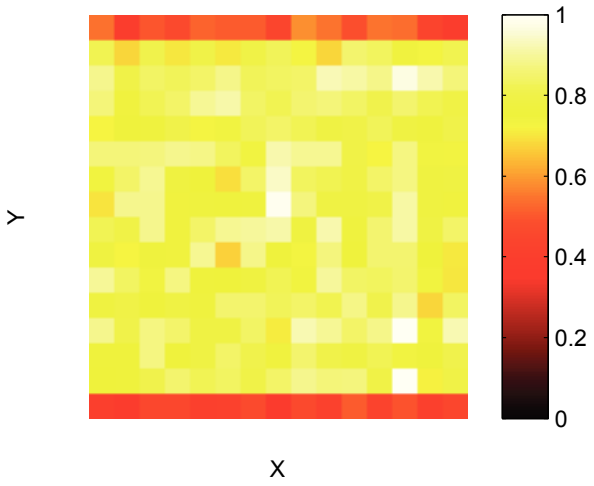

Figure 5.13: *Image obtained from the uniform irradiation of the detector by a ^{241}Am source.*

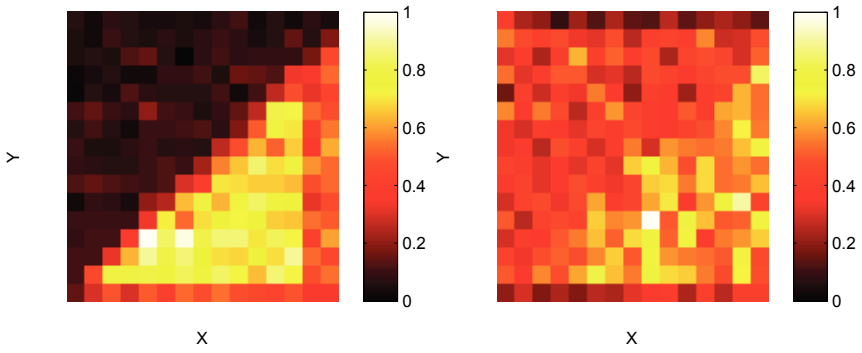

Figure 5.14: *Image obtained by shading the detector with a thin iron sheet, oriented 45° with respect to the strips. On the left, irradiation with ^{241}Am; on the right, irradiation with ^{57}Co.*

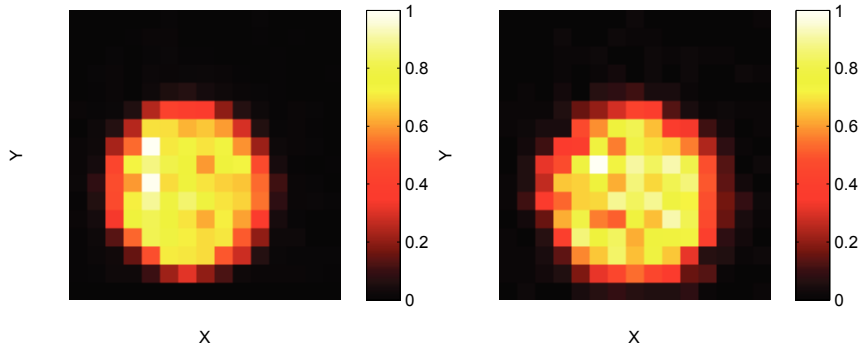

Figure 5.15: *Image obtained by shading the detector with a tungsten collimator. On the left, irradiation with ^{241}Am; on the right, irradiation with ^{57}Co.*

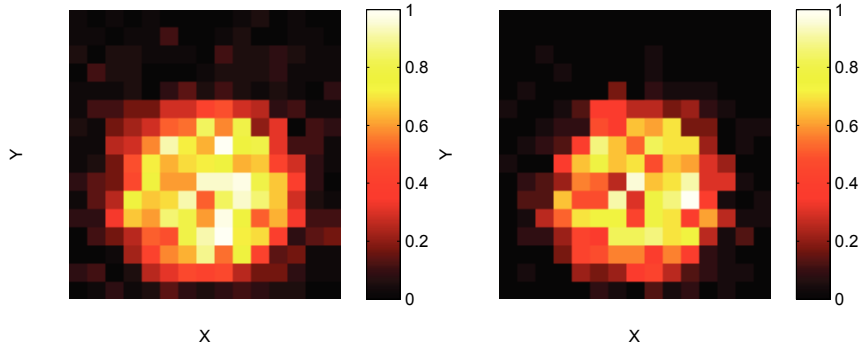

Figure 5.16: *Reconstruction of Compton events. The detector is irradiated using a ^{57}Co source and a tungsten collimator. On the left, representation of all the interactions (first and second) of all detected Compton events; on the right, only the first interaction is taken into account, which removes most of the hits outside the collimator print.*

corresponding to ^{241}Am. This is explained by the fact that incident photons do not arrive completely perpendicular to the detector plane (the source is not far enough). Therefore, a fraction of photons can penetrate through the interior walls of the collimator and travel a short path inside the tungsten before going out and interacting with the germanium. This has the effect of enlarging the collimator print, and is more accused as the energy of the radiation increases.

The use of the Collimator with the ^{57}Co source also allows us to verify the functioning of the matrix algorithm in the case of double interactions. Indeed, figure 5.16 (left) shows a plot of all Compton events located for this acquisition. In it, both the first and second interactions have been taken into account in the histogram. On the right, only the first interaction is plotted, we see that, as expected, almost all interactions outside the collimator print are removed, thus showing that we are capable of correctly identifying and reconstructing this kind of events.

5.5 Summary

In this chapter, the localization of the photons interaction point has been addressed. The *matrix algorithm* used to determine the number and position of each interaction is based on the comparison of the measured pulses with an *a priori* known set of responses to a basis grid of interaction points. In the presence of charge sharing effects or mirror charges, the position calculated by the algorithm is given with a precision better than the granularity of the grid. Thus, this is a suitable method for the assessment of the spatial resolution improvement that can be achieved through the exploitation of these phenomena.

The possibility to use the mirror charges has been explored through simulation, using the pulse shapes generated by MGS. It has been found that mirror charges are too weak to be effectively used below 100 keV, and, above that energy, much better signal to noise ratio than what is measured on our prototype would be required to obtain an improvement of the spatial resolution. As a consequence, the use of mirror charges is discarded for the application of the matrix method on the data acquired with the prototype.

On the other hand, we have shown that the use of charge sharing phenomena for improving the spatial resolution is easier than exploiting the mirror charges. However, the interpolated position yield by the algorithm is unsatisfactory, as it shows a concentration of points on the pixel centres. A fine calibration of the detector response is needed, taking into account the variation of the charge collected as a function of the interaction position between strips, is needed to correct these errors.

The application of the matrix method on several data acquisitions on the PheniX prototype has allowed a first validation of the positioning principles in the detector. The distributions along z for the irradiation of the detector using two different sources (^{241}Am and ^{57}Co) have been found coherent with

the theoretical absorption of Germanium at the corresponding energies. This validates the possibility of 3D localization using this type of detector. Finally, the images obtained using different masks to shadow parts of the detector have been presented, showing a good reconstruction of the pattern, and thus validating the imaging capability of the detector.

Conclusion

A system for the spectroscopy and imaging of a HPGe DSSD has been presented. The system is a candidate detector for an hypothetical new generation X-ray telescope, which would extend the focusing capabilities of current observatories, which today stop at 80 keV, up to a few hundred keV. The core of this work focuses on the implementation of a digital signal processing chain for the analysis of the impulsions. A set of algorithms has been developed with the following main purposes:

- Energy measurement chain. The energy on a single channel is measured in several steps. First, a trigger algorithm is in charge of detecting the presence of an impulsion on the channel. Those channels were an impulsion is detected are filtered to give them a trapezoidal shape. Finally, the energy of the impulsion is obtained by measuring the amplitude of the trapezoid by means of a matched filter.

- Calibration of the gain on each channel in presence of charge sharing events. Due to the narrowness and proximity of the strips, the charge of a single interaction is often collected by more than one strip of the same electrode. This phenomenon complicates the calibration in gain, which can no longer be carried out individually, but needs to take into account the sum of energies on all channels. A least mean square fitting algorithm has been implemented to find the gain coefficients that minimize the error of the summed energy with respect to the radioactive source used for calibration.

- 3D determination of the interaction position. Locating the interaction point in the detection plane is needed to reconstruct the image observed by the telescope. In addition, the information provided by the depth of interaction enables reduction of background and polarimetry capabilities. The *matrix method* used in [73] has been adapted to the case of a DSSD. This estimator is based on the knowledge of the detector response to a grid of points. The algorithm provides the combination of energy deposits on that basis grid that best fits the measured waveforms. Those energy deposits can then be used as weighting coefficients to calculate an interpolated position with a spatial resolution better than the granularity of the grid.

Simulation work

The signal processing chain has been tested using the signals generated with the MGS software [58] coupled to a Pspice model of the readout electronics. MGS simulations were used to determine the performances of the position estimation algorithm.

To validate the simulation of our prototype, the MGS potentials were compared to the ones calculated using analytical expressions, obtaining an excellent agreement between the theoretic results and those given by the numerical methods implemented in the simulator. In addition, the pulse shapes calculated by MGS were compared to those recorded on the prototype for different interaction points, again obtaining a good matching between the simulation and the reality.

One of the main purposes of the simulation was to study the possibility of improving the lateral spatial resolution using the mirror charges –fast transient signals that appear on the strips adjacent to the ones collecting the charge–. The accuracy of the position estimation was assessed for different energies in the range 1–200 keV, as a function of noise. Results showed that the use of mirror charges is only beneficial for energies above 100 keV and better noise levels than those measured on our prototype. In consequence, mirror charges where not exploited in the first tests on the prototype.

Experimental results with the PheniX detector prototype

A first measurement campaign on the PheniX detector was carried out. The first tests permitted to validate the energy measurement chain and successfully calibrate the detector using the proposed algorithm. Measured energy resolutions were 1.4 keV at 59.5 keV and 1.7 keV at 122 keV. .

Two types of charge losses were observed due to the splitting of the collected charge in multiple strips. The first type occurs when a strip collects an small amount of charge which is not detected by the trigger. This effect can not be corrected through signal processing and its severity depends on the spread of the charge cloud due to thermal diffusion during its drift towards the electrodes and the noise performances of the system (which determine the trigger threshold). The second type is related to slow collection times of the charges within the gap, due to weak lateral electric fields. A correction factor depending on the estimated interaction position can be calculated to compensate for this effect.

The estimation of the interaction position along the z axis was validated by comparing the distribution of detected events with the theoretical attenuation of the sources in Germanium, with good agreement obtained between theoretical and measured distributions. The location of the interaction point in the detection plane was tested by masking the detector with different patterns, which were correctly reproduced in the reconstructed images. In addition, the capability to identify and reconstruct the Compton events was demonstrated by removing the interactions of scattered photons located within the masked zone.

Summarizing...

- We developed and validated a system for the analysis of the impulsions in a HPGe DSSD for the X-ray astronomy, featuring almost entire digital implementation.
- Working in the digital domain represents several advantages: easy implementation of pulse shaping algorithms, flexibility in the signal processing, implementation of complex algorithms for the localization of the interaction point, etc.
- We have been able to characterize the response of the detector and readout electronics using two software: MGS and Pspice. This provides a useful tool for the validation and performance assessment of the current and future signal processing algorithms utilised in PheniX.
- We proposed a signal processing chain for the measurement of the energy and a method for the inter-channel calibration of the PheniX detector, both of which have been validated on real data.
- We have adapted the *matrix algorithm* for the location of the interaction point to the DSSD case. Its application on different data acquisitions has allowed to validate the basic principle of 3D localization in the detector.

Future work

The experimental setup for the PheniX detector prototype is still in an early stage and will be improved in the near future. A reduction of noise is expected from a new read out configuration where the input FET stage of the charge-sensitive amplifier will be moved closer to the strips. In addition, a new cooling system should allow to operate the detector at a temperature lower than the 115K of the first campaign. A better protection from mechanical vibrations should also significantly reduce the microphonic interference on the cathode side. From all this, a sensible improvement of the spectroscopic performances is expected in the next set of measurements. An increase of the number of readout channels is also foreseen, passing from the current 32 to 128. This will allow a deeper study of the multiple interactions and the use of the sensor for polarization measurements.

A more accurate assessment of the interaction location performances needs to be carried out. To do so, a system capable of precisely positioning and providing a fine collimation of the radioactive source is needed. The calculation of the interaction depth should be validated by irradiating the detector by an oblique beam in order to obtain different depths of interaction along a set of several pixels.

Finally, it must be pointed out that all the signal processing developed in this work was intended for off-line analysis of the ideal performances of the detector, with no concern on the computational cost. The adaptation of the algorithms to a real time processing system will be required in view to the future application on a real instrument.

Perspectives

At the time of writing, the PheniX team is working in an evolution of the experimental setup in order to solve the problems identified in the first set of measurements. In this new version, the extension of the total number of channels, from the current 32 to 128 (64 per side) is foreseen. The objective is to build a full demonstrator of the capabilities of the detector. If the expected performances can be demonstrated, next step could consist in equipping a stratospheric balloon with a similar prototype in order to test it in a spatial environment.

At the end, the PheniX experience should provide IRAP and the CNES with strong arguments in view of preparing an instrument proposal in response to eventual calls of the ESA or other spatial agencies.

Conclusion

Un système de spectroscopie et imagerie pour un détecteur HPGe type DSSD a été présenté. Ce système de détection est prêt pour un télescope X-durs de nouvelle génération, lequel étendrait la capacité de focaliser les photons, limitée à 80 keV pour les observatoires actuels, jusqu'à quelques centaines de keV. Le noyau de ce travail est l'implémentation d'une chaine de traitement numérique pour l'analyse des impulsions. Une série d'algorithmes a été développée avec les objectifs principaux suivants:

- Chaine de traitement pour la mesure de l'énergie. L'énergie sur un canal est mesurée en plusieurs étapes. D'abord, un algorithme de déclenchement détecte la présence d'une impulsion sur chaque piste. Ensuite, les voies qui ont déclenché sont filtrées pour donner à l'impulsion une forme trapézoïdale. Finalement, l'énergie de l'impulsion est obtenue par la mesure de l'amplitude du trapézoïde en utilisant un filtre adapté.

- La calibration en gain de chaque voie en présence d'événements présentant une delocalisation des charges. En raison de l'étroitesse et la proximité des pistes, la charge libérée lors d'une interaction est souvent collectée par plus d'une piste de la même électrode. Ce phénomène complique la calibration en gain, qui ne peut plus être réalisée individuellement, mais nécessite prendre en compte la somme d'énergies sur toutes les voies. Un algorithme d'ajustement par moindres carrées a été implémenté pour trouver les coefficients de gain qui minimisent l'erreur de la somme des énergies par rapport à l'énergie de la source de calibration.

- Détermination en trois dimensions de la position de l'interaction. Localiser le point d'interaction sur le plan de détection est nécessaire pour reconstruire une image de la région du ciel observée par le télescope. De plus, l'information donnée par la profondeur d'interaction permet une réduction du btuit de fond et la réalisation de mesures de polarisation. Le méthode de la matrice utilisée dans [73] a été adapté au cas d'un DSSD. Cet estimateur est basé sur la connaissance de la réponse du détecteur à une grille de points de référence. L'algorithme produit la combinaison qui s'adapte le mieux aux formes des pulses mesurés. Ces dépôts d'énergie peuvent être utilisées

comme coefficients de pondération pour calculer une position interpolée avec une résolution spatiale meilleur que la granularité de la grille.

Travail de simulation

La chaine de traitement de signal a été testée en utilisant les signaux générées avec le software MGS[58] couplés à un modèle Pspice de l'électronique de lecture. Les simulations MGS ont été utilisées pour déterminer les performances de l'algorithme d'estimation de la position.

Pour valider la simulation de notre prototype, les potentiels calculés avec MGS ont été comparés avec ceux obtenus en utilisant des expressions analytiques. La concordance entre trouvée les deux a été excellente. En plus, les formes de pulse calculées par MGS ont été comparées à celles acquises avec le prototype pour différentes profondeurs d'interaction, montrant une correspondance étroite entre la simulation et la réalité.

Un des objectifs principaux de la simulation était d'étudier la possibilité d'améliorer la résolution spatiale latérale au moyen des *charges miroir* –signaux transitoires rapides qui apparaissent sur les pistes voisinant celles où la charge est collectée–. La précision de l'estimation de la position a été évaluée pour différentes énergies dans l'intervalle 1-200 keV, en fonction du bruit. Les résultats montrent que l'utilisation des *charges miroir* est seulement avantageuse pour énergies au delà de 100 keV si les niveaux de bruit sont meilleurs que ceux mesurées sur notre prototype. En conséquence, les charges miroir n'ont pas été exploitées pour les premiers tests en laboratoire.

Résultats expérimentaux avec le prototype PheniX

Une première campagne de mesures avec le prototype PheniX a été réalisée. Les premiers tests ont permis de valider la chaine de mesure de l'énergie et calibrer le détecteur avec succès en utilisant l'algorithme proposé. Les résolutions en énergie mesurées ont été de 1.4 keV à 59.5 keV et 1.7 keV.

Deux types de pertes de charge ont été observées due à la répartition de la charge collectée entre plusieurs pistes. Le premier type apparait quand une piste collecte une petite quantité de charge, insuffisante pour être détectée par le trigger. Cet effet ne peut pas être corrigé par traitement du signal et sa sévérité dépend de l'expansion du nuage de charge par effet de la diffusion thermique pendant le trajet des charges vers les électrodes. et les performances de bruit du système (qui déterminent le seuil du trigger). Le deuxième type concerne les temps de collection de charge lents au niveau du gap entre deux pistes, due à la faiblesse du champ électrique latéral dans ces régions. Un facteur de correction selon la position de l'interaction peut être calculé pour compenser cet effet.

L'estimation de la position de l'interaction au long d l'axe z a été validée par comparaison de la distribution d'événements détectés avec l'atténuation théorique des sources dans le Germanium, avec

une bonne correspondance obtenue entre les distribution théoriques et celles mesurées. La localisation du point d'interaction sur le plan de détection a été testée en masquant le détecteur avec différentes figures, lesquelles ont été correctement reproduites sue les images reconstruites. En plus, la capacité d'identifier et reconstruire les événements Compton a été démontrée en éliminant les interactions dues à la deuxième interaction Compton dans la zone masquée.

Synthèse...

- Nous avons développé et validé un système pour l'analyse des impulsions pour un détecteur HPGe type DSSD pour l'astronomie X, implémenté presque totalement dans le domaine numérique.
- Travailler dans le domaine numérique représente plusieurs avantages: implémentation facile des algorithmes de *pulse shaping*, flexibilité du traitement, implémentation d'algorithmes complexes pour la localisation du point d'interaction, etc.
- Nous avons caractérisé la réponse du détecteur et l'électronique de lecture utilisant deux software: MGS et Pspice. Ça nous donne un outil pour la validation et évaluation des performances pour les actuels et futurs algorithmes de traitement du signal utilisés pour PheniX.
- Nous avons proposé une chaine de traitement du signal pour la mesure de l'énergie et une méthode pour la calibration inter-canaux du prototype PheniX. Toutes deux ont été validées avec des données réelles.
- Nous avons adapté un algorithme matriciel pour la localisation du point d'interaction au cas d'un DSSD. Son application sur différentes acquisitions de données nous a permis de valider le principe basique de localisation 3D du détecteur.

Travail futur

La mise en oeuvre du prototype PheniX est encore dans une phase préliminaire et va être amélioré en un futur prochain. Une réduction de bruit est attendue grâce à une nouvelle configuration de lecture où le FET d'entrée de l'amplificateur de charge sera rapproché des pistes. En plus, un nouveau système de refroidissement devrait permettre de baisser la température d'opération de la diode au dessous des 115K de la première campagne. Une meilleure protection contre les vibration mécaniques devrait aussi réduire d'une façon significative les interférences de microphonie sur la cathode. Pour tout ça, une amélioration des performances spectroscopiques est attendue pour les prochaines mesures. Un incrément du nombre de canaux de lecture est aussi prévu, passant des actuels 32 à 128. Ça permettra une

étude plus approfondie des interactions multiples et l'utilisation du senseur pour faire des mesures de polarisation.

Une évaluation plus précise des performances de localisation du point d'interaction est nécessaire. Pour cela, un système capable de positionner précisément la source radioactive, tout en proportionnant une fine collimation du faisceau, est requise. Le calcul de la profondeur d'interaction devra être validé par le biais d'une irradiation oblique du détecteur afin d'obtenir différentes profondeurs d'interaction au long de plusieurs pixels consécutifs.

Finalement, on doit noter que tout le traitement du signal développé dans ce travail est orienté pour un analyse off-line des performances du détecteur, sans souci du coût de calcul. L'adaptation des algorithmes à un traitement en temps réel sera nécessaire en vue de leur future application sur un instrument opérationnel.

Perspectives

Au moment d'écrire cette thèse, l'équipe PheniX travaille sur l'évolution de l'expérience. Dans cette nouvelle version, le nombre total de voies sera étendue, passant des actuelles 32 à 128 (64 par électrode). L'objectif est de construire un démonstrateur complet des capacités du détecteur. Si les performances attendues peuvent être démontrées, le prochain pas pourrait consister à équiper un ballon stratosphérique avec un similaire prototype afin de le tester dans un environnement spatial.

à la fin, l'expérience PheniX devrait doter l'IRAP et le CNES avec des forts arguments en vue de préparer une proposition d'instrument en réponse des éventuels appels d'offre de l'ESA ou autres agences.

Appendix A

Influence of the baseline on the energy measurement

A.1 Error on the energy measurement due to a baseline shift

If we suppose that a small continuum remains after the baseline removal block, the recorded input signal, $s(t)$, can be expressed as:

$$s(t) = [x(t) + n(t) + C]u(t) \tag{A.1}$$

where $u(t)$ is the unitary step function, which is used to mark the start of the record at t=0. $x(t)$ is the charge amplifier output pulse, given by

$$x(t) = Ae^{-(t-t_0)/\tau}u(t - t_0) \tag{A.2}$$

$n(t)$ is the electronic noise and C is the continuum value.

To measure the energy, the signal $s(t)$ is filtered by a trapezoidal shaper, and after that, the shaper output is correlated with the trapezoid pattern. The height of the correlation peak determines the energy measurement, and appears when the pattern is aligned with the filtered trapezoid at $t = t_0$. In consequence, in order to assess the impact of the continuum, the correlation output at $t = T_0$ due to the $Cu(t)$ must be calculated.

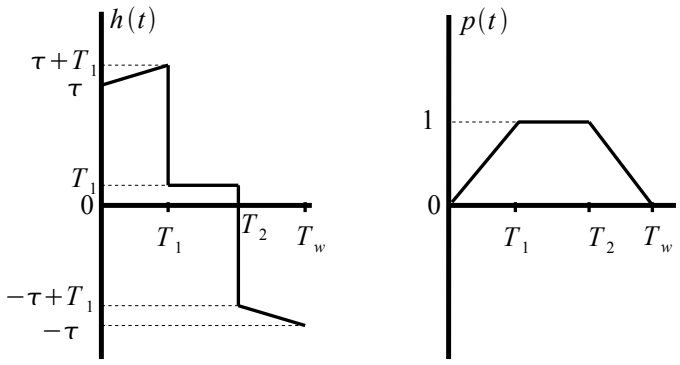

Figure A.1: *Impulse response of the trapezoid shaper (on the left) and trapezoid pattern used in the correlation (on the right).*

First step consists in determining the interfering signal at the shaper output, $i_o(t)$, given by the convolution of $Cu(t)$ and the filter impulse response $h(t)$, which has the shape illustrated in figure A.1. $i_o(t)$ is then:

$$i_o(t) = \frac{1}{T_1\tau}h(t) * Cu(t) = \frac{C}{T_1\tau}\int_0^{T_w} h(r)u(t-r)dr \tag{A.3}$$

The normalizing factor $\frac{1}{T_1\tau}$ is used to obtain the same amplitude A on the trapezoid than in the input exponential pulse. If we suppose that the number of pre-trigger samples is configured so as t_0 is greater than the trapezoid width, T_w, only the filter output for $t > T_w$ needs to be calculated. Then, equation A.3 simply yields:

$$i_o(t) = \frac{C}{T_1\tau}\int_0^{T_w} h(r)dr = \frac{CT_2}{\tau} \tag{A.4}$$

The correlation of $i_0(t)$ with the trapezoid pattern p(t), at $t = t_0$, is given by:

$$\epsilon = \frac{\int_{t_0}^{t_0+T_w} s_0(t)p(t-t_0)dt}{\int_0^{T_w} p^2(t)dt} = \frac{3CT_2(T_1+T2)}{\tau(3T_2-T_1)} \tag{A.5}$$

The denominator is the autocorrelation of $p(t)$ at $t = 0$, and is used as a normalizing factor to maintain the input amplitude A on the output correlation peak. Expression A.5 in terms of the width of

the trapezoid raising edge, T_r ($T_r = T_1$) and the width of the flat top, T_t ($T_2 = T_t + T_r$), yields:

$$\epsilon = \frac{3C(2T_r + T_t)(T_r + Tt)}{\tau(3T_t + 2T_r)} \tag{A.6}$$

A.2 Error on the energy measurement due to a ramp like interfering signal

In the case of an interfering ramp signal, the recorded input signal, $s(t)$, can be expressed as:

$$s(t) = [x(t) + i(t) + n(t)]u(t) \tag{A.7}$$

where $u(t)$ is the unitary step function, which is used to mark the start of the record at t=0. $x(t)$ is the charge amplifier output pulse, given by

$$x(t) = Ae^{-(t-t_0)/\tau}u(t - t_0) \tag{A.8}$$

$i(t)$ is the ramp like interference,

$$i(t) = mt \tag{A.9}$$

and $n(t)$ is the electronic noise.

To measure the energy, the signal $s(t)$ is filtered by a trapezoidal shaper, and after that, the shaper output is correlated with the trapezoid pattern. The height of the correlation peak determines the energy measurement, and appears when the pattern is aligned with the filtered trapezoid at $t = t_0$. In consequence, in order to assess the impact of the interfering signal, the correlation output at $t = T_0$ due to $i(t)$ must be calculated.

First step consists in determining the interfering signal at the shaper output, $i_o(t)$, given by the convolution of $i(t)$ and the filter impulse response $h(t)$, which has the shape illustrated in figure A.1. Before entering the filter, the baseline removal block subtracts the baseline value right before the trigger point. $i_o(t)$ is then:

$$i_o(t) = \frac{1}{T_1\tau}h(t) * (i(t) - i(t_0))u(t) = \frac{1}{T_1\tau}\int_0^{T_w} h(r)[i(t - r) - mt_0]u(t - r)dr \tag{A.10}$$

The normalizing factor $\frac{1}{T_1\tau}$ is used to obtain the same amplitude A on the trapezoid than in the input exponential pulse. If we suppose that the number of pre-trigger samples is configured so as t_0 is greater than the trapezoid width, T_w, only the filter output for $t > T_w$ needs to be calculated. Developing equation A.10, we obtain:

$$\begin{aligned} i_o(t) &= \frac{1}{T_1\tau}\left[\int_0^{T_1}(\tau+r)m(t-r)dr + \int_{T_1}^{T_2} T_1 m(t-r)dr \right. \\ &+ \left. \int_{T_2}^{T_w}(-r+T_w-\tau)m(t-r)dr - mt_0T_1T_2\right] \\ &= m\frac{T_2}{\tau}(t-t_0+\tau-T_w/2) \end{aligned}$$

As $\tau >> Tw/2$, the interference at the shaper output can be simplified to:

$$i_o(t) \approx mT_2(1+\frac{t-t_0}{\tau}) \tag{A.11}$$

The correlation of $i_0(t)$ with the trapezoid pattern p(t), at $t = t_0$, is given by:

$$\epsilon = \frac{\int_{t_0}^{t_0+T_w} s_0(t)p(t-t_0)dt}{\int_0^{T_w} p^2(t)dt} \tag{A.12}$$

The denominator is the autocorrelation of $p(t)$ at $t = 0$, and is used as a normalizing factor to maintain the input amplitude A on the output correlation peak.

As $\frac{t-t_0}{\tau} << 1$ for $t_0 < t < T_w$, $i_0(t)$ can be further simplified to

$$i_o(t) \approx mT_2 \tag{A.13}$$

Hence, expression A.12 yields:

$$\epsilon \approx \frac{mT_2\int_0^{T_w} p(t)dt}{\int_0^{T_w} p^2(t)dt} = \frac{3mT_2(T_1+T_2)}{3T_2-T_1} \tag{A.14}$$

which, in terms of the width of the trapezoid raising edge, T_r ($T_r = T_1$) and the width of the flat top, T_t ($T_2 = T_t + T_r$), yields:

$$\epsilon \approx \frac{3m(T_r + T_t)(2T_r + T_t)}{2T_r + 3T_t} \tag{A.15}$$

Appendix B

Publication in NIM A.

The adaptation of MGS to the simulation of a DSSD was the object of a publication[61] in *Nuclear Instruments and Methods in Physics Review A*, which is appended in the following pages. The purpose of the article was to validate the use of MGS for the simulation of a DSSD. To do so, a comparison was made between the pulse shapes calculated by the software, and those measured on the prototype. The comparison was made for different interaction depths, showing an excellent agreement. The depth of the measured pulses was determined from the measurement of the difference in time of arrival between the anode and cathode pulses. A nearly linear relationship between this parameter and the depth of the interaction was demonstrated using MGS. Finally a reflection was included on the limitations of the simulation, for instance, for the characterization of charge sharing phenomena, and possible modifications to improve the tool.

Simulation of the charge collection and signal response of a HPGe double sided strip detector using MGS

I. Mateu[a,b,*], P. Medina[c,1], J.P. Roques[a,b], E. Jourdain[a,b]

[a] *Université de Toulouse; UPS-OMP; IRAP; Toulouse, France*
[b] *CNRS; IRAP; 9 Av. colonel Roche, BP 44346, F-31028 Toulouse cedex 4,France*
[c] *IPHC, IN2P3 - CNRS/Université Louis Pasteur, 23 rue du Loess, PB28, Strasbourg Cedex 2, F67037 - France*

Abstract

This paper aims to present *Multi geometry Simulation (MGS)*, a software intended for the characterization of the signal response of solid state detectors. Its main feature is the calculation of the pulse shapes induced at the electrodes of the detector by a photon-semiconductor interaction occurring at a specific position inside the detector volume. The program uses numerical methods to simulate the drift of the charge carriers generated by the interaction, as the movement of these particles induces the useful signal for detection to the electrodes. After the description of the tool fundamentals, an example of application is presented where MGS was used for simulating a High Purity Germanium (HPGe) double sided strip detector conceived for hard X-ray astronomy. Simulated and measured pulse shapes are compared for interactions occurring at different depths in the detector volume. The comparison focuses on the difference in time of arrival between the anode and cathode pulses, as this measure allows, together with the X/Y information retrieved from the strips, a 3D determination of the photon interaction point, which is an important feature of the detector. A good matching between simulations and measurements is obtained, with a discrepancy less than 0.5 mm between the measured and the simulated depth of the interaction, for an 11 mm thick detector.

Keywords:
X-ray, HPGe, DSSD, Pulse shape calculation

1. Introduction

Semiconductor detectors are used in a wide range of fields such as spectrometry, particle physics, astrophysics, medicine... In such systems, pulse shape analysis is used for many purposes, from determining the position of the interaction[1], to removing Compton continuum[2], or rejecting background[3]. Therefore, being able to anticipate the signal response can be of great importance in the conception of a new detector, as it provides a means to test the pulse shape analysis through simulation, and to predict the performance of the design before manufacture. Moreover, some algorithms used in pulse shape analysis rely on the comparison of the measured signal to a basis of signals previously acquired through scan of the detector in different positions. This process may be very time-consuming and requires the use of sophisticated scanning systems, capable of positioning the source with enough precision at every scanning point, and with a fine collimation to limit the photon dispersion around the aimed spot. The use of a simulation tool can be a good alternative when such a scan is not practical or not available.

This paper presents MGS[4], a Matlab[5] based software whose purpose is to characterize the signal response of solid state detectors. MGS stands for *Multi Geometry Simulation*, and refers to the software capability to simulate detectors of different geometries. The program was developed and validated by Medina et al. [4] in the frame of the AGATA[6] project. MGS is well adapted to the simulation of single wafer semiconductor volumes of the order of some millimetres to a few centimetres -For instance, it was used for the simulation of pixelated CdZnTe sensors in [7]-, while it is not recommended for detectors of smaller sizes, which can

*Corresponding author. Telephone: +33 (0)5 61 55 65 54
Email addresses: isidre.mateu@irap.omp.eu (I. Mateu), patrice.medina@aero.obs-mip.fr (P. Medina), jean-pierre.roques@irap.omp.eu (J.P. Roques), elisabeth.jourdain@irap.omp.eu (E. Jourdain)
[1] Present address: LA-OMP-CNRS, 14 avenue Edouard Belin, 31400 Toulouse

be modelled by more adapted software, such as ISE-TCAD[8] tools for silicon MOS detectors. MGS is utilized here to simulate a *double sided strip detector* (DSSD) conceived for X-ray astronomy. Following sections are structured as follows: first, a description of the working principles of MGS is given; then, a comparison between the pulse shapes obtained by simulation of the DSSD and the ones measured with a laboratory prototype is reported. Finally, before reaching the conclusions, the advantages and drawbacks of the simulator are discussed.

2. Description of MGS

Photons interact with semiconductor materials through different physical processes (photoelectric absorption, Compton scattering, pair production...), in many cases transferring a part of their energy to an electron. This electron creates a cloud of electron-hole pairs along its path from the interaction point, which constitute the basic information carriers in a semiconductor detector. For the investigated detector, the detection principle consists in making these charge carriers drift in an electric field in order to generate an electrical signal on one or multiple electrodes. In spectroscopic applications, typically, a charge sensitive amplifier is used at each electrode to calculate the integral of the current induced by the motion of the carriers, which is equal to the collected charge (i.e. the charge of the particles that reach the electrode at the end of their trajectory). As a first order approximation, the number of generated carriers depends on the energy deposited by the interaction, which in consequence can be deduced from the pulse analysis, with some uncertainty due to charge trapping or charge loss in the case of interactions occurring near the surface between two contacts. Detectors can present segmented electrodes with one readout channel per segment. In such a configuration, the segment, also called strip, above (or under) the energy deposit point will collect most of the charge, thus allowing to gain position information for imaging purposes.

The goal of MGS is to mimic this behaviour and calculate the signal response to one or multiple interactions taking place at positions defined by the user. At the beginning of a new detector simulation, the following calculation stages are carried out in order to characterize the detector:

1. Definition of the geometry of the detector and its working parameters.
2. Solution of the electric potential for all the volume.
3. Calculation of the electric field.
4. Obtaining the velocity vector applied to the charge carriers at every point of the detector volume.
5. Calculation of the weighting potentials.[2]

These are necessary steps for the determination of the charge carrier trajectories and signal response. After they have been performed, the user can define an interaction at any point of the detector volume. The program then places an electron-hole pair at that position, calculates the path of the charges from the interaction point to their respective electrodes (electron drifting towards the anode and hole drifting towards the cathode), and uses these trajectories to determine the signal response of each electrode through application of the Shockley-Ramo theorem[9]. Note that MGS simplifies the cloud of charge carriers that would appear in a real interaction to a single electron-hole pair carrying the whole energy of the photon.

Further detail on each of the listed steps of the simulation is provided below. The explanation of the weighting potential is grouped together with the charge carrier trajectory calculation and Shockley-Ramo theorem for a better understanding.

2.1. Definition of the geometry

The program uses a grid, a matrix of points in space, to represent the volume corresponding to the detector. The detector geometry is defined using several layers. Each one identifies the points of the grid corresponding to a part of the detector. There are 5 different layers: semiconductor bulk, anode, cathode, isolating material surrounding the detector, and external capsule. In order to obtain a desired geometry, the user has just to choose among several pre-defined templates, each one corresponding to common detector types, and introduce the dimensional parameters. For instance, some of the required parameters for the planar template -used for defining a DSSD- are: detector dimensions, number of strips per side, width of the strips, separation between strips, etc. An example plot of this template is shown at figure 1, where, for the sake of clarity, the electrodes are segmented in only 10 strips. A great advantage of this approach is that the template completely defines the detector, and the code is transparent to the chosen geometry for all subsequent steps of the simulation. This means that it is possible for a user to simulate a new type of detector just by creating the appropriate template, without having to modify the rest of the code.

[2]The weighting potentials are explained in section 2.4 as a part of the Shockley-Ramo theorem

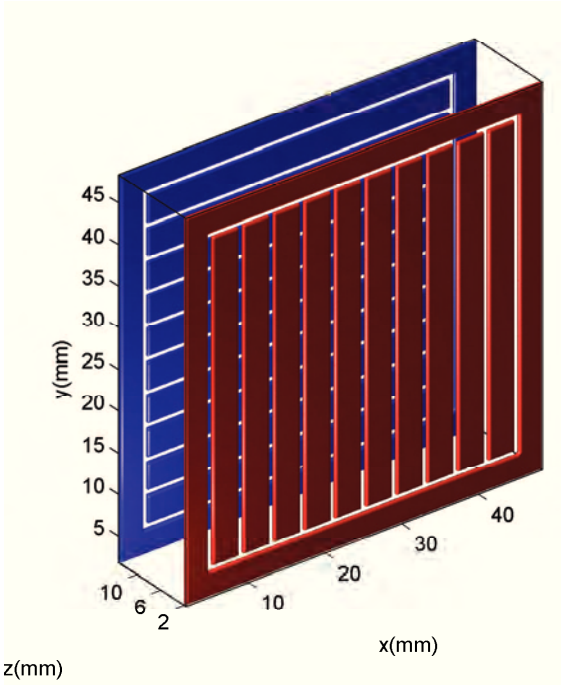

Figure 1: Example of a DSSD geometry represented with MGS. Both electrodes are segmented in 10, 3.5 mm wide strips, with a 50 mm gap between strips. The sensor thickness is 11 mm.

2.2. *Calculation of the electric potential and electric field*

When an energy deposition occurs in the detector, a cloud of positive (holes) and negative (electrons) charge carriers is produced in the surroundings of the interaction point, whose size and shape depend on the amount of deposited energy and the type of interaction. These charged particles immediately drift towards the electric contacts, as a result of the electric field produced by the bias voltage applied to the electrodes. Therefore, to determine the trajectory of the carriers, the first step consists in computing the electric potential inside the detector. This is done through solution of Poisson's equation:

$$\nabla^2\phi = -\frac{\rho}{\epsilon} \tag{1}$$

The boundary conditions of the problem are given by the bias voltage applied between the anode and the cathode, and the grounding of the outer-most points of the grid, simulating an encapsulated detector. The intrinsic space charge density in the bulk is proportional to the density of acceptors or donors in the p- or n-type detector material. The user has to define the concentration of impurities at the two extremes of the bulk (near cathode and near anode). This way, a gradient of space charge density along the crystal is considered. The equation is formulated in its finite difference form, resulting in a determined system of linear equations. MGS allows for a direct solution of the system provided the computer has enough memory. Otherwise, two iterative methods are implemented: *Jacobi's method*[10, p.892] and *successive over relaxation (SOR)*[11]. The number of iterations required by SOR to converge is proportional to N, with N being the total number of grid points, while Jacobi's method converges with a number of iterations proportional to N^2. So SOR is usually faster. Figure 2 shows the potential obtained for the same detector example of figure 1, while figure 3 shows a comparison of the obtained potential between a DSSD and a non segmented parallel plate detector in the region near the electrodes, showing the effect of the segmentation on the field lines. After solution of the electric potential, the electric field is obtained from the negative gradient.

2.3. *Obtaining the velocity vector*

The electric field is used for calculating the drift velocity vector matrices for positive and negative charge carriers. That is, for each point of the grid, the velocity vector that would be applied to a charged particle at that point is determined. At low electric fields (below approximately 100 V/cm for Germanium), drift velocities are directly proportional to the electric field with a

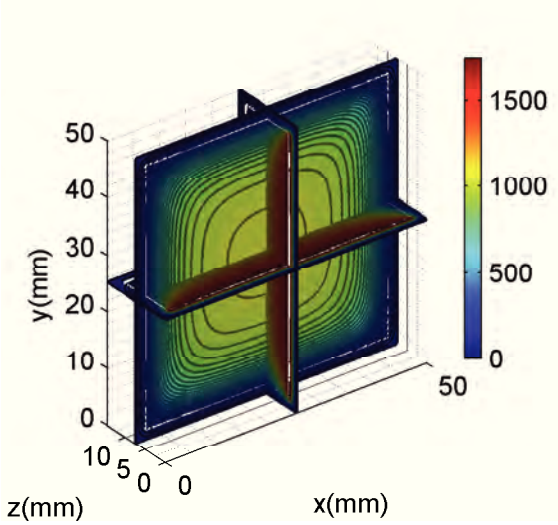

Figure 2: Perspective view of the electric potential of a DSSD, as calculated by MGS.

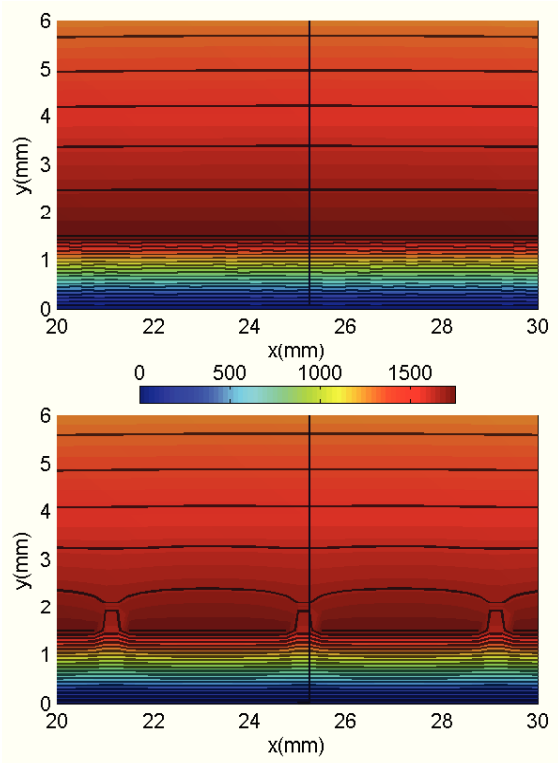

Figure 3: Comparison of the potential calculated by MGS for a non segmented parallel plate detector (top) and a DSSD (bottom) in the region near the electrodes.

mobility coefficient μ, which is different for holes and electrons. At higher electric fields, this linear relationship is lost and drift velocities increase slower with the field value, until reaching a maximum saturation velocity. This is the most usual operating mode for the investigated type of detectors (and it is also the case for our prototype). The mobility of the carriers is simulated in MGS by means of two models: the first, developed by Mihailescu et al.[12], accounts for the mobility of electrons, and the second, by Bruyneel[13], accounts for the mobility of holes. These models take into account anisotropy effects on the charge transport, due to the orientation of the semiconductor lattice. However, they do not consider the *Gunn effect*, observed by Ottaviani et al.[14] for high electric fields, above 3 kV/cm. This has no serious implications for our application, as our detector is operating at a voltage well below this threshold. The models assume a lattice temperature of 78 K, which is commonly used for Germanium. However, our detector is operating at 110 K. A difference in charge carrier velocity was expected from this difference in temperature, so we have modified the MGS code by re-scaling the calculated drift velocities, according the expressions for saturation velocity as a function of temperature given in [15].

2.4. *Charge carrier trajectory, Shockley-Ramo theorem and weighting potentials*

Using the drift velocity matrices, the program is able to compute the trajectory of point-like charges of either polarity drifting from the interaction point to the electric contacts. The actual charge cloud is modelled by a single positive and negative pair of particles whose charge is equivalent to the deposited energy. The interaction point does not need to belong to the grid, as the program interpolates the velocity vector value using the values of the grid points nearby. Having determined the velocity vector at the interaction point, a new position is computed as the initial position plus the velocity vector multiplied by a time step. This process is repeated iteratively until the carrier reaches an electrode. The sequence of intermediate positions defines the carrier trajectory. Again, interpolation is performed at each new calculated position to determine the velocity vector[3]. By default, interpolation is linear, but the code can easily be changed to include the MATLAB option for polynomial interpolation. However, for large matrices,

[3] Since the velocity is very close to saturation the error of assuming a constant velocity instead of integrating along each individual piece of trajectory is negligible.

memory outage can occur with this type of interpolation. A typical time step value is of the order of 1 ns, which for drift velocities of the order of 10^7 cm/s (saturation velocity of carriers in Germanium[16, p. 342]), yields a displacement of about 100 μm per time step.

The motion of holes and electrons inside the detector volume induces current on the electrodes. The signal response is obtained through the application of the Shockley-Ramo theorem. The charge induced on an electrode due to a point charge q moving under the effect of the electric field created by the bias voltage, is given by the following expression:

$$Q(t) = -q \cdot \phi_o(\vec{r}(t)) \tag{2}$$

where ϕ_o is called the *weighting potential*, and is defined as the electric potential that would exist at the instantaneous position of q, designed $\vec{r}(t)$, if the electrode of interest was set at unit potential while the rest of electrodes were grounded and all charges removed. Applying the theorem for the whole carrier trajectory yields the induced charge as a function of time. Note that, as for the velocity vector, the weighting potential at each intermediate position of the trajectory is obtained by interpolation from the nearby grid points. As the potential is a cubic function, it varies rapidly in the proximity of the electrode, so attention has to be made to the choice of the grid step to avoid large variations of the weighting potential between two consecutive grid points; or, alternatively, cubic interpolation must be used. The total charge computed by MGS is the sum of the signals due to the drift of the positive and negative carriers towards the opposite electrodes of the detector. Finally, the current pulse is obtained through the derivation of the charge signal:

$$I(t) = \frac{dQ(t)}{dt}$$

In order to compute the response at one contact, the Poisson equation must be re-solved to obtain its weighting potential, and this is in fact the last step of the characterization of the detector. The process is identical to the one described above to solve the actual potential. Note that for highly segmented detectors, the need of computing the weighting potential for every contact may be problematic in terms of memory storage and simulation duration. If the total number of grid points is large, solving the Poisson's equation may be significantly time-consuming, and the resulting matrices of a considerable size. In order to make the simulation more flexible, MGS allows the user to choose to compute the weighting potential only for certain segments. This may be useful if only the response of a limited region of the detector is of interest.

Alternatively to the numerical solution of Poisson's equation, weighting potentials can be calculated analytically under certain assumptions. [17] gives an expression to calculate the real potential of a planar detector with segmentation only in one of the electrodes. The potential is calculated in the plane orthogonal to the strips (no variation is considered along the direction of the strips), and supposing a detector of infinite size. The expression is then:

$$\phi(x,y) = a_0\left(\frac{y}{D}\right) + \sum_{n=1}^{\infty} a_n cos\frac{2\pi n}{P}x \cdot \left(\frac{sinh\frac{2\pi n}{P}y}{sinh\frac{2\pi n}{P}D}\right) \tag{3}$$

with

$$a_0 = \frac{1}{P}\int_0^P \phi_D(x)dx, \qquad a_n = \frac{2}{P}\int_0^P \phi_D(x)cos\frac{2\pi n}{P}xdx$$

where x and y represent the position coordinates in the directions parallel and perpendicular to the electrodes, respectively. The potential is assumed to be periodic with period P, where P represents the strip pitch, so the formula applies only for $0 < x < P$. D is the detector thickness and $\phi_D(x)$ is the potential on the strip surface ($y = D$). The potential on the opposite electrode is set to 0 ($\phi(x, 0) = 0$).

The expression was utilized for calculating the weighting potential for a strip at the center of our detector, assuming a segmentation pitch much larger than the strip width W, i.e, $P >> W$. The function $\phi_D(x)$ was defined as follows:

$$\phi_D(x) = \begin{cases} 1 & \text{if } |x| < W/2, \\ \frac{|x|-W/2}{G} & \text{if } W/2 < |x| < W/2 + G, \\ 0 & \text{if } W/2 + G < |x| < P/2. \end{cases} \tag{4}$$

where G is the width of the gap between strips. This approximates well the potential distribution considered for the weighting potential calculation, where the strip of interest is set to 1, and the rest of strips to 0. A linear decrease from 1 to 0 has been chosen for the gap, using the approximation proposed in [17] for a similar calculation.

In order to compare the analytical and numerical approaches, a small DSSD was simulated with MGS. The strip and gap widths were the same as those of our prototype, but each electrode was segmented only in 21 strips, instead of 100 for the prototype. Detector thickness was also reduced to 5 mm. Figure 4 shows a comparison between the weighting potential along the axis

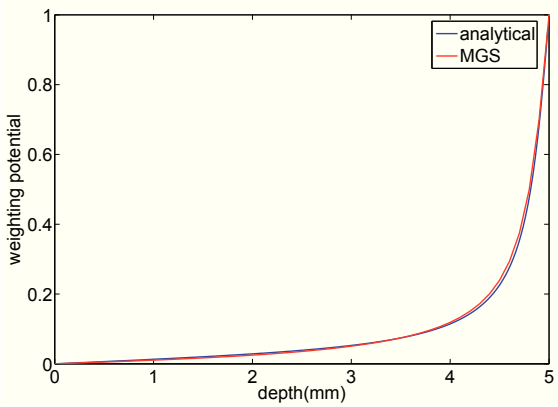

Figure 4: Comparison of the weighting potential obtained with MGS and the one calculated using expression 2.4, for a 5 mm thick DSSD. Each electrode surface is segmented in 21, 350 μm wide strips, with a 50 μm gap between strips. Results are shown for the central strip in its axis along the z dimension.

of the central strip, calculated with MGS and using the analytical expression. Agreement between both figures is evident. This suggests that MGS could benefit from the use of the analytical approach in the regions of the detector where the assumptions of infinite size hold, that is in the central parts of the volume. However, the use of numerical methods remains necessary to properly simulate the effects of the borders on the outermost strips.

3. Comparison of simulated and measured pulse shapes in a double sided strip detector

In order to assess the validity of the pulse shapes obtained with MGS, a simulation of a DSSD prototype was carried out, and the predicted signals were compared to pulses measured in the laboratory. One of the main features of this kind of detector is its ability to locate the depth of the interaction, thus providing a three-dimensional estimation of the position of the interaction. Some interaction position estimation algorithms[18] [19, pag. 29] that could be relevant for this detector are based on an *a priori* knowledge of the detector response for a number of predefined grid points. This response basis can be obtained through precise scanning of the actual detector, or simulated using tools such as MGS. The spatial resolution of this kind of algorithms directly depends on the density of the basis mesh. For our prototype case, the target is a resolution between 1 and 2 mm in the depth direction. Therefore, measured and simulated pulses were compared for 8 equispaced points along the detector thickness, separated by steps of 1.375 mm. The good matching between simulation and measurements validated MGS as a tool for studying the achievable performances of the intended 3D localization algorithms.

3.1. Materials and methods

3.1.1. Detector and acquisition system

The prototype (figures 5, 6) is a HPGe DSSD, designed for a wide coverage in the X-ray domain (between 1 and 200 keV). The wafer thickness is 11 mm, and the electrodes have a useful surface of 4x4 cm segmented into 350 μm wide strips, with a 50 μm gap between strips. We thus have 100 strips 4 cm long on each side of the detector. The detector has been manufactured by Canberra France and operates under a bias voltage around 1700 V. The anode strips are orthogonally oriented with respect to the cathode ones, defining pixels. This way, when an energy deposition is detected, its interaction point is determined by the intersection of the strip that collects the charge at the anode side, with the strip that collects the charge at the cathode side. This is the basic algorithm when a single energy deposition occurs. In case of a double interaction (e.g. a Compton interaction followed by a photoelectric absorption) four strips are involved and the algorithm is more complex. In the framework of this paper, these events, when possible, were separated by searching for coincidences on the measured energies between the anode and the cathode, and then treated as single events. When different energy deposits were found on one side with respect to the other, the event was rejected by the data analysis.

For the first tests, only the response of the 16 central strips of each side was acquired. Each strip was readout by an Amptek A250F charge amplifier, after which custom electronics were realized for removing the amplifier offset and further amplification of the signal. Finally, a CAEN N6740 acquisition card, with a 62.5 MHz sampling rate, was used for digitizing the pulses. The trigger signal for the acquisition was generated using two trigger circuits, whose inputs were the sum of the 16 anode strip signals in one case, and the sum of the 16 cathode strip signals in the other. The final trigger was activated only when both circuits triggered in coincidence to select events in the 16 $strips \times 16\ strips$ ($6.4mm \times 6.4\ mm$) area where the investigated strips overlap. The trigger signal was common to the 32 channels, ensuring that all channels were synchronously sampled. Following the arrival of each trigger, the waveforms of the 32 channels were digitized and stocked for off-line analysis. All subsequent signal processing was performed in the digital domain.

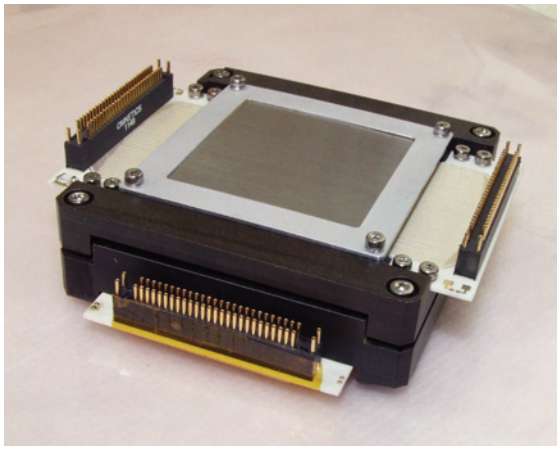

Figure 5: Detector prototype as delivered by the manufacturer. The external capsule with four sets of pin connectors (one per strip) can be observed. A beryllium window on the top delimites the usable surface for detection.

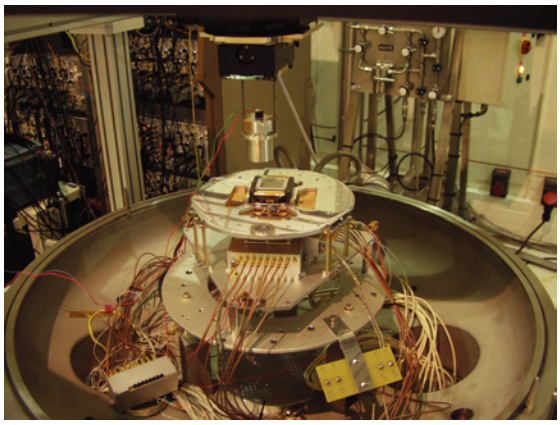

Figure 6: Experimental setup. The detector is mounted on a cooling plateau, and each strip is connected to one of the charge-sensitive amplifiers contained in the casings below. Only 16 strips per side were connected for the first tests. The whole setup is inside a vacuum chamber

3.1.2. Simulation means

MGS was used for simulating the theoretical current pulses for interactions at the same depth as the measured ones. The obtained signals were fed into a Pspice model of the charge-sensitive amplifier and the rest of the electronics used for the acquisition of pulses of the prototype, in order to obtain as realistically simulated signals as possible. A diagram of the model is shown at figure 7. It consists of the following stages:

- The charge-sensitive amplifier to convert the input current pulse into a voltage signal. A Pspice model of the A250F amplifier used in the actual set-up is not publicly available, so it was replaced by a generic amplifier in our circuit. The input FET model and the component values on the feedback loop were obtained from the Amptek website[20].

- A second amplifier follows the charge amplifier to increase the dynamic range of the signal. The signal is amplified by a factor of 2. This stage was implemented using an Analog Devices AD8011 chip in non-inverting configuration.

- An offset correction block to remove the continuum component introduced by the charge amplifier. The circuit was based on a resistive adder between the incoming signal and the output of a DAC. In the real set-up, the DAC input is calculated in the digital domain and back fed to the analogue board. In Pspice, the offset value is constant.

- After the sum, an additional amplification stage was implemented to control the dynamic range of the signal before reaching the ADC input. It was composed of three amplifiers in cascade, each allowing to switch its gain between x1 and x2. As a result, the total gain of the chain could vary among x1, x2, x4 and x8.

- Finally, a low pass filter was implemented to simulate the anti aliasing filter at the digitizer input. The technical documentation of the N6740 CAEN digitizer states that an anti-aliasing filter with cut-off frequency fc=30 MHz and linear phase response is set as the first stage of the board. Unfortunately, no information is given about the specific implementation of the filter, so a third order Bessel filter was used for the Pspice model, to ensure a flat group delay response along the pass band.

Both the MGS and the Pspice simulations ran on a Intel Xeon X5680 @ 3.33 GHz CPU with 16 GB RAM.

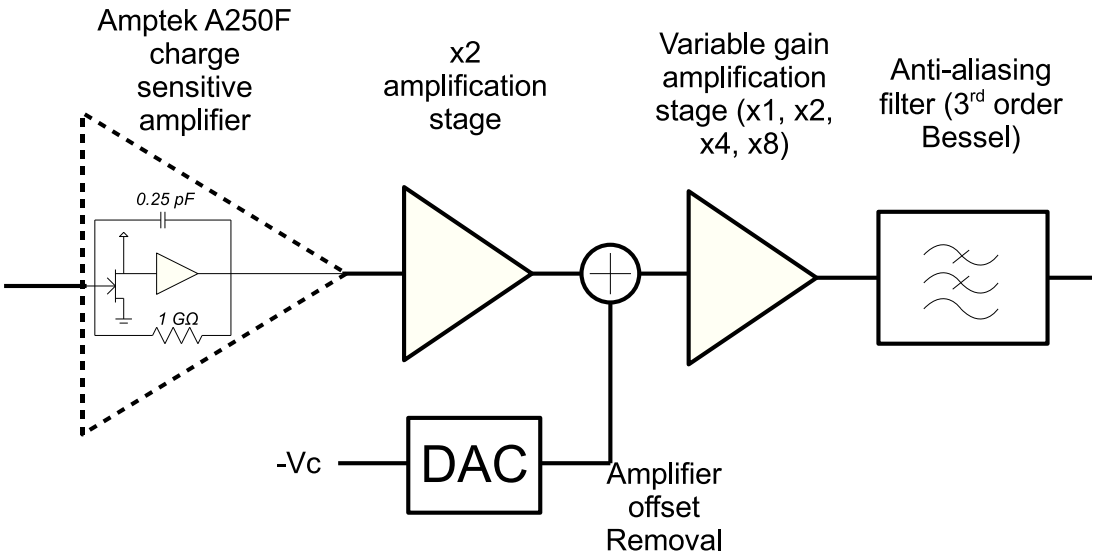

Figure 7: Block diagram of the Pspice model used for the readout of the pulse shapes generated with MGS.

3.1.3. Comparison method

As mentioned above, measured and simulated pulses were compared for each intersection between an anode and a cathode strip, and for 8 different depths of interaction. We denote z the depth of the interaction, and given that the laboratory prototype is irradiated from the cathode side, we define $z = 0$ as the cathode surface. The anode surface is then placed at $z = D$, D being the detector thickness, i.e. 11 *mm*. The comparison is therefore carried out for

$$z_k = \Delta_z/2 + k\Delta_z, \qquad k = 0, \ldots, 7 \tag{5}$$

with

$$\Delta_z = D/8 = 1.375mm \tag{6}$$

Obtaining the simulated pulse shapes at each z_k is straightforward using MGS, since the program allows to define the exact position(s) of the energy deposition(s). For simplicity, x and y dimensions were kept constant to simulate pulses in the center of the intersection, as lateral displacements within the pixel have no appreciable influence on the pulse shape [4]. The depth of the interaction of measured events, on the contrary, needs to be deduced from the analysis of the pulses. This analysis consists in comparing the *time of arrival* of the measured pulses at both electrodes, defining time of arrival as the instant when the pulse reaches 50% of its peak value.

Assuming that, as a basic approximation, an energy deposition consists of a pair of positive and negative point-like charges drifting from the deposition point towards the electrodes at constant (saturated) speed: the positive charge or hole drifting towards the cathode at speed v_h and the negative charge or electron drifting towards the anode at speed v_e. Assuming also that the pulses seen at each electrode rise instantaneously when the respective particles arrive at them, and that we are able to determine exactly those instants (t_h for the instant of arrival of the hole and t_e for the instant of arrival of the electron). Under these assumptions, and taking $t = 0$ as the instant of deposition, t_e takes its maximum value when $z = 0$, as the electron needs to travel all the detector thickness, D, before reaching to the anode. We then have:

$$t_{e,max} = \frac{D}{v_e} \tag{7}$$

Similarly, t_h is maximum when $z = D$:

[4] Energy depositions close to the strip boundary result in charge shared events which are rejected in the DAQ system.

$$t_{h,max} = \frac{D}{v_h} \tag{8}$$

And at any z between 0 and D:

$$t_e = \frac{D-z}{v_e}, \qquad t_h = \frac{z}{v_h} \tag{9}$$

By taking the difference of the last two expressions we obtain:

$$t_h - t_e = \frac{z}{v_h} - \frac{D-z}{v_e} \tag{10}$$

We call the term on the left the *difference in time of arrival* (dtoa) between the cathode and anode pulses. That is, $dtoa = t_e - t_h$. Note that from equations 7 and 8 we have $dtoa_{min} = -t_{e,max}$ and $dtoa_{max} = t_{h,max}$. Combining these with equation 10, we are able to express z as a function of $dtoa$:

$$z = \frac{dtoa - dtoa_{min}}{dtoa_{max} - dtoa_{min}} \times D \tag{11}$$

Therefore, with the approximations stated above, there is a linear relationship between z and $dtoa$, so we can define a Δ_{dtoa} equivalent to Δ_z (equation 6), as:

$$\Delta_{dtoa} = \frac{dtoa_{max} - dtoa_{min}}{8} \tag{12}$$

This way, the measured pulses at the depths z_k given by the equation 5, are those whose dtoa take the following values:

$$dtoa_k = \Delta_{dtoa}/2 + k\Delta_{dtoa}, \qquad k = 0, \ldots, 7 \tag{13}$$

Due to the fact that, in reality, the charge distributions that follow an interaction are not point-like, but form charge clouds of different shapes and sizes, the dtoa measurement can not be considered as the measurement of the exact depth of the interaction, but rather as the measurement of the depth of the charge distribution center. Taking this into account, each MGS pulse at depth z_k was not compared to a single measured pulse, but to an average of pulses whose calculated dtoa is in the range of values $[dtoa_k - \delta, dtoa_k + \delta]$. It was assumed that those pulses were due to interactions close enough to z_k so as their averaged response would be a fair approximation to the response of an interaction occurring at that point. The choice of δ supposes a trade-off: on one hand, the bigger the value, the more pulses will be averaged thus increasing statistics; on the other hand, as δ increases, the averaged signal becomes less representative of the response to a point-like deposit at z_k (as the range of depths that are included in the average also increases). $\delta = 3\ ns$ was finally retained, privileging the fact that responses to be averaged were not too spread in depth around z_k.

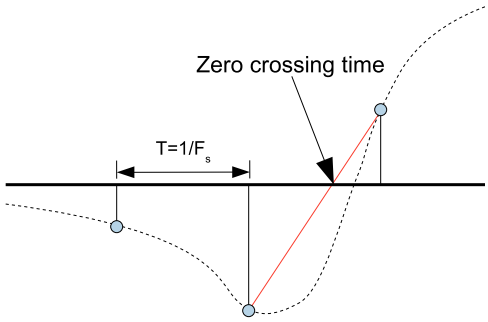

Figure 8: CFD output signal. Linear interpolation is used to estimate the zero crossing time with precision better than the sampling frequency.

3.1.4. The timing measurement

Real measured pulses have a finite rising time, so the *time of arrival* has to be defined. The criterion selected for this work is to define it as the instant when the pulse reaches 50% of its peak value. Note that this is an arbitrary measurement and does not mark the actual time of arrival of the charges to the electrodes. Indeed, the shape of the pulse is determined by the bandwidth of the electronics that do the acquisition.

The timing measurement is based on the *constant fraction discrimination* (CFD) method described in [16, pag. 628]. This technique consists in the addition of the incoming signal (scaled by the fraction value at which the measurement wants to be made, in our case 50%) with an inverted and delayed version of itself. The arrival time is then determined by the zero crossing time of the resulting signal. A linear interpolation has been used in this work to determine this instant with a precision better than our sampling frequency (see figure 8)

The timing measurement error was assessed through simulation. MGS was used for simulating an acquisition of events occurring all along the detector thickness and calculating the standard deviation of the *dtoa* measurement as a function of the interaction depth. The event energy was set to 100 keV, and a 1.5 keV FHWM equivalent white Gaussian noise was added to the signal. Noise addition was carried out at the output of the Pspice simulation, right before digitization. Under these

conditions, $\sigma_{dtoa} < 1\ ns$ was obtained for all z. The same simulation was repeated without linear interpolation of the CFD output, yielding $\sigma_{dtoa} < 8\ ns$. This shows the great benefit of interpolation to improve the precision of the timing measurement. We see also that the timing measurement for energy deposits of 100 keV is not affected by the 1.5 keV noise (typical value of our system).

3.1.5. Acquisition of the pulses

The acquisition of the measured pulses was carried out with the detector exposed to a ^{226}Ra source. The decay scheme of this isotope presents emission of gamma rays at 187.10, 242.00, 295.22, 351.93 and 609.31 keV. These emission lines are energetic enough to ensure that interactions will occur at any depth along the detector thickness. All events whose measured energy was below 100 keV were discarded to avoid degradation of the timing measurements due to a poor signal to noise ratio. Figure 9 shows the histogram of measured events as a function of dtoa, obtained under these conditions. The plot includes all energy deposits above 100 keV, as well as double events resulting from Compton interactions (assuming that enough energy is deposited at each interaction). For this reason, its shape does not correspond to the theoretical exponential attenuation curve expected for the combination of energies of the source. However, a decay on the number of counts can still be observed as we move from negative values of dtoa to positive values, which is consistent with the fact that the detector is irradiated from the cathode side.

This figure was used to determine the values of $dtoa_{min} = -110\ ns$ and $dtoa_{max} = 135\ ns$, thus allowing to compute Δ_{dtoa} and $dtoa_k$ from equations 12 and 13, respectively. Note that dtoa takes slightly higher positive values than negative ones, due to the fact that holes travel at a slower speed compared to electrons. Also, note that some counts can be found at values lower than $dtoa_{min}$ and higher than $dtoa_{max}$. These may correspond to events that occur within the gaps between strips. Those events could first drift to a region close to the gap surface and then drift laterally to the electrodes at slower speed (as the electric field between electrodes is weak), thus yielding higher dtoa values.

3.1.6. Validity of the linear approximation

Equation 11 was obtained supposing that the observed pulses rise instantaneously at the moment when charge carriers arrive to the electrodes. It was also supposed that the signal on an electrode was only due to the charge drifting towards it, while in reality some current is also induced by the motion of charges of opposite polarity.

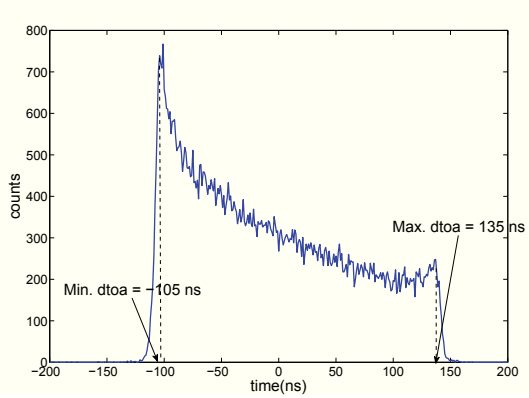

Figure 9: *dtoa* histogram. Detector is irradiated from the cathode side (negative values of *dtoa*). As expected, the number of counts decreases as the anode is approached (positive values).

A simulation was carried out using MGS to take into account the effect of finite pulse rise time and the signal induced by the charges of opposite polarity on the dtoa measurement. Figure 10 compares the calculated dtoa as a function of depth obtained for the MGS simulation with the values yield by equation 11, taking $dtoa_{min} = -105\ ns$ and $dtoa_{max} = 135\ ns$ (as observed in figure 9). We see that the simulation and the linear expression yield very similar results at the center of the detector, while they diverge near the electrodes. This can be explained because for interactions occurring near an electrode, the charge drifting in the opposite direction is sufficiently close at the beginning of its trajectory to induce significant current to the electrode, thus altering the pulse shape. This effect is not taken into account in the linear approximation. In addition, it can be observed that the difference between both curves is more pronounced for near-anode events, where the maximum dtoa value obtained in the simulation (122 ns) is 13 ns less than the measured one. We suspect it to be due to a slight overestimation of the hole drift velocity in the MGS transport model. In light of this figure, we should expect a discrepancy between the measured and simulated pulse shapes for near anode events. The 13 ns difference corresponds to a maximum depth error of 0.5 mm, which is below our target resolution of 1-2 mm along the depth (see figure 10). In conclusion, the linear approximation appears valid over a large domain of depth.

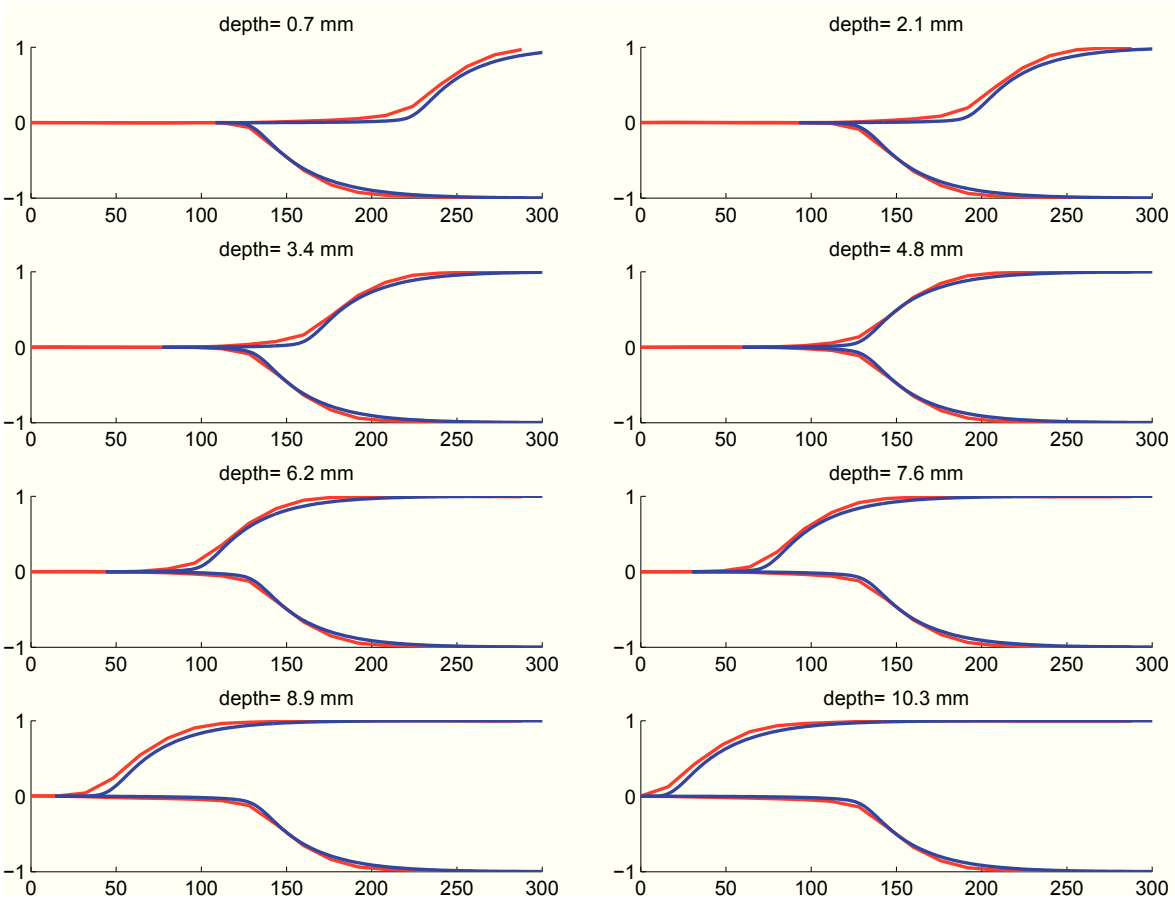

Figure 11: Comparison between simulated (blue) and measured (red) pulse shapes for different depths of interaction. Graphic units: normalized amplitude vs. time (ns)

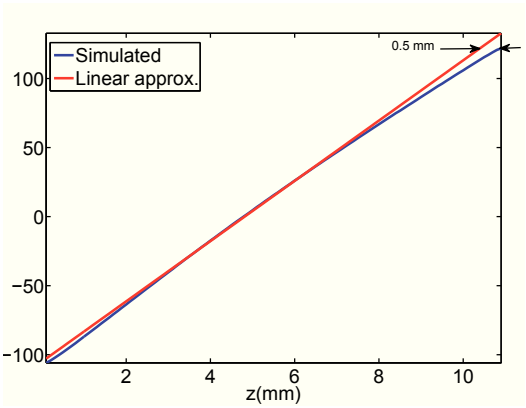

Figure 10: Comparison between the calculated dtoa as a function of the interaction depth obtained through simulation and the values yielded by equation 11

3.2. *Results of the comparison between measured and MGS pulse shapes.*

Figure 11 displays measured and simulated pulses for the z_k given by equation 5. The signals represent the rising edge of the pulses seen by the strips collecting the charge both at the cathode (negative pulse after inverting amplifier) and the anode (positive pulse). Each measured pulse is the average of 1000 events in the range $[dtoa_k - \delta, dtoa_k + \delta]$ (see section 3.1.3). z is the distance of the interaction from the cathode. The evolution of the pulse shape is as expected: for small depths, holes travel a short distance before being completely collected by the cathode, while the electrons need to cross all the detector volume before reaching the anode. This translates into negative pulses rising faster than positive ones. As the interaction penetrates deeper into the volume, the opposite effect is observed.

From figure 11 we see an excellent agreement between simulations and measurements for all depths of interaction. However, for the events near the electrodes small timing mismatches are observed of the order of 10 ns in the worst case. This reminds the results illustrated in figure 10, and discussed in section 3.1.6. They are likely due to the linear approximation used for calculating the depth as a function of dtoa, with probably a slight overestimation of the hole carrier velocity in the MGS code. It is also worth to note that the measured pulse shapes rise slightly faster than the simulated ones, which could indicate some inaccuracy in our Pspice model slowing down the simulated pulses. In Figure 12 we compare the amplitudes obtained by measurements and simulations. We see that, for all cases, the error is below 10% of the peak value.

Considering the close similarity between the pulse shapes generated with MGS and those obtained through the method of averaging measurements used in this work, we conclude that both methods are equally valid to generate a library containing the signal response to a basis of grid points, destined to be used by the position estimation algorithms foreseen in our detection system.

4. Discussion

MGS has been proved to be a valid software for the synthesis of pulse shapes in semiconductor detectors. A search for alternatives revealed that very few of such tools exist, and none of them was found to be freely downloadable and ready-to-use as MGS is [21]. Its main strengths, aside from the pulse shape simulation capability, reside in its easiness of use and the flexibility to simulate geometries of very different sizes and shapes. The fact that it is developed in a well-known language such as Matlab is another advantage, since users can easily add templates for new types of detectors, or even modify the code. However, despite of the qualities just described, some difficulties were encountered during our work which led to a reflection on the drawbacks and limitations of the simulation.

The usage of a regular grid throughout all the detector volume might make the simulation heavy in terms of computational cost and memory requirements. The choice of an adequate value for the separation between points, or grid step, depends on the detail required to correctly characterize the detector. MGS was originally designed to simulate detectors for nuclear physics applications such as AGATA. Due to its large size, a grid of relative low density suffices to accurately describe this kind of detectors. For instance, [6] reports a grid step of 1 mm. For smaller detectors, smaller step sizes must be used. It is the case, for example, of our DSSD prototype, where the gap between two consecutive strips is 50 μm. This means that a step size of 50 μm is the maximum value that should be considered for MGS to represent the discontinuity of the electrodes. However, using this value still yields a poor representation of the strips edges. The sharp transition from the metallic contact to germanium is modelled in the simulation as covering 50 μm. This affects the calculation of the response for interactions that occur in the gap between strips. Figures 13 and 14 represent the weighting potential near the gap for a small version of our prototype (only 4 strips per side), as calculated by MGS using two different grid steps: 50 μm and 10 μm, respectively. Let us recall that the weighting potential of a strip gets value 1 on its surface, and 0 on the rest of strip surfaces, so

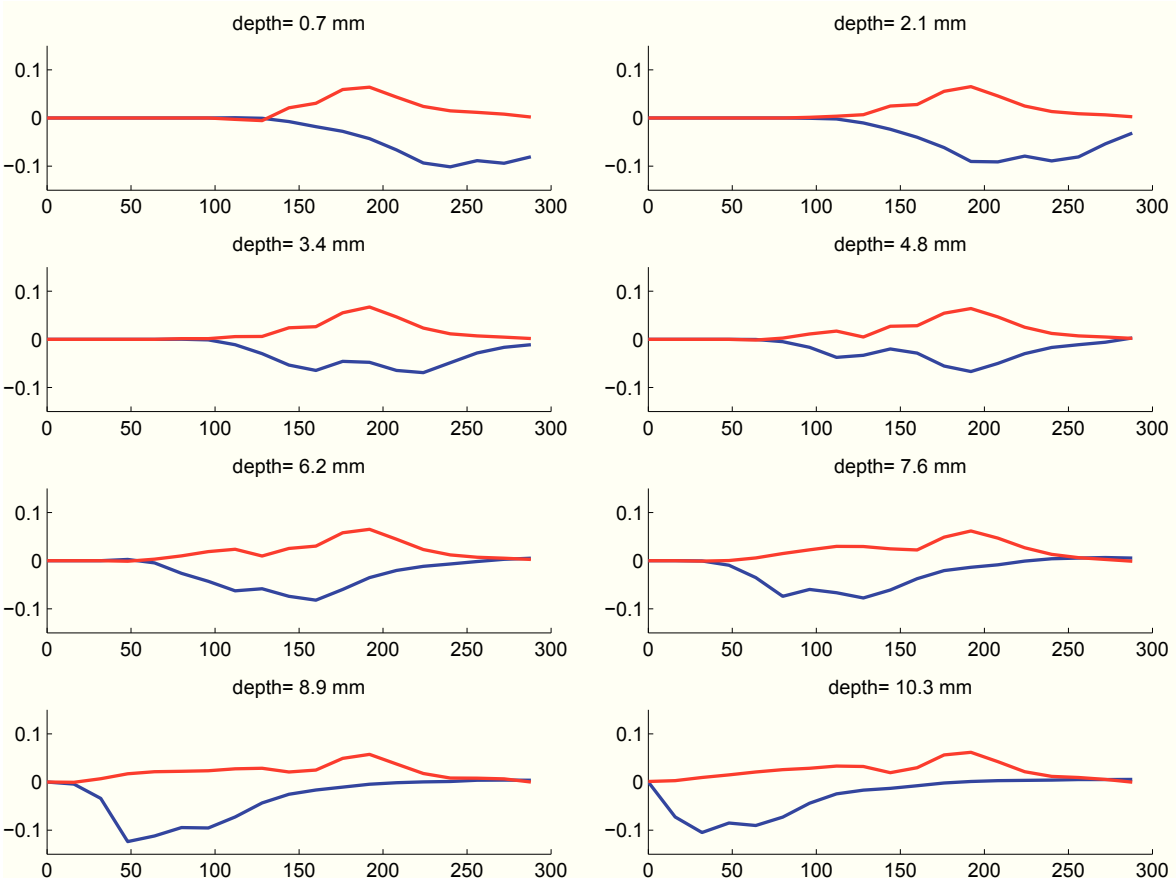

Figure 12: Difference of amplitude between measurements and simulations (simulated minus measured). Red curve corresponds to the cathode and blue curve to the anode. Graphic units: difference of normalized amplitudes vs. time (ns)

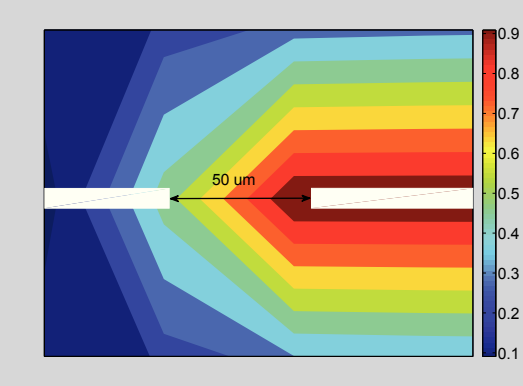

Figure 13: Weighting potential around a gap calculated using a 50 μm step size.

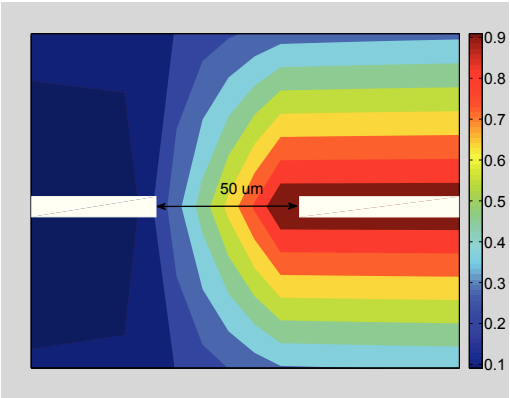

Figure 14: Weighting potential around a gap calculated using a 10 μm step size.

one would expect the transition between these two values to happen along the 50 μm gap. We see that this is well approximated with the 10μm step, while for the 50 μm step the neighbour strip surface is significantly overlapped by non null weighting potential values, as if the gap was in reality of 100 μm. This is explained by the fact that, with a 50 μm step, the last grid point of a strip and the first of the following are indeed separated by 2 steps of 50 μm. Seeing that, further reduction of the step size must be considered to properly simulate events within the gap

The 50 μm grid step, however, provides an accurate enough representation of the areas of interest in the framework of this work. Indeed, all the simulated events were located on the center of a pixel, thus aligned with the strip center both for the anode and for the cathode. In that region, a step smaller than 50 μm is of no interest. This is demonstrated in figures 13 and 14, where the weighting potentials, calculated with 50 μm and 10 μm step sizes, appear in perfect agreement below the strip surface.

4.1. Possible improvements of the MGS code

Taking into account the dimensions of our detector plus the surrounding space, the total volume to represent is a box of $5 \times 5 \times 1.5$ cm. With a step of 50 μm, this means a matrix of 300 million points. The amount of time (more than a day) needed by the implemented iterative algorithms to solve Poisson's equation has been found non-viable for matrices of this size. In order to mitigate the impact of the step reduction, we modified the MGS code to accept different step sizes in each dimension, passing from a cubic grid to a rectangular one. This way, the step size for the two dimensions of the detector plane remained at 50 μm (for the strip representation), while in the third dimension (orthogonal to the electrodes) a 0.5 mm step size was chosen. In this direction there is no change in the type of material, we have just to represent a linear gradient of impurities in the semiconductor, so a small step is not required. This modification reduced the number of grid points by a factor of 10, to 30 million. The time to solve Poisson's equation is significantly reduced but is still around 5 hours. The total simulation time, comprising the calculation of the weighting potential of the 8 central strips of each side was less than 100 hours.

Further improvements tom MGS could be made that would imply more profound modifications of the current code. In the case of DSSD's, the use of analytical expressions to calculate the weighting potential for the inner-most strips of the detector, instead of the numerical solution approach has already been discussed in section 2.4. As the weighting potential of each contact is calculated independently from the others, another way of reducing the simulation time would be the parallelization of these computations. The symmetries of certain detector geometries could also be exploited to reduce the volume in which the Poisson equation needs to be solved. For instance, a DSSD presents symmetries along the x, y and z coordinates. By setting the appropriate boundary conditions, the potential would only need to be solved in one of the eight octants of the coordinate system, thus reducing the total number of points of the matrix by a factor of eight. Finally, a way of greatly enhancing MGS performance would be the implementation of adaptative grids instead of the current rectangular grid of fixed step size. Therefore, a fine mesh could be used to represent in detail the small

parts of the detector, such as the electric contacts in segmented detectors, with no need to maintain it in other regions where such a detail is not required.

That said, most of the proposed modifications would probably require rewriting most of the code, which means a great investment in terms of time and workload. At the same time, what today is a very simple tool to use, would become more complex, as it probably would be up to the user to define more in-depth the functioning of the program (e.g. in the case of adaptative grids, the step size and scope of the different grids). The difficulty to add new templates and extend the program to new detector geometries would also be increased.

5. Conclusions

MGS, a simulation tool for the synthesis of the signal response for solid state detectors, has been presented. The program had been previously used for the simulation of AGATA detectors, and it has been validated here for an X-ray double sided strip detector. During our work, the software was slightly modified to better adapt to the simulation of a DSSD, passing from a cubic grid to a rectangular one, and thus reducing the computational cost of the simulation. A comparison was established between pulses generated with MGS and those measured on a laboratory prototype. The comparison focused on the timing properties between of and measurements for different interaction depths. The results showed that the simulation reproduced the measured signals very accurately, with a measured error of the order of 0.5 mm. In addition, the practical limitations of MGS for the simulation of a highly segmented DSS such as our prototype were discussed.

The precise knowledge of the pulse shapes is of special interest to test algorithms aiming at the estimation of the interaction position, such as the determination of the depth of the interaction through the difference in time of arrival of the pulses. In the detector design phase, a tool such MGS may provide a starting point for a complete simulation of the detection system, including the posterior pulse shaping and signal processing algorithms, allowing to estimate for example the attainable performances in terms of spatial resolution for a given geometry before manufacture. In light of the results presented in this paper and those reported for AGATA[6], we can conclude that MGS is a valuable tool for the simulation of solid state detectors of varied geometries, ranging from big detectors for gamma-ray tracking arrays, to small detectors for X-ray applications.

6. Acknowledgements

This work has been supported by a Centre National d'Études Spatiales and Centre National de la Recherche Scientifique grant.

[1] J. Lee, H. S. Jung, H. Y. Cho, Y. Kwon, C. Lee, A novel digital pulse-shape analysis for high-resolution position-sensitive gamma-ray spectroscopy, in: Advancements in Nuclear Instrumentation Measurement Methods and their Applications (ANIMMA), 2009 First International Conference on, pp. 1–5.

[2] B. Aspacher, G. J. Bamford, R. Coldwell, A. C. Rester, Compton continuum suppression by pulse shape analysis, in: Nuclear Science Symposium and Medical Imaging Conference, 1992., Conference Record of the 1992 IEEE, pp. 44–46 vol.1.

[3] J. Roth, J. H. Primbsch, R. Lin, Segmentation and pulse shape discrimination techniques for rejecting background in germanium detectors, Nuclear Science, IEEE Transactions on 31 (1984) 367–371.

[4] P. Medina, C. Santos, D. Villaume, A simple method for the characterization of hpge detectors, in: Instrumentation and Measurement Technology Conference, 2004. IMTC 04. Proceedings of the 21st IEEE, volume 3, pp. 1828–1832 Vol.3.

[5] MATLAB, version 7.10.0 (R2010a), The MathWorks Inc., Natick, Massachusetts, 2010.

[6] M. Dimmock, A. Boston, J. Cresswell, I. Lazarus, P. Medina, P. Nolan, C. Parisel, C. Santos, J. Simpson, C. Unsworth, Validation of pulse shape simulations for an agata prototype detector, Nuclear Science, IEEE Transactions on 56 (2009) 2415–2425.

[7] B. P. F. Dirks, P. Ferrando, U. Briel, O. Gevin, E. Kendziorra, P. Laurent, O. Limousin, F. Lugiez, J. Martignac, M. Authier, C. Chapron, P. Lechner, G. Pareschi, Y. Rio, J. Roques, P. Salin, L. Strüder, The focal plane of the simbol-x space mission, 2006.

[8] Synopsis, Ise-tcad tools, 2013. [http://www.synopsys.com/Tools/TCAD/Pages/default.aspx, Online; accessed 9-August-2013].

[9] Z. He, Review of the shockley-ramo theorem and its application in semiconductor gamma-ray detectors, Nuclear Instruments and Methods in Physics Research Section A: Accelerators, Spectrometers, Detectors and Associated Equipment 463 (2001) 250 – 267.

[10] I. Bronstein, K. Semendyayev, Handbook of Mathematics, Springer-Verlag London, UK, 3rd edition, 1997.

[11] D. M. Young, Jr, Iterative Methods for Solving Partial Difference Equations of Elliptic Type, Ph.D. thesis, Harvard University, Cambridge, Massachusetts, 1950.

[12] L. Mihailescu, W. Gast, R. Lieder, H. Brands, H. Jager, The influence of anisotropic electron drift velocity on the signal shapes of closed-end hpge detectors, Nuclear Instruments and Methods in Physics Research Section A: Accelerators, Spectrometers, Detectors and Associated Equipment 447 (2000) 350 – 360.

[13] B. Bruyneel, Characterization of Segmented Large Volume, High Purity Germanium Detectors, Ph.D. thesis, Mathematisch-Naturwissenschaftliche Fakultat, Köln, 2006.

[14] G. Ottaviani, C. Canali, A. A. Quaranta, Charge carrier transport properties of semiconductor materials suitable for nuclear radiation detectors, Nuclear Science, IEEE Transactions on 22 (1975) 192–204.

[15] Q. R., M. C., P. V., S. S., A temperature dependent model for the saturation velocity in semiconductor materials, Materials Science in Semiconductor Processing 3 (2000) 149–155.

[16] G. Knoll, Radiation and Detection Measurement, John Wiley & Sons, second edition, 1979.

[17] Z. He, Potential distribution within semiconductor detectors using coplanar electrodes, Nuclear Instruments and Methods in Physics Research Section A: Accelerators, Spectrometers, Detectors and Associated Equipment 365 (1995) 572 – 575.

[18] D. Bazzacco, T. Kroll, A genetic algorithm for the decomposition of multiple hit events in the gamma-ray tracking detector mars, Nucl.Instr.Meth. A 565 (2006) 691.

[19] A. Khaplanov, Position-sensitive germanium detectors for gamma-ray tracking, imaging and polarimetry, Ph.D. thesis, KTH, Physics, Stockholm, 2010.

[20] Amptek, A250f reference, 2013. [http://www.amptek.com/a250fn.html, Online; accessed 9-August-2013].

[21] IPHC, Mgs code, 2013. [http://www.iphc.cnrs.fr/-MGS-.html, Online; accessed 9-August-2013].

Bibliography

[1] NASA, Nustar website, 2013. [http://www.nustar.caltech.edu/, Online; accessed 10-October-2013].

[2] JAXA, Astro-h website, 2013. [http://astro-h.isas.jaxa.jp/index.html.en, Online; accessed 10-October-2013].

[3] D. Della Monica Ferreira, F. E. Christensen, M. J. Pivovaroff, N. Brejnholt, M. Fernandez-Perea, N. J. S. Westergaard, A. C. Jakobsen, M.-A. Descalle, R. Soufli, J. K. Vogel, Hard x-ray/soft gamma ray telescope designs for future astrophysics missions, 2013.

[4] R. Clédassou, P. Ferrando, Simbol-x: An hard x-ray formation flying mission, in: P. Ballmoos (Ed.), Focusing Telescopes in Nuclear Astrophysics, Springer Netherlands, 2006, pp. 421–434.

[5] J.-P. Roques, E. Jourdain, L. Bassani, A. Bazzano, R. Belmont, A. Bird, E. Caroli, M. Chauvin, D. Clark, N. Gehrels, U. Goerlach, F. Harrisson, P. Laurent, J. Malzac, P. Medina, A. Merloni, S. Paltani, J. Stephen, P. Ubertini, J. Wilms, Phenix: a new vision for the hard x-ray sky, Experimental Astronomy 34 (2012) 489–517.

[6] O. Glasser, Wilhelm Conrad Röntgen and the Early History of the Roentgen Rays, Norman radiology series, Norman Pub., 1934.

[7] E. O. Hulburt, Ionization in the upper atmosphere of the earth, Phys. Rev. 31 (1928) 1018–1037.

[8] H. Friedman, Ultraviolet and x rays from the sun, Annual Review of Astronomy and Astrophysics 1 (1963) 59–96.

[9] R. Giacconi, H. Gursky, F. R. Paolini, B. B. Rossi, Evidence for x rays from sources outside the solar system, Phys. Rev. Lett. 9 (1962) 439–443.

[10] S. Bowyer, E. Byram, T. Chubb, H. Friedman, X-ray sources in the galaxy, Nature 201 (1964) 1307–1308.

[11] P. Landsberg, Thermodynamics and Statistical Mechanics, Dover Books on Physics Series, Dover Publications, 1978.

[12] G. Knoll, Radiation and Detection Measurement, John Wiley & Sons, second edition, 1979.

[13] V. A. Bordovitsyn, I. Ternov, Synchrotron Radiation Theory and Its Development: In Memory of I.M. Ternov, World Scientific series on synchrotron radiation techniques and applications, World Scientific, 1999.

[14] G. B. Rybicki, A. P. Lightman, Radiative Processes in Astrophysics, John Wiley & Sons, Inc, 1979.

[15] R. Giacconi, P. Rosati, Cosmic x-ray sources, 2008. [http://www.scholarpedia.org/article/Cosmic_ X-ray_ sources, Online; accessed 13 October 2013].

[16] NASA, The sun's corona, 2014. [http://imagine.gsfc.nasa.gov/docs/science/mysteries_ l1/corona.html, Online; accessed 11-March-2014].

[17] L. der Klis, Compact Stellar X-ray Sources, Cambridge University Press, 2010.

[18] NASA, Supernovae, 2014. [http://imagine.gsfc.nasa.gov/docs/science/know_ l1/supernovae.html, Online; accessed 11-March-2014].

[19] G. P., X-ray studies of active galactic nuclei, Asian Jour Phys (2005) 90.

[20] ESA, Xmm-newton website, 2013. [http://sci.esa.int/xmm-newton/, Online; accessed 14-October-2013].

[21] ESA, Integral website, 2013. [http://sci.esa.int/integral/, Online; accessed 14-October-2013].

[22] NASA, Chandra website, 2013. [http://chandra.harvard.edu/, Online; accessed 14-October-2013].

[23] JAXA, Suzaku website, 2013. [http://www.astro.isas.jaxa.jp/suzaku/index.html.en, Online; accessed 14-October-2013].

[24] NASA, Swift website, 2014. [http://www.nasa.gov/mission_ pages/swift/main/.UylkvIV8qw4, Online; accessed 19-March-2014].

[25] JAXA, Maxi website, 2014. [http://kibo.jaxa.jp/en/experiment/ef/maxi/, Online; accessed 19-March-2014].

[26] A. Goldwurm, Imaging techniques applied to the coded mask sigma telescope, in: L. Bassani, G. Cocco (Eds.), Imaging in High Energy Astronomy, Springer Netherlands, 1995, pp. 9–18.

[27] S. Barthelmy, L. Barbier, J. Cummings, E. Fenimore, N. Gehrels, D. Hullinger, H. Krimm, C. Markwardt, D. Palmer, A. Parsons, G. Sato, M. Suzuki, T. Takahashi, M. Tashiro, J. Tueller, The burst alert telescope (bat) on the swift midex mission, Space Science Reviews 120 (2005) 143–164.

[28] A. Goldwurm, P. Goldoni, A. Gros, J. Stephen, L. Foschini, F. Gianotti, L. Natalucci, G. De Cesare, M. Del Santo, Gamma-ray imaging with the coded mask ibis telescope, in: 4th INTEGRAL workshop, Alicante.

[29] H. Wolter, Mirror systems with glancing incidence as image producing optics for x-rays, Ann. Phys. 10 (1952) 94.

[30] P. Sangsingkeow, K. D. Berry, E. J. Dumas, T. W. Raudorf, T. A. Underwood, Advances in germanium detector technology, Nuclear Instruments and Methods in Physics Research Section A: Accelerators, Spectrometers, Detectors and Associated Equipment 505 (2003) 183 – 186. Proceedings of the tenth Symposium on Radiation Measurements and Applications.

[31] T. e. Takashi, Hard x-ray detector (hxd) on board suzaku, Publ. Astron. Soc. Jap. 59 (2007) 35–51.

[32] M. Weisskopf, The chandra x-ray observatory: An overview, Advances in Space Research 32 (2003) 2005 – 2011.

[33] L. Struder, J. Englhauser, R. Hartmann, P. Holl, N. Meidinger, H. Soltau, U. Briel, K. Dennerl, M. Freyberg, F. Haberl, G. Hartner, E. Pfeffermann, T. Stadlbauer, E. Kendziorra, pnccds on xmm-newton-42 months in orbit, Nuclear Instruments and Methods in Physics Research Section A: Accelerators, Spectrometers, Detectors and Associated Equipment 512 (2003) 386 – 400.

[34] MPE, erosita website, 2014. [http://www.mpe.mpg.de/eROSITA, Online; accessed 19-March-2014].

[35] ACG, Athena website, 2014. [http://www.the-athena-x-ray-observatory.eu/, Online; accessed 19-March-2014].

[36] NASA, The black hole evolution and space time (best) observatory, 2011. [http://pcos.gsfc.nasa.gov/studies/rfi/Krawczynski-Henric-RFI.pdf, Online; accessed 19-March-2014].

[37] NASA, The high energy x-ray probe(hex-p), 2011. [http://pcos.gsfc.nasa.gov/studies/rfi/Harrison-Fiona-RFI.pdf, Online; accessed 19-March-2014].

[38] INAF, New hard x-ray mission (nhxm), 2010. [http://www.brera.inaf.it/NHXM/index.php5/About_NHXM, Online; accessed 19-March-2014].

[39] V. Lonjou, J. Roques, P. V. Ballmoos, P. Jean, J. Knodlseder, G. Skinner, A. Thevenin, G. Weidenspointner, Characterization of the in-flight degradation of the integral/spi detectors, Nuclear Instruments and Methods in Physics Research Section A: Accelerators, Spectrometers, Detectors and Associated Equipment 554 (2005) 320 – 330.

[40] P. Sellin, A. W. Davies, A. Lohstroh, M. Ozsan, J. Parkin, Drift mobility and mobility-lifetime products in cdte:cl grown by the travelling heater method, Nuclear Science, IEEE Transactions on 52 (2005) 3074–3078.

[41] K. Suzuki, S. Seto, T. Sawada, K. Imai, Carrier transport properties of hpb cdznte and thm cdte:cl, Nuclear Science, IEEE Transactions on 49 (2002) 1287–1291.

[42] Development of double-sided silicon strip detectors (dssd) for a compton telescope, Nuclear Instruments and Methods in Physics Research Section A: Accelerators, Spectrometers, Detectors and Associated Equipment 579 (2007) 859 – 865. Proceedings of the 6th.

[43] P. Bloser, F. Schopper, R. Andritschke, G. Kanbach, A. Zoglauer, P. Lechner, Development of silicon strip detectors for a medium energy gamma-ray telescope, Nuclear Instruments and Methods in Physics Research Section A: Accelerators, Spectrometers, Detectors and Associated Equipment 512 (2003) 220 – 228. Proceedings of the 9th European Symposium on Semiconductor Detectors: New Developments on Radiation Detectors.

[44] S. E. Boggs, The Advanced Compton Telescope mission, NASA Vision Mission Concept Study Report 50 (2006) 604–607.

[45] R. Cooper, A. Boston, H. Boston, J. Cresswell, A. Grint, A. Mather, P. Nolan, D. Scraggs, G. Turk, C. Hall, I. Lazarus, A. Berry, T. Beveridge, J. Gillam, R. Lewis, Smartpet: Applying {HPGe} and pulse shape analysis to small-animal {PET}, Nuclear Instruments and Methods in Physics Research Section A: Accelerators, Spectrometers, Detectors and Associated Equipment 579 (2007) 313 – 317. <ce:title>Proceedings of the 11th Symposium on Radiation Measurements and Applications</ce:title>.

[46] L. C. Johnson, D. L. Campbell, E. L. Hull, T. E. Peterson, Characterization of a high-purity germanium detector for small-animal spect, Physics in Medicine and Biology 56 (2011) 5877.

[47] N. Scholz, H. Dennert, W. Eyrich, A. Lehmann, M. Moosburger, H. Wirth, Investigation of large area semiconductor strip detectors for use in low energy nuclear physics, Nuclear Instruments and

Methods in Physics Research Section A: Accelerators, Spectrometers, Detectors and Associated Equipment 313 (1992) 233 – 236.

[48] B. Phlips, W. Johnson, R. Kroeger, J. Kurfess, G. Phillips, E. Wulf, P. Luke, Development of germanium strip detectors for environmental remediation, Nuclear Science, IEEE Transactions on 49 (2002) 597–600.

[49] O. Limousin, F. Lugiez, O. Gevin, A. Meuris, C. Blondel, E. Delagnes, M. Donati, I. L. Mer, J. Martignac, F. Pinsard, M. Vassal, R. Bocage, F. Soufflet, Caliste 256: A cdte imaging spectrometer for space science with a 580 μm pixel pitch., Nuclear Instruments and Methods in Physics Research Section A: Accelerators, Spectrometers, Detectors and Associated Equipment 647 (2011) 46 – 54.

[50] NIST, Electron stopping ranges, 2013. [http://physics.nist.gov/PhysRefData/Star/Text/ESTAR.html, Online; accessed 20-September-2013].

[51] W. Heitler, The Quantum Theory of Radiation, Dover Books on Physics and Chemistry, Dover Publications, 1954.

[52] S. Sze, Physics of semiconductor devices, Wiley, 2nd edition, 1981.

[53] L. Reggiani, C. Canali, F. Nava, A. A. Quaranta, Diffusion coefficient of holes in ge, Journal of Applied Physics 49 (1978) 4446–4452.

[54] Z. He, Review of the shockley-ramo theorem and its application in semiconductor gamma-ray detectors, Nuclear Instruments and Methods in Physics Research Section A: Accelerators, Spectrometers, Detectors and Associated Equipment 463 (2001) 250 – 267.

[55] K. Vetter, M. Burks, L. Mihailescu, Gamma-ray imaging with position-sensitive {HPGe} detectors, Nuclear Instruments and Methods in Physics Research Section A: Accelerators, Spectrometers, Detectors and Associated Equipment 525 (2004) 322 – 327. <ce:title>Proceedings of the International Conference on Imaging Techniques in Subatomic Physics, Astrophysics, Medicine, Biology and Industry</ce:title>.

[56] Amptek, A250f reference, 2013. [http://www.amptek.com/a250fn.html, Online; accessed 9-August-2013].

[57] Mod. N6740 32 channel 12 bit 65 MS/S digitizer manual rev.9, CAEN, 2013.

[58] P. Medina, C. Santos, D. Villaume, A simple method for the characterization of hpge detectors, in: Instrumentation and Measurement Technology Conference, 2004. IMTC 04. Proceedings of the 21st IEEE, volume 3, pp. 1828–1832 Vol.3.

[59] M. Dimmock, A. Boston, J. Cresswell, I. Lazarus, P. Medina, P. Nolan, C. Parisel, C. Santos, J. Simpson, C. Unsworth, Validation of pulse shape simulations for an agata prototype detector, Nuclear Science, IEEE Transactions on 56 (2009) 2415–2425.

[60] G. Campos, Modelling of the analog electronic stage of a detection system for hard x-ray astronomy, 2012. (Master Thesis).

[61] I. Mateu, P. Medina, J.-P. Roques, E. Jourdain, Simulation of the charge collection and signal response of a hpge double sided strip detector using mgs, Nuclear Instruments and Methods A (2013). To be published.

[62] I. Bronstein, K. Semendyayev, Handbook of Mathematics, Springer-Verlag London, UK, 3rd edition, 1997.

[63] D. M. Young, Jr, Iterative Methods for Solving Partial Difference Equations of Elliptic Type, Ph.D. thesis, Harvard University, Cambridge, Massachusetts, 1950.

[64] L. Mihailescu, W. Gast, R. Lieder, H. Brands, H. Jager, The influence of anisotropic electron drift velocity on the signal shapes of closed-end hpge detectors, Nuclear Instruments and Methods in Physics Research Section A: Accelerators, Spectrometers, Detectors and Associated Equipment 447 (2000) 350 – 360.

[65] B. Bruyneel, Characterization of Segmented Large Volume, High Purity Germanium Detectors, Ph.D. thesis, Mathematisch-Naturwissenschaftliche Fakultat, Köln, 2006.

[66] G. Ottaviani, C. Canali, A. A. Quaranta, Charge carrier transport properties of semiconductor materials suitable for nuclear radiation detectors, Nuclear Science, IEEE Transactions on 22 (1975) 192–204.

[67] Q. R., M. C., P. V., S. S., A temperature dependent model for the saturation velocity in semiconductor materials, Materials Science in Semiconductor Processing 3 (2000) 149–155.

[68] Z. He, Potential distribution within semiconductor detectors using coplanar electrodes, Nuclear Instruments and Methods in Physics Research Section A: Accelerators, Spectrometers, Detectors and Associated Equipment 365 (1995) 572 – 575.

[69] V. Radeka, Trapezoidal filtering of signals from large germanium detectors at high rates, Nuclear Instruments and Methods 99 (1972) 525 – 539.

[70] V. T. Jordanov, G. F. Knoll, A. C. Huber, J. A. Pantazis, Digital techniques for real-time pulse shaping in radiation measurements, Nuclear Instruments and Methods in Physics Research Section A: Accelerators, Spectrometers, Detectors and Associated Equipment 353 (1994) 261 – 264.

[71] J. Hayward, D. Wehe, Incomplete charge collection in an {HPGe} double-sided strip detector, Nuclear Instruments and Methods in Physics Research Section A: Accelerators, Spectrometers, Detectors and Associated Equipment 586 (2008) 215 – 223.

[72] M. Amman, P. Luke, Three-dimensional position sensing and field shaping in orthogonal-strip germanium gamma-ray detectors, Nuclear Instruments and Methods in Physics Research Section A: Accelerators, Spectrometers, Detectors and Associated Equipment 452 (2000) 155 – 166.

[73] A. Khaplanov, Position-sensitive germanium detectors for gamma-ray tracking, imaging and polarimetry, Ph.D. thesis, KTH, Physics, Stockholm, 2010.

[74] C. Lawson, R. Hanson, Solving Least Squares Problems, Prentice-Hall, 1974.

Digital signal processing for hard X-ray detection systems for spatial applications.

Abstract: Anticipating future mission opportunities in high-energy astronomy, the development of a hard X-ray detection system for imaging and spectrometry is in progress at the *Institut de Recherche en Astrophysique et Planétologie* of Toulouse. The system is based on a High-purity Germanium double sided strip detector and aims at an energy coverage from a few keV up to a few hundred keV. Besides the sophisticated detector design, the extensive use of digital signal processing algorithms for the analysis of the impulsion is another innovation in this project, and constitutes the main topic of this thesis.

Astrophysics in the hard X-ray domain expect an era of major evolution in the upcoming years. Technological progress in mirror manufacturing allows now the focusing of photons well above 10 keV, which for many years had been the upper limit allowed by the technology. NASA's Nustar observatory, launched in 2012, and JAXA's Astro-H, to be launched in 2015, are the first missions to exploit the new mirrors for energies up to 80 keV. However, last research shows that focusing optics beyond this limit are to be expected soon. With this new generation of optics, a need for new detectors capable of exploiting the focusing capabilities is currently developing .

One of the main features of the studied detector is the possibility to obtain a three dimensional location of the interaction of the photons in its volume, with immediate applications in background reduction and tracking of Compton events for polarimetry measurements. For this purpose, we implemented an estimator of the interaction position, which is presented in this work, together with the methods used for calibration, triggering, pulse shaping and energy measurement purposes.

In order to develop a full simulation of the system, we have adapted to our particular case the MGS tool, an already existing Matlab code for the simulation of the charge collection processes and signal response provided by the detector, and we have used Pspice to model the analogue readout stage prior to the digitizer. Both tools have allowed us to generate realistic input signals for the testing of the performances of the signal processing algorithms in charge of the energy measurements and the location of the interaction position.

Finally, we have completed the study with the first measurements obtained from Phenomena, a laboratory prototype of the detection system which has been designed and manufactured in the framework of a Research and Technology action at IRAP, funded by the CNES.

AUTEUR: Isidre MATEU SUAU

TITRE: Systèmes de détection digitaux par traitement numérique des impulsions X-dur pour des applications spatiales

DIRECTEUR DE THESE: Jean-Pierre ROQUES

LIEU ET DATE DE SOUTENANCE: IRAP, le 5 février 2014

RESUME:

Pour préparer les futures missions d'astronomie haute énergie, nous avons développé, à l'Institut de Recherche en Astrophysique et Planétologie de Toulouse, un système de détection pour l'imagerie et la spectroscopie des rayons X-durs. Celui-ci est basé sur un détecteur en Germanium haute pureté en configuration planaire, avec des électrodes segmentées par pistes, et vise une couverture en énergie allant de quelques keV à quelques centaines de keV. En plus d'une réflexion très poussée au niveau de la conception du détecteur, ce projet se montre également innovant par l'utilisation extensive d'algorithmes de traitement numérique pour l'analyse des impulsions. C'est ce point qui constitue le sujet principal de cette thèse.

L'astrophysique dans le domaine des rayons X-dur voit s'ouvrir une ère de grande évolution pour les années à venir. Des progrès technologiques dans la fabrication de miroirs permettent maintenant de focaliser les photons au delà de 10 keV, ce qui était une limite technique depuis de nombreuses années. L'observatoire NuSTAR de la NASA, lancé en 2012, et Astro-H (JAXA), qui sera lancé en 2015, sont les premières missions à exploiter ces nouveaux miroirs pour des énergies allant jusqu'à 80 keV. Cependant, des recherches récentes montrent que des optiques capables de focaliser au delà de cette limite sont sur le point d'être réalisées. Avec cette nouvelle génération d'optiques, apparaît le besoin de nouveaux détecteurs capables de les exploiter pleinement.

Une des principales caractéristiques du détecteur proposé à l'IRAP est la possibilité d'obtenir une localisation du point d'interaction des photons en volume, avec application immédiate pour la réduction de bruit de fond et le suivi des événements Compton permettant des mesures polarisation. À ce propos, nous avons implémenté un algorithme pour déterminer la position des interactions, ainsi que des méthodes pour réaliser la calibration du détecteur, gérer les déclenchements, réaliser la mise en forme et mesurer l'énergie.

Afin d'obtenir une simulation complète du système, nous avons adapté MGS, un code Matlab déjà existant, pour la simulation de la collection de charge et de la réponse de notre détecteur, et nous avons utilisé Pspice pour modéliser l'électronique de lecture. Ces deux outils nous ont permis de générer des signaux réalistes pour tester les performances des algorithmes de traitement du signal pour la mesure d'énergie et la localisation de l'interaction.

Finalement, nous présentons les premières mesures réalisées avec PheniX, prototype d'un système de détection conçu et réalisé dans le cadre d'une action de Recherche et Développement à l'IRAP, avec un financement CNES.

MOTS-CLES: PHENIX, Traitement du signal, Détection, Spectroscopie, Imagerie, Rayons X, Germanium, Détecteur planaire à pistes

---

DISCIPLINE: Astrophysique, Sciences de l'Espace, Planétologie

---

Institut de Recherche en Astrophyisique et Planétologie - 9, Avenue du Colonel Roche - BP 4346 - 31028 Toulouse Cedex 4